eXPRESS Polymer Letters Vol.8, No.2 (2014) 73
Available online at www.expresspolymlett.com
DOI: 10.3144/expresspolymlett.2014.9

Editorial corner – a personal view

The ongoing impact of carbon (allotropic forms)/polymer composites

G. C. Psarras*

Department of Materials Science, University of Patras, Patras 26504, Hellas (Greece)

Carbon reinforced polymer composites are in the front line of technological applications and research interest for decades. Tire industry, aerospace and automotive industry, production of sport and leisure goods, microelectronic and electrochemical manufacturing are some of the main fields of carbon/polymer composites applications.

Carbon lies in the IV column of the periodic table, being the lightest element of the column. It differs substantially from the rest column's elements due to its ability to form sp^2 bonding. Carbon is found in two allotropic forms in nature, diamond and graphite. Carbyne and fullerenes are two additional allotropic forms of carbon, chemically synthesized.

The significant impetus in the carbon reinforced polymer composites (CRPs) was given by the industrial production of carbon fibres. Although, the earliest reference for commercial use of carbon fibers goes back to the late 1800s, practical end use products utilizing carbon fibres first appeared in the 1960s. Car racing and aerospace industries were the pioneers to exploit the high modulus, high strength, and low weight properties of CRPs. On the other hand, the electrical properties of particulate CRPs, such as carbon black composites, were also intensively investigated.

The advent of nanotechnology era and the development of various types of polymer matrix nanocomposites gave the opportunity for a new breakthrough in the field of CRPs. Carbon nanoinclusions, such as single- and multi-wall carbon nanotubes, carbon nanofibres, exfoliated graphite nanoplatelets, and recently graphene, embedded in a polymer matrix result in composite systems with improved mechanical and tribological characteristics, enhanced heat resistance, and advanced optical and electrical behaviours.

Mutual interactions between carbon nanoinclusions and interactions between polymer macromolecules and carbon nanoparticles, as well as, missing of methods to achieve homogeneous or preferential distribution of nanofillers, are current drawbacks of nano-CRP technology, in tandem with their economic cost. These aspects are in the focus of worldwide research efforts, in the field, since controlling the distribution state and tuning the polymer-nanofiller interactions will allow full tailoring of the overall performance of composite structures.

The diversity of possible polymer matrices and carbon nanoinclusions – currently available and forthcoming ones – for the production of nano-CRPs, indicate that perspectives for future development are wide open.

Prof. Dr. Georgios C. Psarras
Member of International Advisory Board

---

*Corresponding author, e-mail: G.C.Psarras@upatras.gr

eXPRESS Polymer Letters Vol.8, No.2 (2014) 74–84
Available online at www.expresspolymlett.com
DOI: 10.3144/expresspolymlett.2014.10

Graphene reinforced ultra high molecular weight polyethylene with improved tensile strength and creep resistance properties

A. Bhattacharyya[1*], *S. Chen*[2], *M. Zhu*[2]

[1]Nanotech Research Facility, PSG Institute of Advanced Studies, 641004 Coimbatore, India
[2]College of Materials Science and Engineering, Donghua University, 201620 Shanghai, China

Received 9 August 2013; accepted in revised form 24 September 2013

Abstract. Reduced graphene oxide or graphene was dispersed in ultra high molecular weight polyethylene (UHMWPE) using two methods to prepare nanocomposite films. In pre-reduction method, graphite oxide (GO) was exfoliated and dispersed in organic solvents and reduced to graphene before polymer was added, while reduction of graphene oxide was carried out after polymer addition for *in situ* reduction method. Raman spectroscopic study reveals that the second method results in better exfoliation of graphene but it has more amorphous content as evident from selected area electron diffraction (SAED) pattern, wide angle X-ray and differential scanning calorimetry (DSC). The nanocomposite film produced by pre-reduction method possesses higher crystallinity (almost the same as that of the pure film) as compared to the *in situ* method. It shows better modulus (increased from 864 to 1236 MPa), better strength (increased from 12.6 to 22.2 MPa), network hardening and creep resistance (creep strain reduced to 9% from 50% when 40% of maximum load was applied for 72 h) than the pure film. These findings show that graphene can be used for reinforcement of UHMWPE to improve its tensile and creep resistance properties.

Keywords: *nanocomposites, mechanical properties, graphene, ultra high molecular weight polyethylene (UHMWPE)*

1. Introduction

Ultra high molecular weight polyethylene (UHMWPE) has been extensively used for various high performance application areas as biomedical, defence, etc [1, 2]. However, its adverse properties such as creep, abrasion resistance, etc. are still a matter of concern [3]. Several research groups have observed that the mechanical properties of a polymer can be improved using small amount of nanofillers in it [4]. Among the nanofillers, carbon nanotube (CNT) is researched most as a reinforcement due to its excellent tensile properties [5]. However, after years of research, the expected improvements have not yet been achieved due to several reasons. Except the difficulty of dispersing CNT in viscous solution, the caged structure of CNT is the main drawback for load transmission from polymer matrix to the reinforcement as it slips from the polymer matrix [6]. Functionalization of CNT partially solves this problem, but it destroys the caged structure which leads to drop in tensile properties [7]. In this aspect, graphene or functionalized graphene has the potential to supersede CNT. The measured and theoretical properties of graphene are comparable with CNT [8], moreover, due to its flat structure, the strength translation towards matrix at different direction is possible (CNT has good tensile property only along its length) and matrix slippage problem can be minimized. Most of the groups working with graphene based polymer nanocom-

---

[*] Corresponding author, e-mail: amitbha1912@gmail.com

posites found improvements in mechanical properties [9, 10]. The mechanical and thermo mechanical properties of graphene oxide reinforced poly lactic-co-glycolic acid nanofiber mesh are significantly enhanced when only 1 and 2 wt% of graphene oxide were dispersed in it [11]. In a review on graphene based nanocomposites, Sengupta *et al*. [12] listed few graphene and high density polyethylene (HDPE) based nanocomposites showing increase in mechanical properties. Jiang and Drzal [13] found that the paraffin wax modification on graphene results in improved electrical conductivity and flexural properties than uncoated one for HDPE based nanocomposites. However, more research is required in this field to understand the interaction of graphene with polymer matrix. The basic problems are the dispersion and orientation of mono or few layered graphene in the polymer matrix and the interface between polymer matrices with graphene so that efficient load transfer is possible. The strength realization using graphene is not adequate till now; mainly because of the lack of proper inter-phase between graphene and polymer and due to the poor 'between-plane' strength of graphene causes slippage of multilayer graphene [12]. For these, graphene preparation, dispersion in polymer matrix and matrix-graphene load transfer need to be investigated. In this paper, reduced graphene oxide dispersed UHMWPE nanocomposite films are prepared in two different process routes. The produced films are characterized to correlate with their tensile and time dependant creep strain properties.

2. Experimental

2.1. Material

Graphite having particle size less than 10 μm was procured from Shanghai Yifan Graphite Co Ltd., China. UHMWPE powder having average molecular weight of 3×10^6 was supplied by Shanghai Lianle Chemical Co. Ltd., China. Ortho-dichlorobenzene (ODCB) and N, N′-dimethylformamide (DMF) were purchased from Aladdin Industrial Corporation and Shanghai Boer Chemical Reagent Co. Ltd., China, respectively. All other chemicals were supplied by Sinopharm Chemical Reagent Co. Ltd., China and used as received without further purification.

2.2. Preparation of graphite oxide (GO)

GO has been synthesized using Hummers method from graphite [14]. In short, 5 g of graphite and 10 g of sodium nitrate ($NaNO_3$) were added to 150 mL of concentrated sulfuric acid (H_2SO_4) with continuous stirring (500 rpm) for 30 min. The mixture was kept in ice bath to keep the temperature low and 15 g of potassium permanganate ($KMnO_4$) was added very slowly in it (extreme care has been taken as it is a highly exothermic reaction). The mixture was subjected to ultrasonic treatment (42 kHz) for 30 min and then kept for 3 h with stirring (500 rpm). It was carefully mixed with 200 mL de-ionized water to stop the reaction. 50 mL hydrogen peroxide (H_2O_2) was added to reduce the un-reacted $KMnO_4$. The mixture was centrifuged and washed twice with dilute hydrochloric acid. Then it was washed three times with de-ionized water and filtered with 0.2 μm acetate filter. The resulting GO was dried at 40°C for 60 h. To test the graphene yield, 100 mg GO was exfoliated and dispersed in de-ionized water with 30 min ultrasonic treatment and 1 h stirring (500 rpm) and 0.5 mL of phenylhydrazine was added at 90°C for reduction of graphene oxide. The reaction was allowed to continue for 4 h. After that, graphene was filtered, washed twice and dried for 4 h. The yield was approximately 60 wt%. However, for nanocomposites preparation, graphite oxide (GO) taken on weight basis was reported.

2.3. Preparation of nanocomposites

As solvent of UHMWPE and graphene dispersion media, 1:4 (v/v) mixtures of DMF and ODCB were selected. Graphene oxide and graphene forms stable dispersion in DMF [15] but DMF cannot dissolve UHMWPE. ODCB is a good solvent for UHMWPE, as well as CNT can disperse reasonably well in it [16]. Exfoliation of graphite in ODCB has also been reported [17]. So, this solvent was chosen. However, it has been observed that the exfoliation and dispersion of GO is not very good in ODCB. For this, a combination solvent system of DMF and ODCB was used. Two routes were followed for dispersion of reduced graphene oxide in polymer:

Route 1 (R-1) or the pre-reduction method: 1 wt% (on weight of UHMWPE) GO was exfoliated and dispersed in DMF and ODCB (1:4 ratio) by ultrasonic treatment (30 min), followed by reduction with phenylhydrazine for 4 h with continuous stirring (500 rpm). Subsequently, 3% (w/v on total solvent taken) UHMWPE powder was added slowly at 140°C with continuous stirring for 2 h till it completely dissolved.

A variation of R-1 was also tried as follows: GO was exfoliated in DMF, followed by reduction with phenylhydrazine for 4 h with continuous stirring (500 rpm). UHMWPE powder was added slowly at 140°C in ODCB (taken separately as 4 times of DMF on volume basis) with continuous stirring (500 rpm) for 2 h till it was completely dissolved. Subsequently, the graphene dispersion was added into it. However, as viscosity was very high, this process did not give good dispersion of graphene in polymer solution, so it was not used.

Route 2 (R-2) or *in situ* reduction method: 1 wt% (on weight of UHMWPE) GO was exfoliated and dispersed in DMF and ODCB (1:4 ratio) with 30 min ultrasonic treatment and 1 h stirring (500 rpm), followed by addition of small amount of UHMWPE (twice the weight of GO) at 140°C, stirring continued till the polymer dissolved, followed by reduction with phenylhydrazine for 4 h. Subsequently, remaining UHMWPE powder was added slowly at 140°C with continuous stirring for 2 h till it completely dissolved. The dispersion contained total 3% UHMWPE (w/v on total solvent taken).

Schematic representations of both the process routes are described in Figure 1. In the case of route 2 or *in situ* reduction, Small amount of polymer is added in the system before reduction as reduced graphene oxide tends to re-agglomerate in the media. The added polymer is expected to hinder the graphene agglomeration after reduction. The total amount of UHMWPE has not been added as the viscosity will be very high so dispersion would be difficult and create disturbance in reduction process. Again, the long stirring for 4 h during graphene oxide reduction would lead to gel break down of UHMWPE [18].

In both the process routes, after complete dissolution, the polymer-graphene dispersions were cast into films and dried at 70°C for 48 h. The average thickness of films was found to be 60 µm.

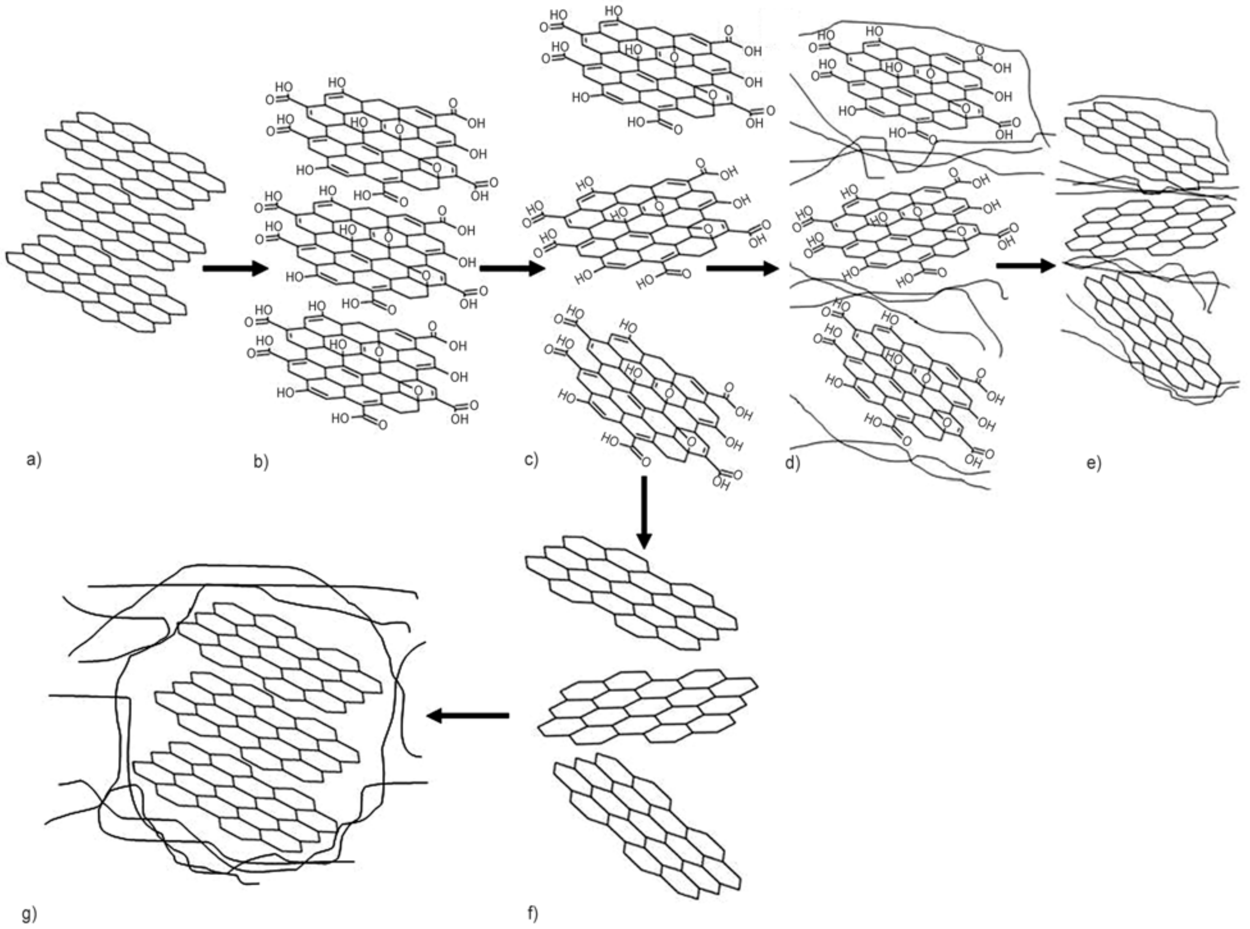

Figure 1. Schematic representation of process routes starting from graphite (a), graphite oxide (b), graphene oxide (c), polymer chains around graphene oxide as in route 2 (d), polymer coated graphene after *in situ* reduction in route 2 (e), pre-reduction of graphene in route 1 (f) and graphene embedded in polymer as in route 1 (g)

2.4. Characterization

Raman spectroscopic studies were carried out in 514 nm laser source of inVia Raman spectroscope from Renishaw, UK. High resolution transmission electron microscope (HRTEM model: JEM 2100) from Jeol Inc., Japan was used for imaging and selected area electron diffraction (SAED) studies of graphene and graphene oxide (at 200 kV) and nanocomposite films (at 100 kV). X ray powder diffractometer (D/Max-2550 PC made by Rigaku, Japan) was used to register the X-ray patterns of the particles. Differential scanning calorimeter (DSC) tests were carried out in DSC Q20 produced by TA instruments at a scanning rate of 10°C/min. Instron 4206 universal tester by Instron Engineering Corp. USA was used for tensile tests. Sample strips with 2 mm width have been cut and 10 samples were tested in each case at a speed of 5 mm/min with a jaw separation distance of 20 mm. The tensile modulus was calculated at initial straining of 0.5 to 0.7%. Maximum strain at break was measured as percentage ratio of extension to initial test length (jaw separation distance). For creep tests, the film strips of same dimension were loaded with 20, 40, 60 and 80% of their average maximum strength. The strains as percentage ratio of extension to initial test length of 20 mm have been recorded at different test time. Four samples were tested in each case. Both the tensile and creep tests were carried out at laboratory condition of 27°C and 65% relative humidity.

3. Results and discussions

3.1. Characterization of graphene-UHMWPE nanocomposites

3.1.1. Raman spectroscopy

Figure 2 illustrates the Raman spectrum of graphite, graphene, UHMWPE film and two nanocomposite films made by two different process routes. D (~1330 cm^{-1}) and G (~1580 cm^{-1}) band peaks of graphite and graphene are shown. The D peak, exists in defected graphene, is due to first order zone boundary phonons. The chemically converted graphene includes significant amount of defects which causes enhanced relative intensity of D band with respect to G band [17]. The relative peak intensity of D band to G band is often used to estimate the amount

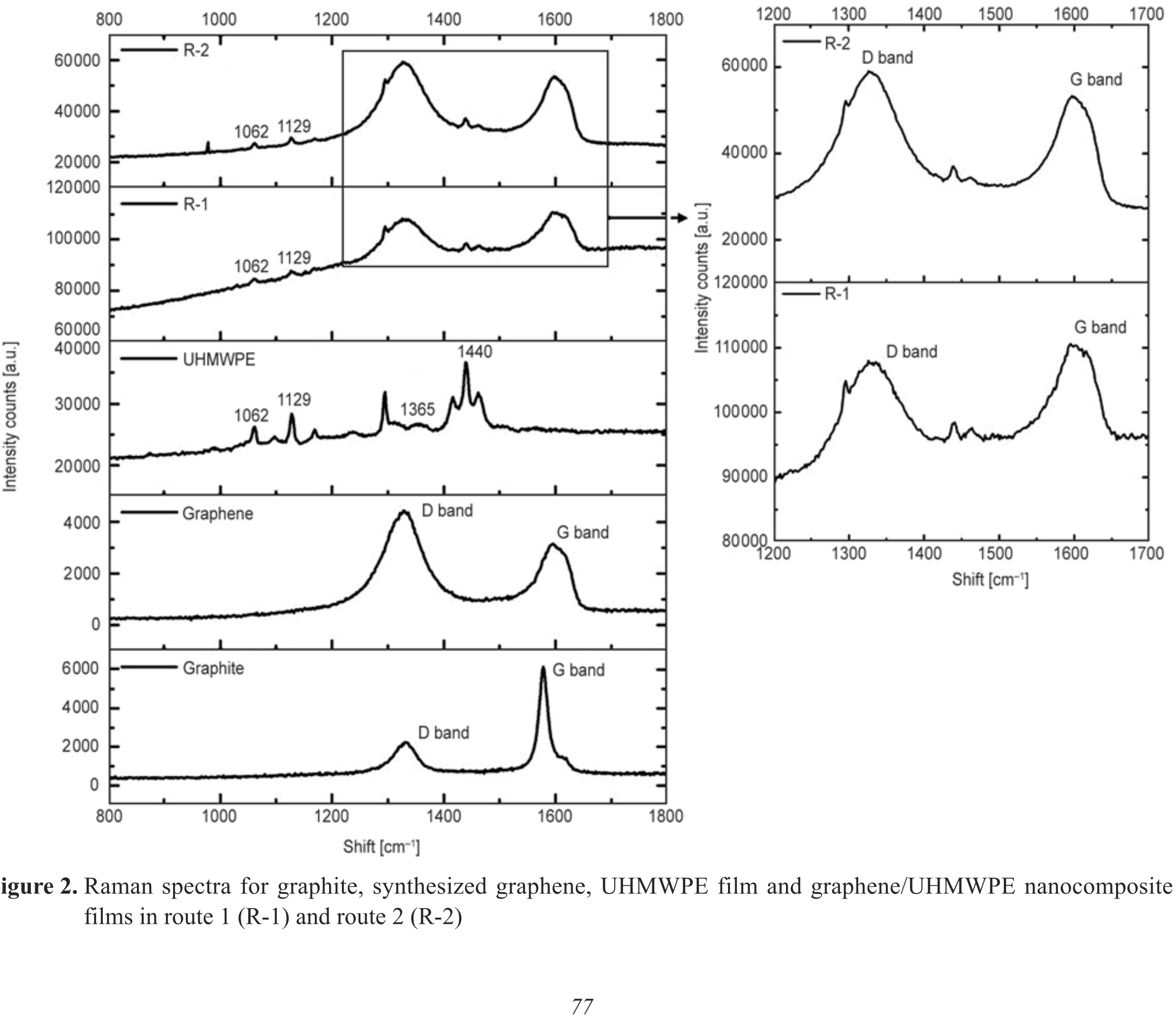

Figure 2. Raman spectra for graphite, synthesized graphene, UHMWPE film and graphene/UHMWPE nanocomposite films in route 1 (R-1) and route 2 (R-2)

of defects in carbon materials. The G band to D band ratio gives an idea of in-plane crystallite size (*La*) [19]. For the reduced graphene oxide synthesized in this work, it is approximately 2.7 nm. The C-C asymmetric and symmetric stretching bands (1062 and 1129 cm^{-1}) of UHMWPE lie at the same position for both the nanocomposite films produced by R-1 and R-2 as shown in Figure 2. This proves the unstressed condition of nanocomposite films or the stress levels are same as the pure film [20]. The relative peak intensities of G and D band peaks of graphene differ in the nanocomposite films produced by two routes. After baseline correction, the relative peak intensity of G band to D band of graphene is lower in the case of R-2 (ratio 0.82, *La* = 3.6 nm) which indicates less in-plane crystal size of graphene than in the case of R-1 (ratio 1.22, *La* = 5.4 nm). The D band intensity increases with the thinning of graphene and is absent for bulk graphite as defects can be observed more easily in thinner flakes [21]. So, more intense D band for nanocomposite film made by route 2 (R-2) can be attributed to better exfoliation of graphene in the polymer matrix. The reduction of graphene oxide before addition of polymer leads to re-agglomeration of graphene in route 1 while the polymer chains hinder the graphene to form stacking in the case of R-2. Hence, *in situ* reduction method (R-2) results

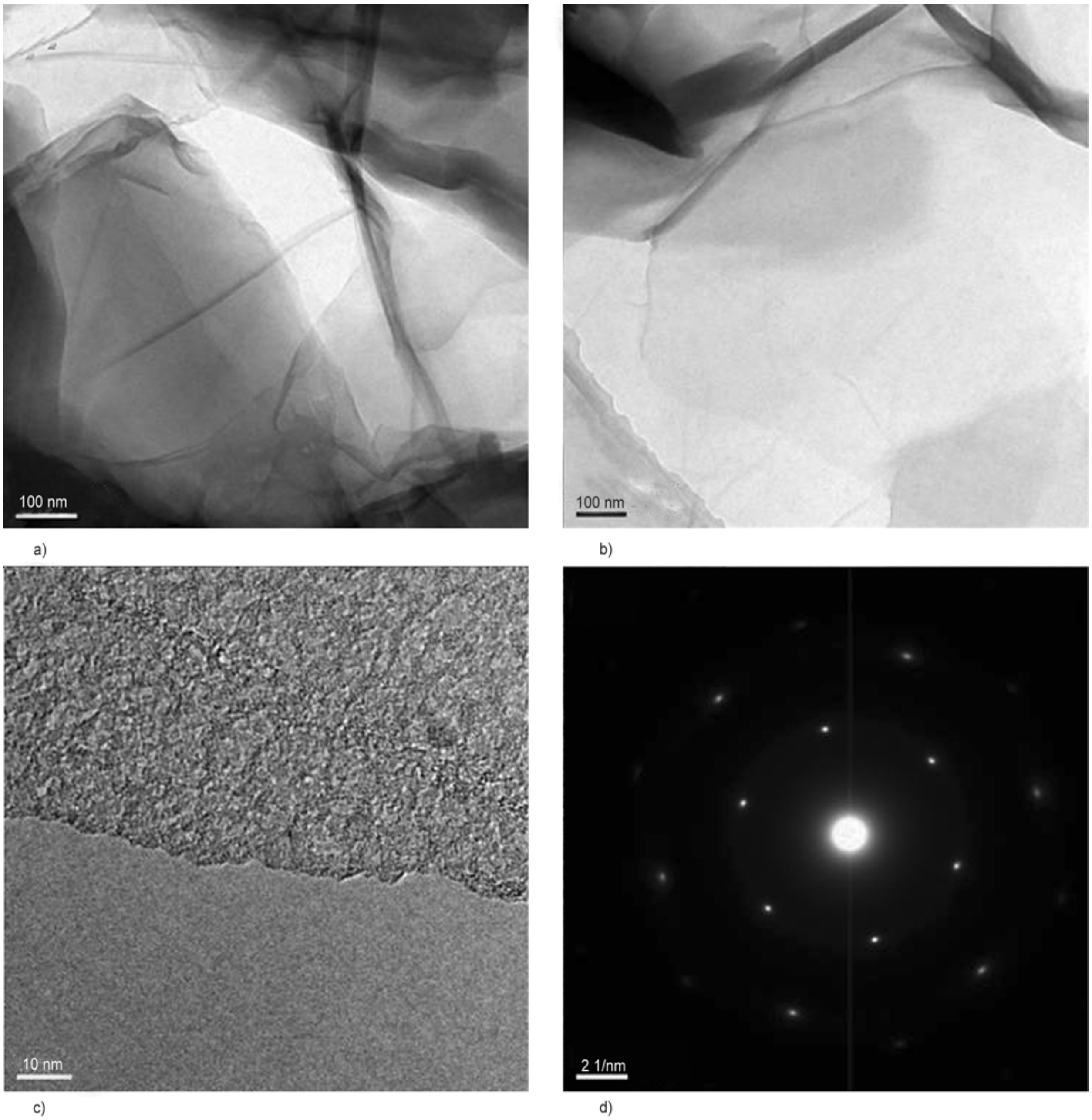

Figure 3. TEM images of graphene oxide (a), graphene ((b) and (c)) and corresponding SAED pattern of graphene (d)

in thinner graphene flakes and more dispersion of graphene in the polymer matrix which consequently shows more intense D band Raman peak as compared to pre-reduction method (R-1).

3.1.2. Transmission electron microscope (TEM)

Figure 3 shows the transmission electron microscope images of graphene oxide and graphene. After reduction, graphene sheets are mostly monolayers. The SAED pattern (Figure 3d) taken on the area mentioned in Figure 3c confirms the monolayer graphene [22, 23]. The synthesized graphene is folded and crinkled at different places. Existence of bi- or tri- layered flakes is also observed from SAED pattern taken in other areas. Hence, it can be concluded that the synthesized graphene is mostly monolayer while some few layered graphene also exist. The few layered graphene should also exfoliate to monolayer as it experiences further ultrasonic treatment and stirring during nanocomposite preparation.

TEM images and corresponding SAED patterns of the graphene/UHMWPE nanocomposites produced by two routes have been shown in Figure 4. The thin dark lines observed throughout the scanned area of both nanocomposite films (Figure 4a and 4c) can

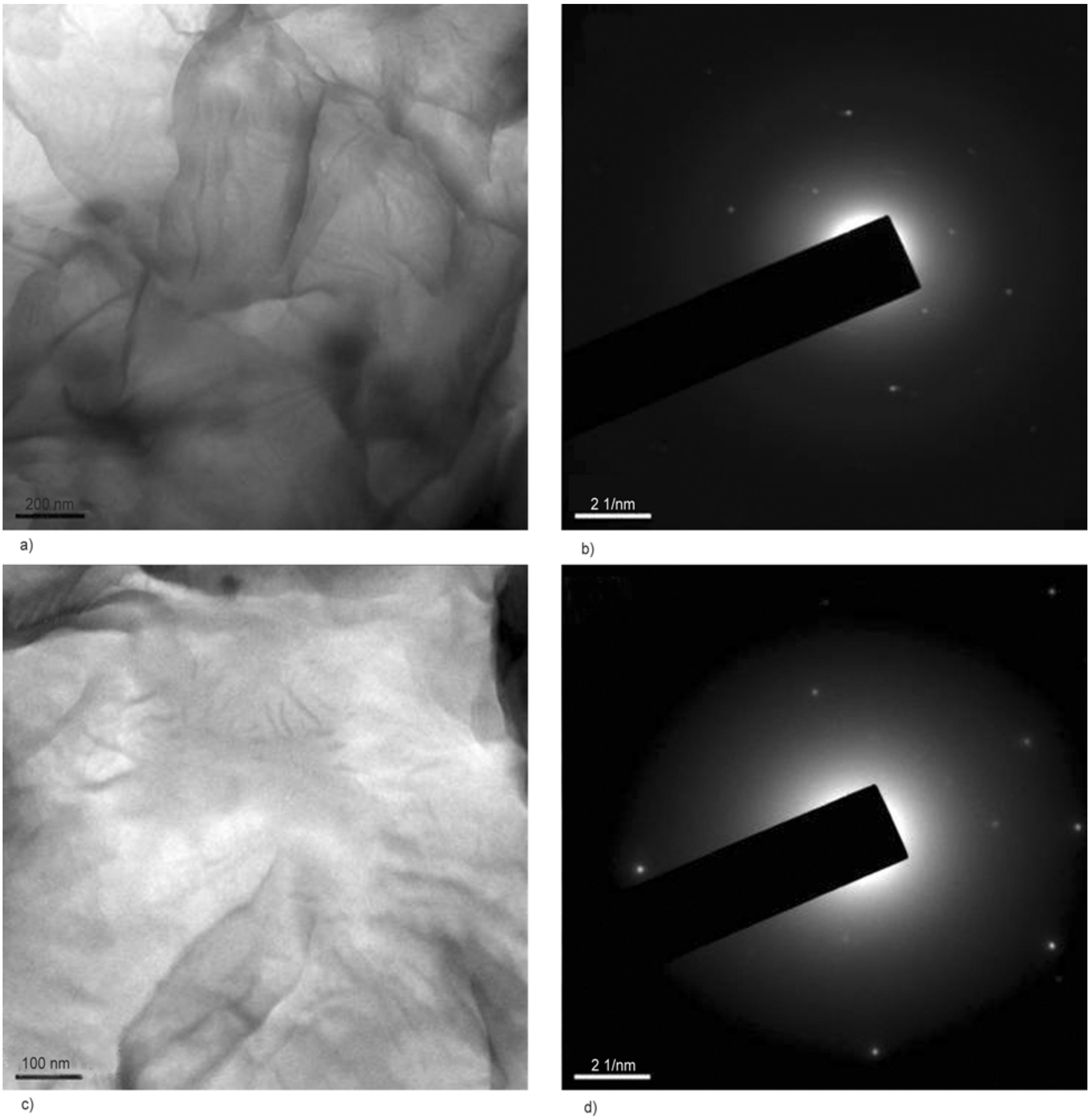

Figure 4. TEM images ((a) and (c)) and corresponding SAED patterns of graphene-UHMWPE nanocomposites by R-1 ((a) and (b)) and R-2 ((c) and (d))

be attributed to graphene. However, it is noteworthy to mention that the crinkles developed by the ultra thin polymer film may also contribute to some of these lines. The TEM images show almost comparable dispersion of graphene in both the nanocomposites. From the Raman G band to D band ratio, R-2 or *in situ* reduction method results in thinner graphene flakes, hence, better dispersion of graphene in the resulted nanocomposite film. The SAED patterns reveal the difference in crystalline content. The patterns confirm the semi-crystalline nature of nanocomposite film produced by R-1 or pre-reduction method (Figure 4b) while amorphous content is very high in R-2 (Figure 4d). So, it can be concluded from the intensity of crystal spots and diffused amorphous rings that the crystalline content is less for *in situ* reduced nanocomposite film.

3.1.3. Wide angle X-ray

Figure 5 shows the wide angle X-ray curves of the three samples. The crystalline content estimated from the curves is 39.8% for pure UHMWPE film and almost same in 1 wt% graphene dispersed nanocomposite film produced through R–1 (39.6%). However, it is reduced to 32% in nanocomposite film produced by R-2. This may be attributed to the better exfoliated state of graphene which restricts the polymer chains to organize in particular arrangement and hinders the crystallization of polymer chains.

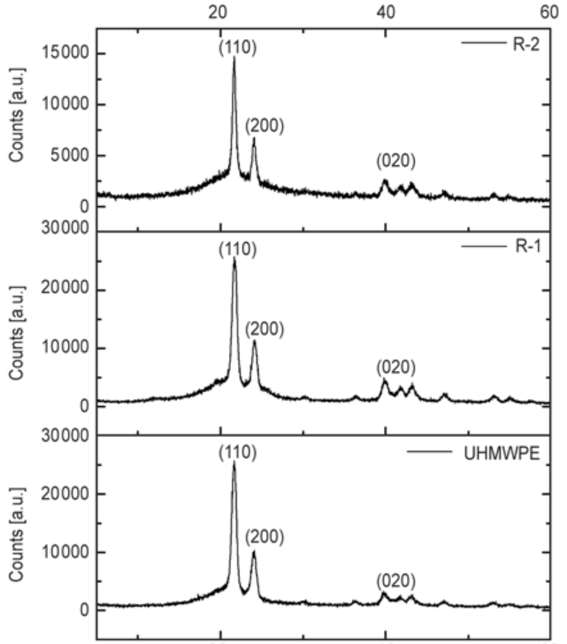

Figure 5. Wide angle X-ray curves for UHMWPE film, nanocomposite films produced by route 1 (R-1) and route 2 (R-2)

3.1.4. Differential scanning calorimetry (DSC)

Considering the heat of fusion for 100% crystalline UHMWPE as 289 J/g [24], the crystallinity results can be obtained from the DSC curves. The estimated crystalline content for pure UHMWPE film is 41%, for nanocomposite film produced by R-1 is 39% and for nanocomposite film produced by R-2 is 35% as calculated from the DSC curves shown in Figure 6. The results are almost similar as that of X-ray crystallinity data. So, the graphene obstructs the crystal formation of polymer chains in nanocomposite film produced by *in situ* reduction method or R-2. Peak melting temperature is almost same in all three films, however, the onset of melting peak shifted to higher side in the case of R-1 and the peak width is much less, which indicates less variation in crystal size for pre-reduction method or R-1.

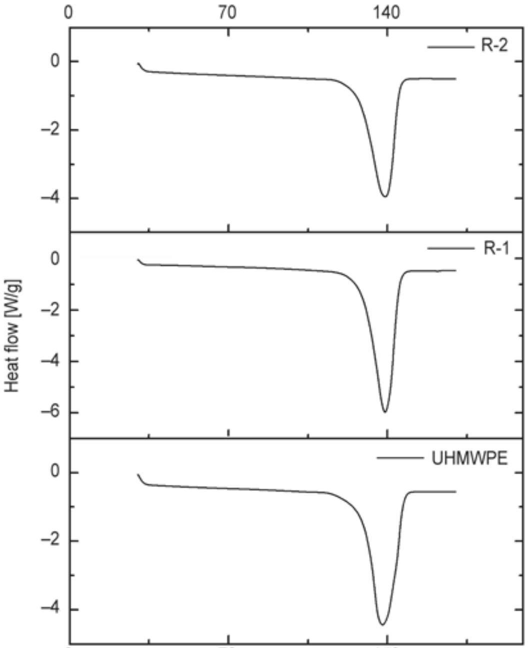

Figure 6. DSC curves for UHMWPE film, nanocomposite films produced by route 1 (R-1) and route 2 (R-2)

3.2. Mechanical behavior of graphene-UHMWPE nanocomposites

3.2.1. Tensile test

The tensile test results are shown in Table 1. The tensile modulus calculated at initial straining (from 0.5 to 0.7%) shows good increase in R-1 or pre reduced graphene based nanocomposite film than

Table 1. Tensile test results of pure and nanocomposite films (average of 10 readings with standard error)

Sample name	Modulus [MPa] ± standard error (n = 10)	Maximum strength [MPa] ± standard error (n = 10)	Maximum strain [%] ± standard error (n = 10)
UHMWPE	864±7	12.6±2.0	58±5
R-1	1236±17	22.2±1.5	28±4
R-2	416±23	17.1±2.0	41±5

the pure one (from 864 to 1236 MPa). However, it is decreased significantly in R-2 produced nanocomposite film. In both the process routes, use of 1 wt% GO significantly improves the tensile strength of the UHMWPE and reduces the breaking extension. R-1 supersedes R-2 in terms of strength; however, the strain to break is also reduced. As compared to the pure film, the maximum strength has been increased almost twice in nanocomposite film produced by pre-reduction method or R-1 (from 12.6 to 22.2 MPa) and the strain is reduced to 28 from 58%. For nanocomposite film by R-2, the strain is reduced to 41% with some improvement in strength (17.1 MPa). So, network hardening of polymer matrix is introduced by graphene in both nanocomposite films and the effect is more prominent in the case of R-1. The results match with the observations made during characterization of the film. The low tensile modulus, high extension and low strength improvement are attributed to the lower crystalline content of nanocomposite film prepared by *in situ* reduction (R-2) while the high crystallinity as well as the influence of graphene leads to very high reduction in maximum strain for R-1 nanocomposite film. Representative tensile test curves of three types of samples are shown in Figure 7. As the films are not drawn, plateau zones are observed after maximum stress till they fail. The zone length is significantly reduced in both nanocomposite films which indicate network hardening at high stress level; but, R-2 shows more extension before stress relaxation near break. The tensile modulus (measured at low stress level) of *in situ* reduced graphene based nanocomposite film is even less than the pure UHMWPE film because of its higher amorphous content. The chain stretching and reordering happen only at higher stress level where the strength contribution of graphene results in higher tensile strength of the nanocomposite film (produced by R-2) than the pure one. Hence, the *in situ* reduced nanocomposite film has more ductility and significantly less modulus than the pre-reduced one. The incorporation of graphene in polymer matrix by R-2 method inhibits the polymer crystallization, thus lowering the crystalline content which causes less strength improvement, less modulus and more ductility as compared to nanocomposite films produced by R-1 method.

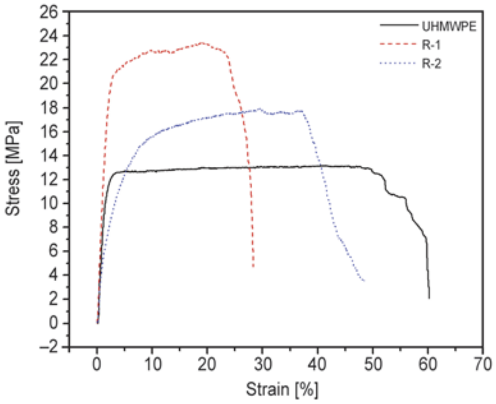

Figure 7. Representative stress-strain curve of UHMWPE film, nanocomposite films by R-1 and R-2

3.2.2. Creep test

Creep tests have been carried out at different loading on films upto 72 h as shown in Figure 8. The test results are coded as 'X-Y' where X is sample name (coded as PE for UHMWPE film, R-1 for nanocomposite film produced by pre-reduction or route 1 method and R-2 for nanocomposite film produced by *in situ* or route 2 method) and Y is load percentage of the average maximum load (as of Table 1) applied on the sample throughout the creep test. The results show that at 20% loading, strains of pure and nanocomposite films are almost comparable (Figure 8a) at the beginning while over the extended period of time the strain is very high for pure film. The nanocomposite films produced by R-1 and R-2 shows less creep strain. The difference is more prominent at 40% loading (Figure 8b). The tendency to creep strain is very high for pure UHMWPE film as compared to nanocomposite films at that laoding. The increase in load to 60% of the breaking load leads to failure in 4 h in the case of pure film, while nanocomposite films fail after 24 h (Figure 8c). The strain on creep is much less in the case of both nanocomposite films, however, nanocomposite film produced by pre-reduction or R-1 method shows better results than *in situ* reduced (R-2)

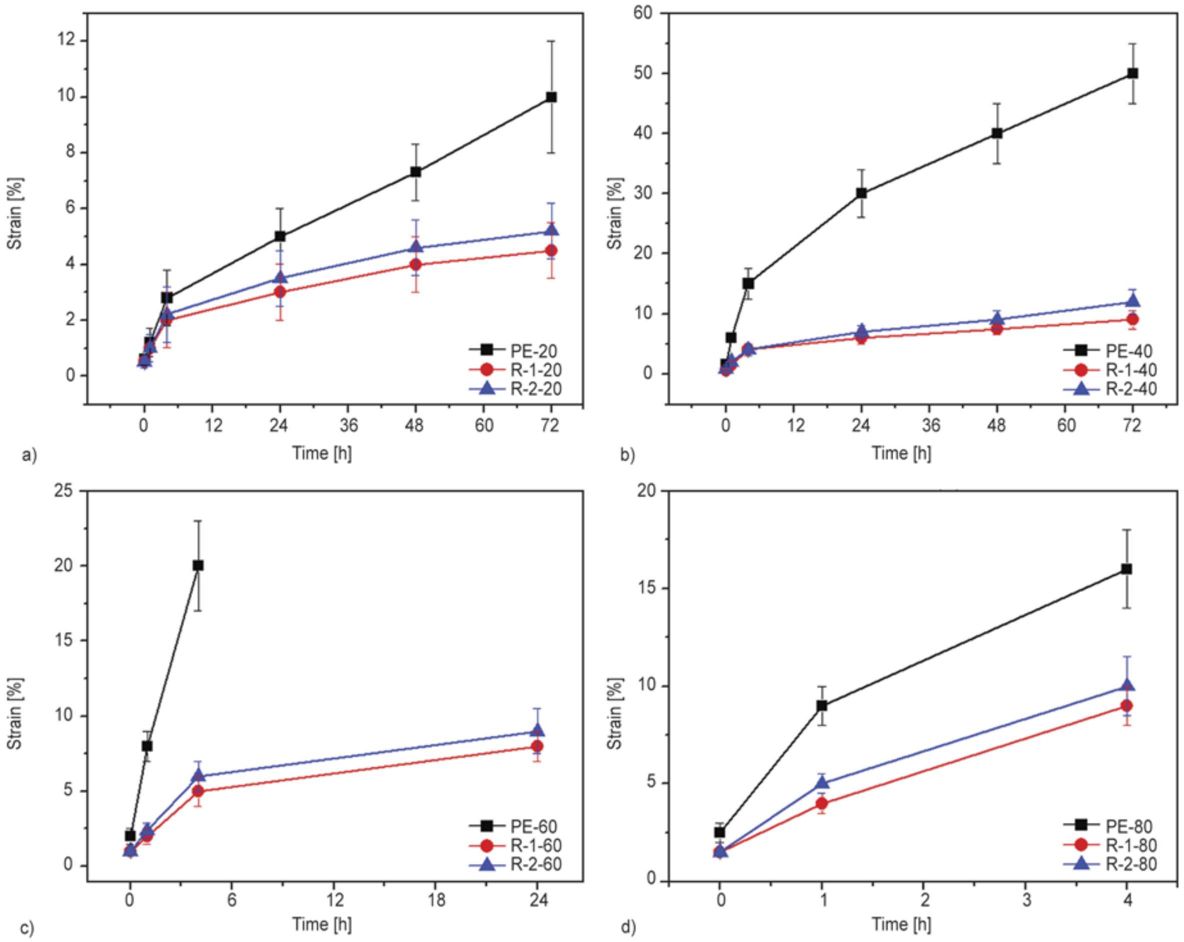

Figure 8. Strain of pure films (PE) and nanocomposite films from route 1 (R-1) and route 2 (R-2) with time under 20% (a), 40% (b), 60% (c) and 80% (d) load of average maximum load

one at all loadings. The results are similar in nature to tensile test results and hence, it can be concluded that the polymer network hardening is the reason behind the low creep for the nanocomposite films. The strain rate is low for the samples undergoing the such creep test. Hence, polymer samples get sufficient time to reorder its chains, distribute the stress and transfer the load to the reinforcing nanoparticles. This leads to significant improvement in reduction of creep strain for both the nanocomposite films.

A scheme to explain the morphology and properties of nanocomposite films is shown in Figure 9. All the solution cast films are semi crystalline in nature, however, the crystals are not oriented to a particular direction as there is no stretching or drawing. The crystals grow with the evaporation of solvents till they are obstruced either by neighbouring crystals or by nanoparticles (here graphene nanoplatelets). The process continues till complete solidification. The entangled molecular chains having no particular orientation contribute to its amorphous fraction. The nanoparticles reinforce the amorphous region of polymer nanocomposites. In the case of pre-reduced graphene dispersed nanocomposite film, the graphene nanoplatelets are well distributed in

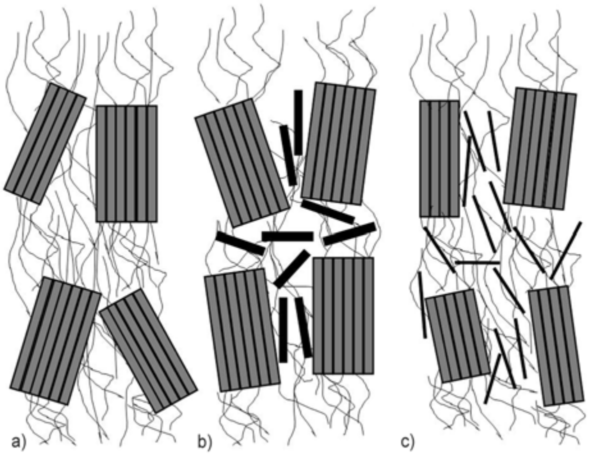

Figure 9. Schematic of proposed morphology for pure UHMWPE film (a), nanocomposite film by pre-reduction method (b) and nanocomposite film by *in situ* reduction method (c)

the polymer solution, hence, the size distribution of crystals are less as compared to pure one as shown in Figure 9b. The better or fully exfoliated graphene has higher surface area than the less exfoliated one, so it restricts the polymer chains more than the multilayer graphene sheets. The interference of graphene prevents the polymer chains to form the regular crystalline array as shown in Figure 9c. When subjected to tensile testing, the entangled polymer chains in amorphous region get stretched and the load is transferred to nanoparticles which leads to increase in maximum strength. However, the ductility of the film is reduced significantly as the chain mobility is restricted. The high amorphous content of the *in situ* reduced nanocomposite film leads to less tensile modulus and more ductility as compared to pre-reduced one. The ductility of R-2 produced nanocomposite film never achieves the level of pure UHMWPE film due to the nanofiller constrain and the tensile molulus at low stress level is also less as it is less cryslline in nature.

4. Conclusions

Graphene can be used as reinforcement for UHMWPE to improve its tensile property and to reduce its creep behavior. The dispersion of graphene in polymer matrix by the pre-reduction method may not be as good as *in situ* reduction method, but the latter leads to significant loss in crystallinity due to restriction in polymer chains movements by the exfoliated graphene flakes. In the *in situ* reduction process, the exfoliated graphene impedes the crystalline arrangement for the polymer which in turn decreases the tensile modulus, increases strain at break as well as the creep strain as compared to pre-reduced graphene based nanocomposite. The network hardening of matrix is more in pre-reduction or the first route of nanocomposite film production (strain reduced to 28%). The strength enhancement in first route (more than 76% improvement as compared to pure film) is also much better than the second route due to reinforcement by graphene as well as higher crystalline content. Hence, the crystalline content is also a significant contributing factor for improvement in tensile properties along with the dispersion of graphene. It can be concluded that the pre-reduction method is suitable for high strength and creep resistant applications while *in situ* reduction method may perform better for applications where more ductility is required. The underlying mechanism of graphene dispersion at its different concentration needs to be explored by further characterizations. More investigation in this route by using functionalized graphene and drawing of films will be expected and interesting.

Acknowledgements

Authors like to express their heartiest acknowledgement to Dr. Baldev Raj, President Research, PSG Institutions, for his continuous encouragement and help to facilitate this work. Authors also express their deep gratitude to management of PSG Institutions and College of Materials and Engineering (CMSE), Donghua University for their support as well as the financial support from the National Natural Science Foundation for Distinguished Young Scholar of China (50925312) and Natural Science Foundation of China (51273040).

References

[1] Kavesh S., Prevorsek D. C.: Ultra high strength, high modulus polyethylene spectra fibers and composites. International Journal of Polymeric Materials and Polymeric Biomaterials, **30**, 15–56 (1995).
DOI: 10.1080/00914039508031459

[2] Li C. S., Zhan M. S., Huang X. C., Zhou H.: Degradation behavior of ultra-high molecular weight polyethylene fibers under artificial accelerated weathering. Polymer Testing, **31**, 938–943 (2012).
DOI: 10.1016/j.polymertesting.2012.06.009

[3] Bracco P., Brunella V., Luda M. P., Zanetti M., Costa L.: Radiation-induced crosslinking of UHMWPE in the presence of *co*-agents: Chemical and mechanical characterisation. Polymer, **46**, 10648–10657 (2005).
DOI: 10.1016/j.polymer.2005.08.095

[4] Ramanathan T., Abdala A. A., Stankovich S., Dikin D. A., Herrera-Alonso M., Piner R. D., Adamson D. H., Schniepp H. C., Chen X., Ruoff R. S., Nguyen S. T., Aksay I. A., Prud'Homme R. K., Brinson L. C.: Functionalized graphene sheets for polymer nanocomposites. Nature Nanotechnology, **3**, 327–331 (2008).
DOI: 10.1038/nnano.2008.96

[5] Coleman J. N., Khan U., Blau W. J., Gun'ko Y. K.: Small but strong: A review of the mechanical properties of carbon nanotube–polymer composites. Carbon, **44**, 1624–1652 (2006).
DOI: 10.1016/j.carbon.2006.02.038

[6] Andrews R., Weisenberger M. C.: Carbon nanotube polymer composites. Current Opinion in Solid State and Materials Science, **8**, 31–37 (2004).
DOI: 10.1016/j.cossms.2003.10.006

[7] Ma P-C., Siddiqui N. A., Marom G., Kim J-K.: Dispersion and functionalization of carbon nanotubes for polymer-based nanocomposites: A review. Composites Part A: Applied Science and Manufacturing, **41**, 1345–1367 (2010).
DOI: 10.1016/j.compositesa.2010.07.003

[8] Kuilla T., Bhadra S., Yao D., Kim N. H., Bose S., Lee J. H.: Recent advances in graphene based polymer composites. Progress in Polymer Science, **35**, 1350–1375 (2010).
DOI: 10.1016/j.progpolymsci.2010.07.005

[9] Arai T., Tominaga Y., Asai S., Sumita M.: A study on correlation between physical properties and interfacial characteristics in highly loaded graphite–polymer composites. Journal of Polymer Science Part B: Polymer Physics, **43**, 2568–2577 (2005).
DOI: 10.1002/polb.20543

[10] Song P., Cao Z., Cai Y., Zhao L., Fang Z., Fu S.: Fabrication of exfoliated graphene-based polypropylene nanocomposites with enhanced mechanical and thermal properties. Polymer, **52**, 4001–4010 (2011).
DOI: 10.1016/j.polymer.2011.06.045

[11] Yoon O. J., Jung C. Y., Sohn I. Y., Kim H. J., Hong B., Jhon M. S., Lee N-E.: Nanocomposite nanofibers of poly(D, L-lactic-co-glycolic acid) and graphene oxide nanosheets. Composites Part A: Applied Science and Manufacturing, **42**, 1978–1984 (2011).
DOI: 10.1016/j.compositesa.2011.08.023

[12] Sengupta R., Bhattacharya M., Bandyopadhyay S., Bhowmick A. K.: A review on the mechanical and electrical properties of graphite and modified graphite reinforced polymer composites. Progress in Polymer Science, **36**, 638–670 (2011).
DOI: 10.1016/j.progpolymsci.2010.11.003

[13] Jiang X., Drzal L. T.: Improving electrical conductivity and mechanical properties of high density polyethylene through incorporation of paraffin wax coated exfoliated graphene nanoplatelets and multi-wall carbon nano-tubes. Composites Part A: Applied Science and Manufacturing, **42**, 1840–1849 (2011).
DOI: 10.1016/j.compositesa.2011.08.011

[14] Hummers Jr. W. S., Offeman R. E.: Preparation of graphitic oxide. Journal of the American Chemical Society, **80**, 1339 (1958).
DOI: 10.1021/ja01539a017

[15] Dreyer D. R., Park S., Bielawski C. W., Ruoff R. S.: The chemistry of graphene oxide. Chemical Society Reviews, **39**, 228–240 (2010).
DOI: 10.1039/B917103G

[16] Bahr J. L., Mickelson E. T., Bronikowski M. J., Smalley R. E., Tour J. M.: Dissolution of small diameter single-wall carbon nanotubes in organic solvents? Chemical Communications, **2**, 193–194 (2001).
DOI: 10.1039/B008042J

[17] Hamilton C. E., Lomeda J. R., Sun Z., Tour J. M., Barron A. R.: High-yield organic dispersions of unfunctionalized graphene. Nano Letters, **9**, 3460–3462 (2009).
DOI: 10.1021/nl9016623

[18] Narh K. A., Barham P. J., Keller A.: Effect of stirring on the gelation behavior of high-density polyethylene solutions. Macromolecules, **15**, 464–469 (1982).
DOI: 10.1021/ma00230a051

[19] Subrahmanyam K. S., Vivekchand S. R. C., Govindaraj A., Rao C. N. R.: A study of graphenes prepared by different methods: Characterization, properties and solubilization. Journal of Materials Chemistry, **18**, 1517–1523 (2008).
DOI: 10.1039/B716536F

[20] Bakshi S. R., Tercero J. E., Agarwal A.: Synthesis and characterization of multiwalled carbon nanotube reinforced ultra high molecular weight polyethylene composite by electrostatic spraying technique. Composites Part A: Applied Science and Manufacturing, **38**, 2493–2499 (2007).
DOI: 10.1016/j.compositesa.2007.08.004

[21] Ni Z., Wang Y., Yu T., Shen Z.: Raman spectroscopy and imaging of graphene. Nano Research, **1**, 273–291 (2008).
DOI: 10.1007/s12274-008-8036-1

[22] Suk J. W., Kitt A., Magnuson C. W., Hao Y., Ahmed S., An J., Swan A. K., Goldberg B. B., Ruoff R. S.: Transfer of CVD-grown monolayer graphene onto arbitrary substrates. ACS nano, **5**, 6916–6924 (2011).
DOI: 10.1021/nn201207c

[23] Ferrari A. C., Meyer J. C., Scardaci V., Casiraghi C., Lazzeri M., Mauri F., Piscanec S., Jiang D., Novoselov K. S., Roth S., Geim A. K.: Raman spectrum of graphene and graphene layers. Physical Review Letters, **97**, 187401/1–187401/4 (2006).
DOI: 10.1103/PhysRevLett.97.187401

[24] Andjelić S., Richard R. E.: Crystallization behavior of ultrahigh molecular weight polyethylene as a function of in vacuo γ-irradiation. Macromolecules, **34**, 896–906 (2001).
DOI: 10.1021/ma0008241

eXPRESS Polymer Letters Vol.8, No.2 (2014) 85–94
Available online at www.expresspolymlett.com
DOI: 10.3144/expresspolymlett.2014.11

Preparation and characterization of biopolymers comprising chitosan-grafted-ENR via acid-induced reaction of ENR50 with chitosan

M. R. H. Mas Haris[1*], *G. Raju*[1,2]

[1]School Chemical Sciences, Universiti Sains Malaysia 11800 Minden, Penang, Malaysia
[2]Malaysian Rubber Board, 1458 Jalan Ampang, 50450 Kuala Lumpur, Malaysia

Received 20 July 2013; accepted in revised form 26 September 2013

Abstract. This paper describes the first detailed tailored-approach for the preparation of biopolymers comprising chitosan (CTS) grafted onto the backbone of epoxidized natural rubber (CTS-g-ENR). In a typical experiment, appropriate amount of CTS and $AlCl_3{\cdot}6H_2O$ was added to a specified amount of ENR50 (ENR with about 50% epoxy content) dissolved in a dual-solvent consisting of 1,4-dioxane and water (97.5:2.5% v/v) and the resulting mixture refluxed with continuous stirring for 6 hours. Nuclear magnetic resonance (NMR) spectral analysis of a biocomposite, CTS-g-ENR-P1, revealed that its epoxy content is 22.36% which is considerably lower than 44.93% as determined for ENR50-control (ENR50 derivative obtained under similar experimental condition but in the absence of CTS). This means that the grafting of CTS onto the backbone of ENR had occurred. The revelation is affirmed by the presence of the characteristic absorption bands of CTS and ENR, and the appearance of new bands at 1219, 902 and 733 cm^{-1} in the Fourier transform infrared (FTIR) spectrum of CTS-g-ENR-P1. Further evidence that CTS had been successfully grafted onto the backbone of ENR can be deduced and described in this paper from the data obtained by means of Differential Scanning Calorimetric analysis, Thermogravimetric analysis and Variable Pressure Scanning Electron Microscopy.

Keywords: *biopolymers, chitosan, epoxidized natural rubber*

1. Introduction

Chitin is a linear biopolymer and the second most abundant natural polysaccharide after cellulose [1]. The usual commercially available chitin is typically extracted from crab and shrimp shells. Chitosan is derived from chitin [2]. It is composed of predominantly α(1→4)-linked 2-amino-2-deoxy-β-D-glucopyranose with some amount of, 2-acetamido-2-deoxy-D-glucopyranose sugars, depending on the degree of N-deacetylation [3–5]. Due to the presence of the primary amino (C-2), primary (C-6) and secondary (C-3) hydroxyl groups on each repeat unit, chitosan is indeed a multinucleophilic material that may undergo specific reaction with other materials that contain electrophilic sites. Chitosan is being used in a wide range of applications ranging from biomedical engineering, pharmaceutical and cosmetic products to water treatment and plant protection [6]. Being a natural polysaccharide, chitosan exhibits high biodegradability but have poor mechanical properties. As such, modification of polymers that possess excellent thermal and mechanical parameters with chitosan may result in the production of a new class of polymeric materials exhibiting not only desired biodegradability but also good physicochemical and mechanical properties [7].

Incorporation of chitosan in the matrices of elastomers is of interest to researchers in areas that

---

[*]Corresponding author, e-mail: mas1@usm.my

involve the utilization of natural rubber or its derivatives and chitosan [8–16]. Of special interest to our current work, Lertwattanaseri *et al.* [13] reported the preparation of a novel model case of bionanocomposites comprising nanofibrous chitosan bonded to the backbone of epoxidized natural rubber (ENR) via both amino and hydroxyl groups. Confirmation of the proposed structure for the ENR–chitosan bionanocomposite was done by qualitative and quantitative FTIR techniques. Considering the nature of the reactivity of the hydroxyl and amino groups of chitosan, we believe the proposed structure is inconclusive. Very recently, Riyajan and Sukhlaaied reported the preparation of ENR-g-chitosan involving the reaction of chitosan radicals with ENR molecules using potassium persulphate ($K_2S_2O_8$) as an initiator [16]. The chemical structure of the ENR-g-chitosan, specifically the presence of ether linkage in the biopolymers, was confirmed by ^{1}H-NMR and ATR-FTIR.

Chitosan is soluble in acidic aqueous media [17, 18] whereas ENR, being hydrophobic in nature, is not [19]. This is the likely reason why there is very limited number of reports in the literature on homogenous (liquid-liquid phase) or semi-heterogeneous (liquid-solid phase) reaction condition involving chitosan and ENR. Furthermore, ENR is known to undergo ring-opening and double bond cleavage reactions [20–25]. To date, there is no report on the stability of the microstructure of ENR in conditions with different concentrations of acid. In view of this finding and as part of our interest to gain further insights on the physicochemical and mechanical properties of natural rubber latex films that were subjected to acid and/or base treatments [26–27], we have carried out the study on the effect of acidity on the stability of the molecular structure of ENR50. We found by means of NMR spectroscopy that the epoxidized isoprene units of ENR50 did not undergo significant ring-opening reaction in 1,4-dioxane acidified by the addition of dilute HCl or $AlCl_3{\cdot}6H_2O$ solution. This observation prompted us to investigate and hereby report our findings on the acid-induced reaction of ENR50 with chitosan.

2. Experimental

2.1. Materials

Epoxidized natural rubber with about 50% epoxy content (designated as ENR50) and with relative M_w of $3.8{\cdot}10^5$ g/mol was supplied by Malaysian Rubber Board, Kuala Lumpur, Malaysia. Chitosan (CTS) with with relative M_w of $1.0{\cdot}10^5$ g/mol was provided by Advanced Materials Research Centre at Kulim, Kedah, Malaysia. The degree deacetylation of the CTS was determined by a titration method [28] and found to be 96%. HCl and $AlCl_3{\cdot}6H_2O$ (purchased from Merck, Damstardt, Germany), 1,4-dioxane (Fisher, Malaysia) and NaOH (System Chemar) were used as received. Deuterated chloroform (Merck, 99.8% with 0.03% TMS) was used as the NMR solvent.

2.2. Instruments

^{1}H-NMR spectra of samples dissolved in $CDCl_3$ were recorded on a Bruker Avance-400 NMR spectrometer operating at 400.13 MHz. Tetramethylsiloxane (TMS) was used as the internal reference. Infrared spectra were recorded using a Perkin- Elmer 2000 Infrared Spectrometer with 16 scans at 4 cm^{-1} resolution. Solid ENR50 and CTS-g-ENR biopolymers were analysed directly using an attenuated total reflection (ATR) technique within the wave number range of 4000–650 cm^{-1}. CTS was analyzed in the form of KBr pellet (KBr: CTS = 98:2) within the wave number range of 4000 to 400 cm^{-1}. Differential Scanning Calorimetry (DSC) analysis was carried out using Perkin-Elmer Pyris-1 DSC, equipped with an internal cooler 2P-cooling accessory and calibrated using n-decane and indium. Samples (5–10 mg) were examined within an atmosphere of dry nitrogen gas maintained at a flow rate of 50 mL/min. All samples were annealed at a heating rate of 20°C/min (for both heating and quenching). For the first scan, samples were heated from –50°C up to at least 100°C and hold for about 2 minutes before cooling (at 20°C/min) back to –50°C. The second scan was performed after 2–5 minutes of waiting time. Thermal weight loss measurements were made using Perkin-Elmer TGA–7 thermogravimetric analyser. Testing was carried out under a stream of dry nitrogen gas (flow rate = 30 mL/min) at temperature range of 40 to 600°C with heating rate of 10°C/min. Weight of samples used was within 4–10 mg. Data of Variable Pressure Scanning Electron Microscopy (VPSEM) was obtained with the use of Carl Zeiss EVO LS 10 Scanning Electron Microscope. The morphology of the ENR50, CTS and CTS-g-ENR biopolymers were studied.

2.3. Methods

2.3.1. Exposure of ENR50 to different concentrations of HCl or $AlCl_3·6H_2O$

ENR50 (1.0 g) was dissolved in 95 mL 1,4-dioxane at room temperature inside a 250 mL two-necked round bottom flask equipped with a magnetic stirrer and a reflux condenser. Then 5 mL of 0.0001 M HCl was added dropwise and the resulting solution stirred for 4 hours. A sample of the solution (10 mL) was isolated every hour and placed in about 10 mL of chilled 0.0001 M sodium hydroxide to neutralize and precipitate the resulting ENR50 derivative. This derivative was isolated and washed with ample amount (>200 mL) of distilled water. Then it was placed in an oven with the temperature maintained at 50°C for 24 hours. The procedure was repeated but with the use of 0.001 M, 1.0 M and 3.0 M HCl. All resulting polymeric materials were analysed by NMR spectroscopy.

The experiment was repeated with the use of 0.75 and 0.30 g of aluminium chloride hexahydrate ($AlCl_3·6H_2O$) in lieu of HCl. ENR50 derivatives obtained after been exposed to $AlCl_3·6H_2O$ for 2, 4 and 24 hours were analysed by NMR spectroscopy.

2.3.2. Reaction of chitosan with ENR50 in acidified 1,4-dioxane

ENR50 (1.0 g) was dissolved in a dual-solvent consisting of water and 1,4-dioxane (2.5:97.5% v/v) inside a 250 mL two-necked round bottom flask equipped with a magnetic stirrer and a reflux condenser. Then CTS (1.0 g) and $AlCl_3·6H_2O$ (0.75 g) were added and the content of the flask was refluxed with continuous stirring for 6 hours. Subsequently, the resulting mixture was cooled and filtered. The filtrate containing the product was concentrated under reduced pressure using a rotary evaporator and cast on a glass plate. The product (CTS-g-ENR-P1) was dried in an oven (50°C) for 24 hours.

The experiment was repeated with the use of a lower concentration (i.e. 0.30 g) of $AlCl_3·6H_2O$. The product obtained is designated as CTS-g-ENR-P2. For the purpose of obtaining a reference sample (ENR50-control), ENR50 was subjected to similar reaction condition with the use of 0.75 g of $AlCl_3·6H_2O$ but in the absence of CTS. All resulting polymeric materials were characterized by means of FT-NMR, FT-IR, SEM, DSC and TGA techniques.

4. Results and discussion

4.1. Effect of acidity on the stability of the molecular structure of ENR50

^{1}H-NMR spectra of ENR50 and ENR50 derivatives that were obtained after ENR50 been exposed to 0.0001, 0.001, 1.0 and 3.0 M of HCl for 1 hour are depicted in Figure 1. The epoxy group of an epoxidized natural rubber is known to be randomly distributed on the backbone of the polymer. Nonetheless, a fairly comprehensive characterization of the structure of liquid epoxidized natural rubber by means of 1D-NMR and 2D-NMR spectroscopy is available in the literature [29]. For simplicity, the proton resonances of ENR50 as observed in Figure 1 are assigned to a simplified structure depicted in Figure 2 as follows: methyl protons bonded to the epoxidized isoprene unit **a** ($–CH_2–C\mathbf{H_3}COCH–CH_2–$) = 1.29 ppm; methylene protons bonded to the epoxidized isoprene unit **b** ($–C\mathbf{H_2}–CH_3COCH–CH_2–$) = 1.55 ppm, methyl protons bonded to the isoprene unit **c**

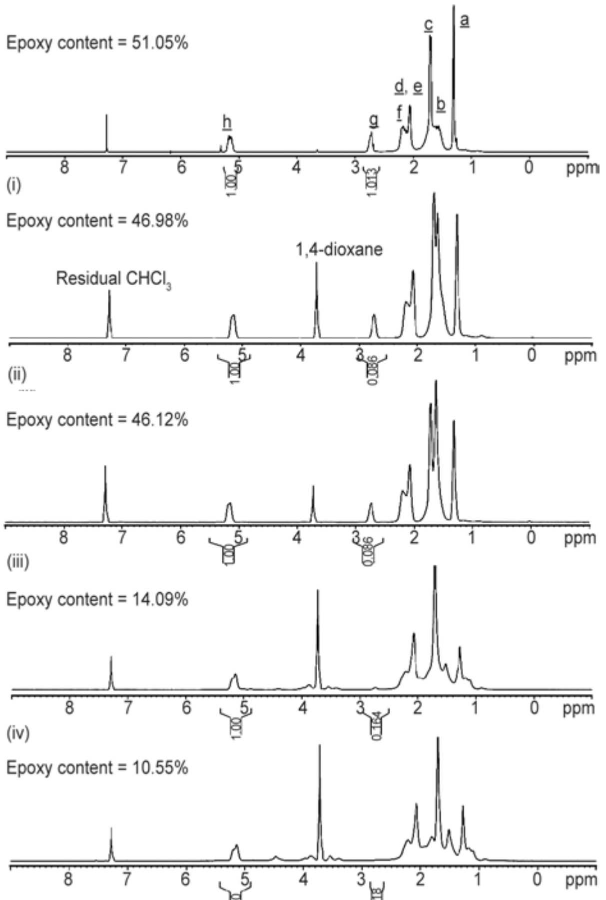

Figure 1. ^{1}H-NMR spectra of (i) ENR50 and its derivatives obtained after ENR50 has been exposed (ii) 0.0001 M, (iii) 0.001 M, (iv) 1.0 M and (v) 3.0 M of HCl for 1 hour

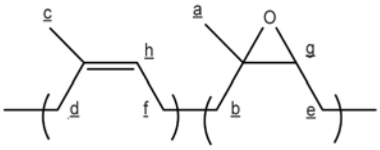

Figure 2. A simplified structure of ENR50

(–CH_2–C**H_3**C=CH–CH_2–) = 1.67 ppm, methylene protons bonded to the isoprene unit **d** (–C**H_2**–CH_3 COCH–CH_2–) overlapped with the methylene protons bonded to the epoxidized isoprene unit **e** (–CH_2–CH_3COCH–C**H_2**–) = 2.04 ppm; methylene protons bonded to the isoprene unit **f** (–CH_2–CH_3 COCH–C**H_2**–) = 2.15 ppm; methine proton bonded to the epoxidized isoprene unit **g** (–CH_2–CH_3COC**H**–CH_2–) = 2.70 ppm; methine proton bonded to the isoprene unit **h** (–CH_2–CH_3C=C**H**–CH_2–) = 5.10 ppm. The presence of residual amount of 1,4-dioxane and chloroform can be observed at 7.16 and 3.70 ppm. The epoxy content [30] can be determined with the use of Equation (1):

$$\text{Epoxy content} = \frac{A_{2.7}}{A_{2.7} + A_{5.1}} \cdot 100\% \qquad (1)$$

where $A_{2.7}$ and $A_{5.1}$ refer to the integral area of **g** = 2.7 and **h** = 5.1, respectively. From Figure 1(i), the actual epoxy content of ENR50 is determined to be 51.05% whereas that of the ENR50 derivatives (Figure 1(ii)–1(v)) obtained after ENR50 having been exposed to 0.0001, 0.001, 1.0 and 3.0 M HCl is 46.98, 46.12, 14.09 and 10.55%, respectively. The effect of acidity on the stability of the molecular structure of ENR50 becomes clear when we consider the degree of reduction of its epoxy content. The difference in epoxy content of ENR50 and that of the ENR50 derivative obtained after having been exposed to 1.0 and 3.0 M HCl is 36.96 and 40.50%, respectively. However, when in 0.0001 and 0.001 M the difference is only 4.07 and 4.93%, respectively. This means the molecular structure of ENR50 remained fairly intact at low acid concentration ($[H^+] \leq 0.001$ M) even though its epoxidized isoprene units were likely to be fully protonated and susceptible to undergo ring-opening reaction with nucleophiles.

4.2. Effect of $AlCl_3·6H_2O$ on the epoxidized isoprene unit of ENR50

A solution containing $AlCl_3·6H_2O$ is mildly acidic (pH = 4.5) due to the formation of hydronium ion as illustrated by the Brønsted-Lowry acid-base reaction in Figure 3. When $AlCl_3·6H_2O$ dissolved in water, the aluminium ion will be surrounded with six water molecules. The Al^{3+} aqua complex ion, $[Al(H_2O)]^{3+}$, is a weak Brønsted-Lowry acid that donates a proton, H^+, forming the Al^{2+} aqua complex ion, $[Al(H_2O)_5OH]^{2+}$, whereas the water molecule acts as a weak Brønsted-Lowry base that accepts the proton forming the hydronium ion, H_3O^+.

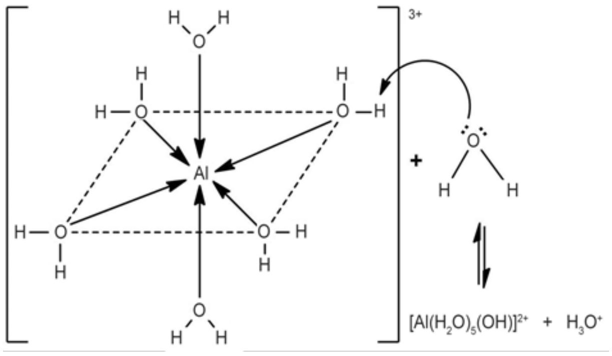

Figure 3. Acid hydrolysis of aluminium ion

^{1}H-NMR spectra of ENR50 derivatives that were obtained after ENR50 having been exposed to $AlCl_3·6H_2O$ for 2, 4 and 24 hours are depicted in Figure 4. Their corresponding epoxy content is determined to be 44.93, 44.04 and 38.84%, respectively. In keeping with the above finding wherein diluted HCl was used, the epoxidized isoprene units of

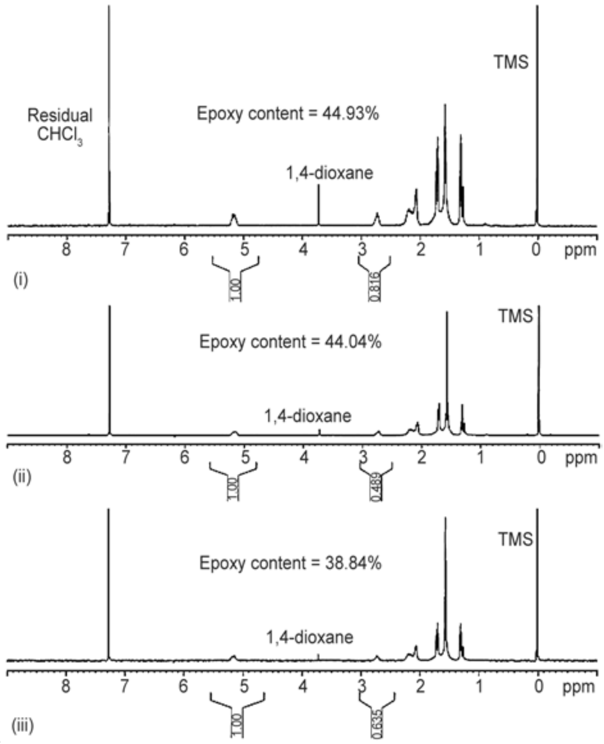

Figure 4. ^{1}H-NMR spectra of ENR50 derivatives obtained after ENR50 has been exposed to $AlCl_3·6H_2O$ for (i) 2 hr, (ii) 4 hr and (iii) 24 hr

ENR50 did not undergo significant ring-opening reaction even though being likely fully protanated in a solution containing $AlCl_3·6H_2O$.

4.3. Nuclear magnetic resonance spectral analysis

Figure 5 depicts the fourier transformed ^{1}H-NMR spectra of ENR50-control and CTS-g-ENR-P1. The epoxy content of ENR50-control and CTS-g-ENR-P1 is determined to be 44.93 and 22.36%, respectively. It is therefore evident that ENR50 underwent a substantial reduction in epoxy content only in the presence of CTS. As such, it is reasonable to deduce that the grafting of CTS onto the backbone ENR50 had likely occurred via ring-opening reaction of protonated epoxidized isoprene units. The plausible reaction pathways leading to the formation of CTS-g-ENR biopolymers is discussed later in the text.

4.4. Infrared spectral analysis

Figure 6 shows the Fourier transform infrared spectra of ENR50, CTS and CTS-g-ENR-P1. The characteristic vibrational absorption bands of ENR50: 2961, 2923 and 2856 cm^{-1} are due to C–H stretchings of the $–CH_3–$ and $–CH_2–$ groups, 1660 cm^{-1} is due the C=C stretching, 1448 and 1376 cm^{-1} are due to C–H bendings of the $–CH_2–$ and $–CH_3–$ groups, 1259 and 1018 cm^{-1} are due to C–O–C stretching and bending of the epoxy group, 873 cm^{-1} is due to C–H bending attached to the epoxy group and 837 cm^{-1} is due to C–H bending attached to the unsaturated carbon [31]. The characteristic bands of CTS: broad band at 3600–3100 cm^{-1} are due to a combination of O–H and N–H stretchings of the hydroxyl and primary amine groups, 2956 cm^{-1} is due to the C–H stretching of the $–CH_2–$ group, 1638 and 1560 cm^{-1} (overlapped) are due to the N–H bendings of the amide and primary amine groups, broad band at 1080–1033 cm^{-1} is due the skeletal vibration involving C–O stretching, 896 cm^{-1} is due the stretching of C–O–C linkage [32]. For CTS-g-ENR-P1 (Figure 6(iii)), the normally broad band due to the absorption of hydroxyl and amino groups became narrower and shifted to a lower frequency, centered at about 3322 cm^{-1}, indicating that chemical reaction had taken place predominantly at the primary amine rather than at the hydroxyl groups. The considerable reduction of the intensity of the band at 873 cm^{-1} suggests that the epoxy group was involved in the reaction. The presence of the characteristic absorption band at 1645 cm^{-1} due to the N–H bending suggests that the primary amine group of chitosan was involved in the reaction. Furthermore, the appearance of additional bands at 733, 902 and 1219 cm^{-1} assignable to N–H wag, C–N bond and saccharide structure of chitosan, respectively [33], affirms that CTS-g-ENR-P1 was produced likely via the acid-induced attack of the primary amine of the former on the epoxide ring of the latter.

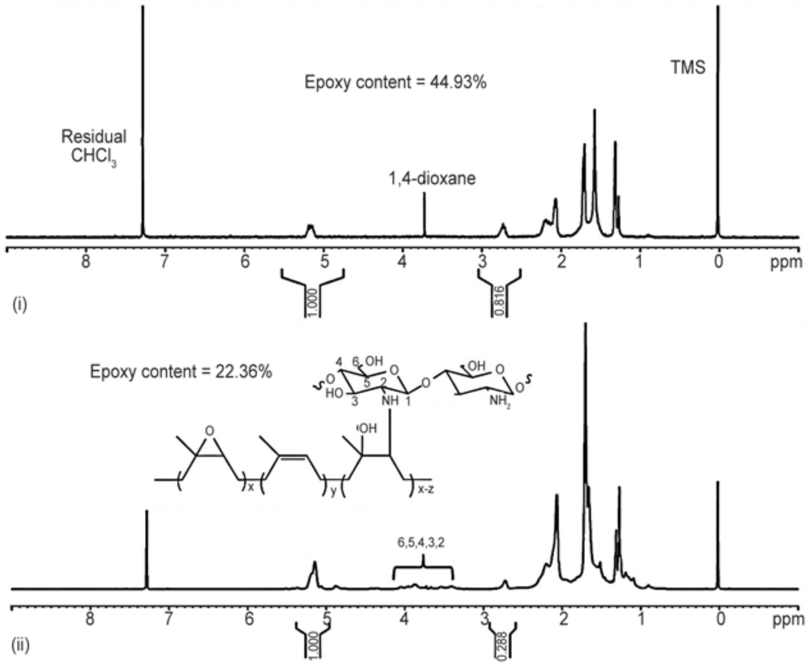

Figure 5. ^{1}H-NMR spectra of (i) ENR50-control and (ii) CTS-g-ENR-P1

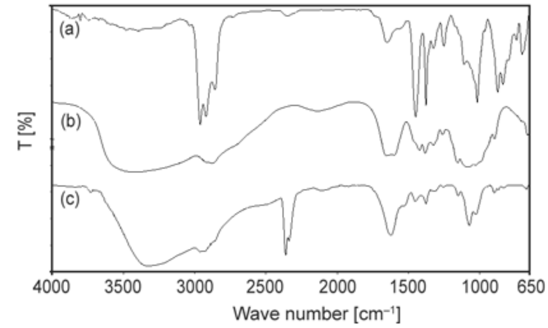

Figure 6. FTIR spectra of (i) ENR50, (ii) CTS and (iii) CTS-g-ENR-P1

4.5. Differential scanning calorimetric analysis

The thermograms (DSC second run curves) of CTS/ENR50-control, CTS-g-ENR-P1 and CTS-g-ENR-P2 are illustrated in Figure 7. Two cycles of heating and cooling runs were carried out in order to eliminate the moisture effect, and the temperature region was taken into consideration to avoid thermal degradation in the first heating. The T_g of CTS/ENR50-control, sample prepared by physically mixing appropriate amounts of CTS and ENR50, was found to be –27.24°C. This T_g is very close to that of ENR50 (–23.90°C), indicating no reaction took place under this condition. The T_g of CTS is not observed in Figure 7 because it occurred at a higher temperature, 203°C [34], i.e., outside the temperature range indicated. The T_g of CTS-g-ENR-P2, the biocomposite obtained with the use of a lower concentration of $AlCl_3{\cdot}6H_2O$, is 2.88°C. The fact that only one T_g was detected for CTS-g-ENR-P2 exemplify a new product that had formed arising from the grafting of CTS onto the backbone ENR50. The T_g of CTS-g-ENR-P1, the biocomposite obtained with the use of a higher concentration of $AlCl_3{\cdot}6H_2O$, is also not observed in Figure 7 because it is closer to that of CTS which occurred outside the temperature range indicated.

4.6. Thermogravimetric analysis

The thermogravimetric (TGA) and derivative thermogravimetric (DTG) curves of ENR50, CTS, CTS-g-ENR-P1 and CTS-g-ENR-P2 are depicted in Figure 8 and Figure 9, respectively. The DTG curve of ENR50 exhibits one-step degradation process with rapid weight loss of 48% at 418°C. The major mass loss occurred within 310 and 570°C is 96% due to the total pyrolysis (decomposition of the hydrocarbon in nitrogen atmosphere) of the rubber matrices. The amount of carbonized residue deduced from the TGA curve of ENR50 beyond 600°C is about 2.5%. DTG curve of CTS exhibits mass loss at two stages. The initial mass loss of 12% occurred within 40 and 240°C due to loss of solvent molecules (water and acetic acid). The second stage shows a mass loss of 52% within 240 and 400°C due to degradation (via chain scission) of CTS [35]. The amount of carbonized residue deduced from the TGA curve of CTS beyond 600°C is about 33.8% which is quite substantial compared to that of ENR50. However, from the view point of thermal stability it is of interest to note that within 270 and 340°C only about 1% of ENR50 degraded whereas CTS degraded by about 38%. Therefore, ENR50 is thermally more stable than CTS.

Both DTG curves of CTS-g-ENR-P1 and CTS-g-ENR-P2 show approximately similar three degradation stages. The first mass loss of 3% occurred within 40 and 150°C attributable to solvent molecules (water and 1,4-dioxane) imbedded in the biopolymers. The second mass loss of 15% occurred within 140 and 300°C due to the destruction of amino

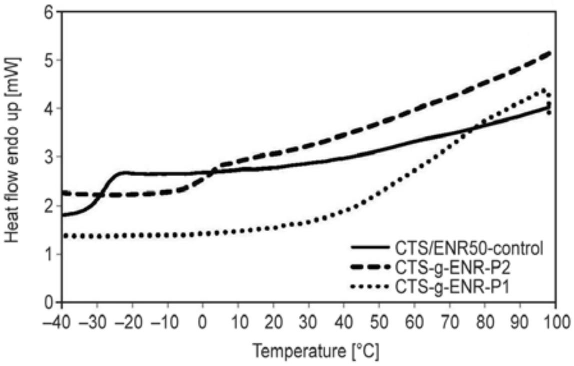

Figure 7. DSC curves of the CTS/ENR50-control, CTS-g-ENR-P1 and CTS-g-ENR-P2

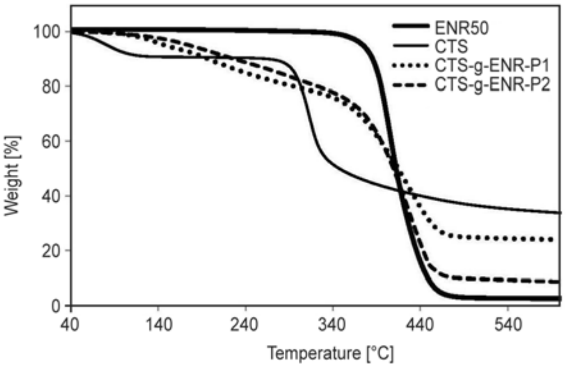

Figure 8. TGA curves for ENR50, CTS, CTS-g-ENR-P1 and CTS-g-ENR-P2

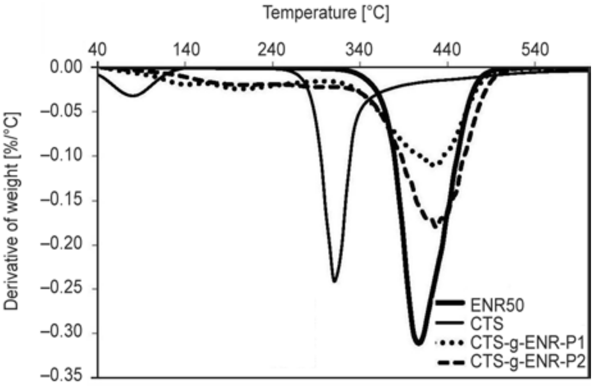

Figure 9. DTG curves for ENR50, CTS, CTS-g-ENR50-P1 and CTS-g-ENR50-P2

groups of CTS [9]. The third is the major mass loss of 56% occurred within 300 and 594°C due to a combination of chain scission of the grafted CTS and total decomposition of the rubber matrices. The amount of carbonized residue deduced from the TGA curves of CTS-g-ENR-P1 and CTS-g-ENR-P2 beyond 600°C is 24 and 9%, respectively. Therefore, it is apparent that lesser amount of CTS incorporated (grafted) onto the rubber matrices resulted in a lower amount of carbonized residue beyond 600°C. The thermal stabilities of CTS-g-ENR-P1 and CTS-g-ENR-P2 are quite similar and likely due to a combination of that of CTS and ENR50, i.e., higher than that of CTS but lower than that of ENR50.

4.7. Morphology study

SEM micrographs of CTS, ENR50 and CTS-g-ENR-P1 are shown in Figure 10. The chitosan has a flaky and uneven shape with smooth surface but the ENR50 displays a rough and groove like structure with some debris. Micrographs of the biocomposite show a one-phase morphology with a reduced gap between the chitosan and the rubber matrices suggesting not only good interfacial interactions but also very likely that CTS has been successfully grafted onto the backbone of the ENR.

4.8. Reaction pathways for the formation of CTS-g-ENR biopolymers

The plausible reaction pathways for the formation of CTS-g-ENR biopolymers are proposed in Figure 11. In a mildly acidic condition such as in solution containing $AlCl_3{\cdot}6H_2O$ (pH = 4.5), the epoxidized isoprene units of ENR50 would likely be protonated and susceptible to attack by reactive nucleophiles. How-

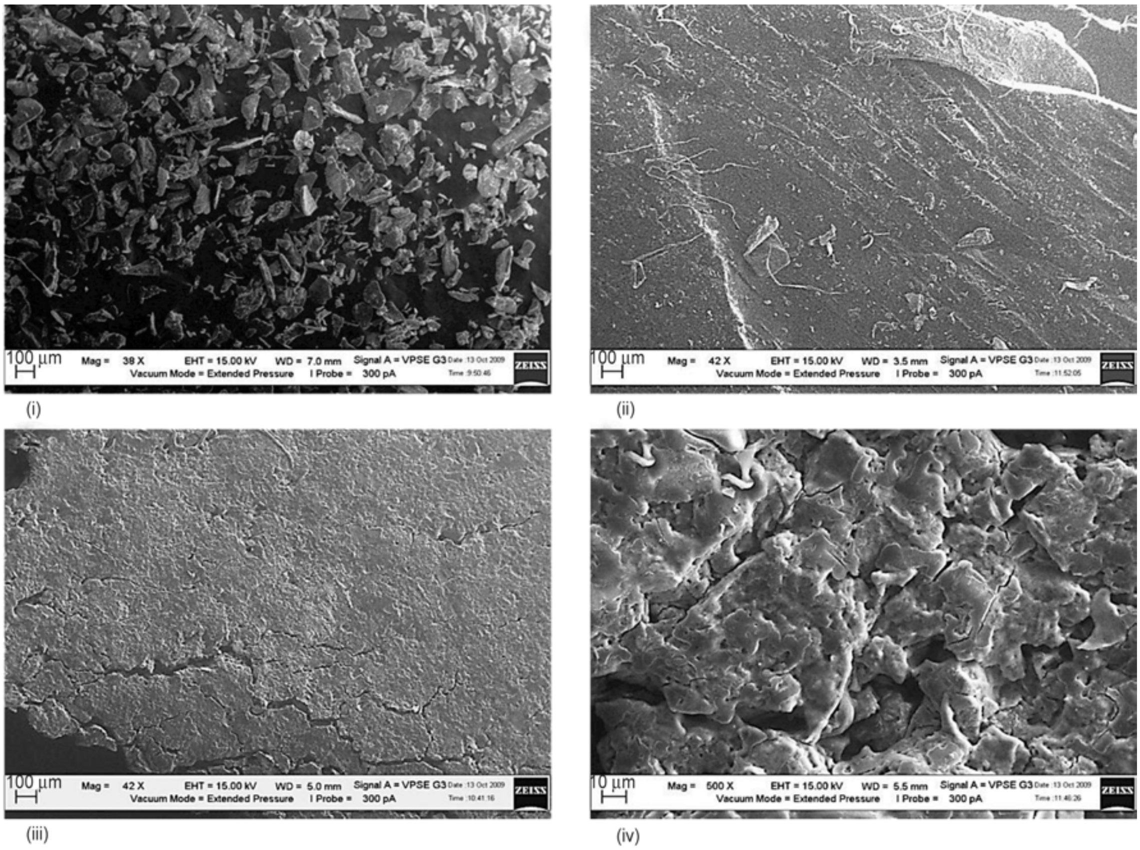

Figure 10. SEM micrographs of (i) CTS, (ii) ENR50, (iii) CTS-g-ENR-P1 at magnification of 42×, (iv) CTS-g-ENR-P1 biopolymers at magnification of 500×

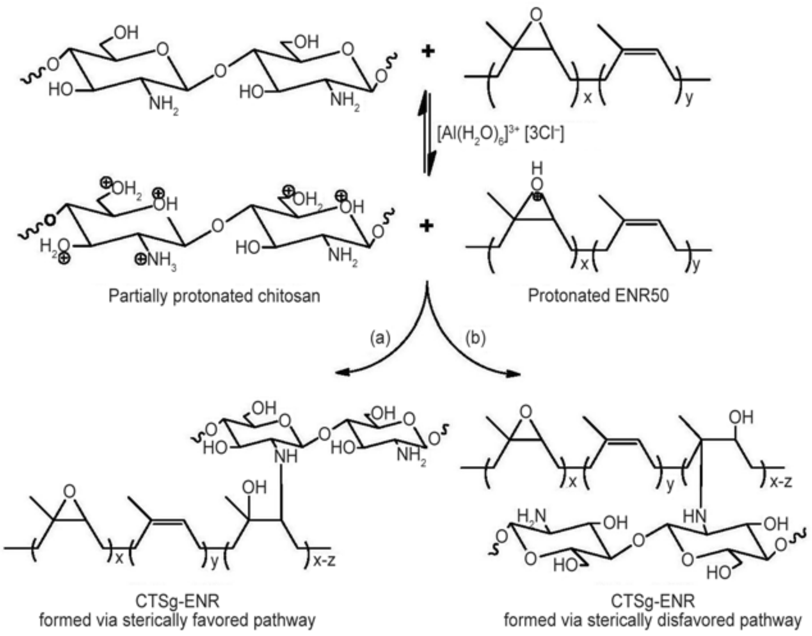

Figure 11. Reaction pathways for the formation of CTS-g-ENR biopolymers

ever under the similar mildly acidic condition, CTS being a multinucleophilic material would be partially protonated. The unhindered primary (C-6) hydroxyl group of CTS would be protonated rendering it non-reactive, whereas some of the sterically hindered primary amino (C-2) and secondary (C-3) hydroxyl groups would be free, i.e., remain as reactive nucleophiles. A primary amino group is much more reactive than a secondary hydroxyl group. As such, the grafting of CTS onto the backbone of ENR50 would involve solely the attack of the primary amino (C-2) of CTS on the protonated epoxidized isoprene units of ENR50. The attack may occur via sterically favored pathway (a) and sterically disfavored pathway (b) as illustrated in Figure 11. However, considering that CTS is a bulky polymeric entity and the fact that ENR50 remained structurally stable in the mildly acidic condition, we are of the opinion that the acid-induced reaction of ENR50 with CTS occurred preferentially or regioselectively via the sterically favored pathway. This notion is further supported by the infrared spectral analysis described above.

5. Conclusions

The effect of acidity on the stability of the molecular structure of ENR50 was investigated. It is hitherto elucidated by means of NMR spectroscopy that ENR50 remained structurally stable in 1,4-dioxane acidified by the addition of dilute HCl or $AlCl_3 \cdot 6H_2O$ solution. Based on this finding, the acid-induced reaction of ENR50 with CTS in a dual-solvent consisting of 1,4-dioxane and water (97.5:2.5% v/v) was explored. Two type of biopolymers CTS-g-ENR-P1 and CTS-g-ENR-P2 consisting of higher and lower amount CTS, respectively, grafted onto the backbone on the natural rubber derivative were prepared. The structural and physicochemical properties of the products as compared to that of the starting materials were characterized by means of FT-NMR, FT-IR, SEM, DSC and TGA techniques. The regioselectivity of the acid-induced reaction is discussed and it is concluded that the biopolymers were formed via sterically favored pathway involving the attack of the primary amino (C-2) of CTS on the protonated epoxidized isoprene units of ENR50.

Acknowledgements

The authors would like to thank the Malaysian Government and Universiti Sains Malaysia for providing the financial support via the Fundamental Research Grant Scheme (FRGS) No. 1001/PKIMIA/842021. They would like to also extend their deepest gratitude to Dr Kartini Noorsal from Advanced Materials Research Centre (AMREC), Kulim for her assistance in providing the SEM facilities.

References

[1] Muzzarelli R.: Chitin. Pergamon Press, Oxford (1977).
[2] Chandra R., Rustgi R.: Biodegradable polymers. Progress in Polymer Science, **23**, 1273–1335 (1998). DOI: 10.1016/S0079-6700(97)00039-7

[3] Auzély R., Rinaudo M.: Controlled chemical modifications of chitosan. Characterization and investigation of original properties. Macromolecular Bioscience, **3**, 562–565 (2003).
DOI: 10.1002/mabi.200300018

[4] Dutta P., Dutta J., Tripathi V.: Chitin and chitosan: Chemistry, property and application. Journal of Scientific and Industrial Research, **63**, 20–31 (2004).

[5] Munro N. H., Hanton L. R., Moratti S. C., Robinson B. H.: Preparation and graft copolymerisation of thiolated β-chitin and chitosan derivatives. Carbohydrate Polymers, **78**, 137–145 (2009).
DOI: 10.1016/j.carbpol.2009.04.018

[6] Muzzarelli R. A. A., Muzzarelli C.: Chitosan chemistry: Relevance to the biomedical sciences. in 'Polysaccharides I' (ed.: Heinze T.) Springer, Berlin, 151–209 (2005).
DOI: 10.1007/b136820

[7] Rogovina S. Z., Alexanyan C. V., Prut E. V.: Biodegradable blends based on chitin and chitosan: Production, structure, and properties. Journal of Applied Polymer Science, **121**, 1850–1859 (2011).
DOI: 10.1002/app.33477

[8] Johns J., Rao V.: Characterization of natural rubber latex/chitosan blends. Journal of Polymer Analysis and Characterization, **13**, 280–291 (2008).
DOI: 10.1080/10236660802190104

[9] Rao V., Johns J.: Mechanical properties of thermoplastic elastomeric blends of chitosan and natural rubber latex. Journal of Applied Polymer Science, **107**, 2217–2223 (2008).
DOI: 10.1002/app.27265

[10] Rao V., Johns J.: Thermal behavior of chitosan/natural rubber latex blends TG and DSC analysis. Journal of Thermal Analysis and Calorimetry, **92**, 801–806 (2008).
DOI: 10.1007/s10973-007-8854-5

[11] Johns J., Rao V.: Mechanical properties and swelling behavior of cross-linked natural rubber/chitosan blends. International Journal of Polymer Analysis and Characterization, **14**, 508–526 (2009).
DOI: 10.1080/10236660903072797

[12] Johns J., Rao V.: Thermal stability, morphology, and X-ray diffraction studies of dynamically vulcanized natural rubber/chitosan blends. Journal of Materials Science, **44**, 4087–4097 (2009).
DOI: 10.1007/s10853-009-3589-2

[13] Letwattanaseri T., Ichikawa N., Mizoguchi T., Tanaka Y., Chirachanchai S.: Epoxidized natural rubber bionanocomposite: A model case of bionanocomposite using nanofibrous chitosan and its consequent functional properties. Chemistry Letters, **38**, 798–799 (2009).
DOI: 10.1246/cl.2009.798

[14] Shaari S., Ismail H., Othman N.: The effect of chitosan loading on the properties of chitosan filled epoxidized natural rubber compounds. Key Engineering Materials, **471–472**, 851–856 (2011).
DOI: 10.4028/www.scientific.net/KEM.471-472.851

[15] Ismail H., Shaari S. M., Othman N.: The effect of chitosan loading on the curing characteristics, mechanical and morphological properties of chitosan-filled natural rubber (NR), epoxidised natural rubber (ENR) and styrene-butadiene rubber (SBR) compounds. Polymer Testing, **30**, 784–790 (2011).
DOI: 10.1016/j.polymertesting.2011.07.003

[16] Riyajan S-A., Sukhlaaied W.: Effect of chitosan content on gel content of epoxized natural rubber grafted with chitosan in latex form. Materials Science and Engineering: C, **33**, 1041–1047 (2013).
DOI: 10.1016/j.msec.2012.11.012

[17] Ravi Kumar M. N.: A review of chitin and chitosan applications. Reactive and Functional Polymers, **46**, 1–27 (2000).
DOI: 10.1016/S1381-5148(00)00038-9

[18] Aranaz I., Mengibar M., Harris R., Panos I., Miralles B., Acosta N., Heras A.: Functional characterization of chitin and chitosan. Current Chemical Biology, **3**, 203–230 (2009).
DOI: 10.2174/187231309788166415

[19] Gelling I., Tinker A., Rahman H. B.: Solubility parameters of epoxidised natural rubber. Journal of Natural Rubber Research, **6**, 20–29 (1991).

[20] Gelling I.: Epoxidised natural rubber. Journal Rubber Research, **6**, 184–205 (1991).

[21] Derouet D., Brosse J-C., Challioui A.: Alcoholysis of epoxidized polyisoprenes by direct opening of oxirane rings with alcohol derivatives 1. Modelization of the reaction. European Polymer Journal, **37**, 1315–1326 (2001).
DOI: 10.1016/S0014-3057(00)00266-4

[22] Derouet D., Brosse J-C., Challioui A.: Alcoholysis of epoxidized polyisoprenes by direct opening of oxirane rings with alcohol derivatives 2. Study on epoxidized 1,4-polyisoprene. European Polymer Journal, **37**, 1327–1337 (2001).
DOI: 10.1016/S0014-3057(00)00267-6

[23] Gan S-N., Abdul Hamid Z.: Partial conversion of epoxide groups to diols in epoxidized natural rubber. Polymer, **38**, 1953–1956 (1997).
DOI: 10.1016/S0032-3861(96)00710-0

[24] Derouet D., Brosse J., Tillekeratne L.: Fixation of methacrylic acid onto epoxidised liquid natural rubber. Journal of Natural Rubber Research, **5**, 296–300 (1990).

[25] Jayawardena S., Rexy D., Durand D., Pinazzi C. P.: Synthesis of macromolecular antioxidants by reaction of aromatic amines with epoxidized polyisoprene, 3. Reaction of 4-anilinoaniline with epoxidized 1,4-polyisoprene. Die Makromolekulare Chemie, **185**, 2089–2097 (1984).
DOI: 10.1002/macp.1984.021851004

[26] Siti Maznah K., Baharin A., Hanafi I., Azhar M. E., Mas Rosemal Hakim M. H.: Effect of soaking in potassium hydroxide solution on the curing, tensile properties and extractable protein content of natural rubber latex films. Polymer Testing, **27**, 1013–1016 (2008).
DOI: 10.1016/j.polymertesting.2008.09.005

[27] Siti Maznah K., Baharin A., Hanafi I., Azhar M. E., Rosemal Hakim M. H.: Effect of acid treatment on extractable protein content, crosslink density and tensile properties of natural rubber latex films. Polymer Testing, **27**, 823–826 (2008).
DOI: 10.1016/j.polymertesting.2008.06.004

[28] Lu S., Song X., Cao D., Chen Y., Yao K.: Preparation of water-soluble chitosan. Journal of Applied Polymer Science, **91**, 3497–3503 (2004).
DOI: 10.1002/app.13537

[29] Saito T., Klinklai W., Kawahara S.: Characterization of epoxidized natural rubber by 2D NMR spectroscopy. Polymer, **48**, 750–757 (2007).
DOI: 10.1016/j.polymer.2006.12.001

[30] Malz F., Jancke H.: Validation of quantitative NMR. Journal of Pharmaceutical and Biomedical Analysis, **38**, 813–823 (2005).
DOI: 10.1016/j.jpba.2005.01.043

[31] Mahmood W. A. K., Khan M. M. R., Azarian M. H.: Sol-gel synthesis and morphology, thermal and optical properties of epoxidized natural rubber/zirconia hybrid films. Journal of Non-Crystalline Solids, **378**, 152–157 (2013).
DOI: 10.1016/j.jnoncrysol.2013.07.002

[32] Duan K., Chen H., Huang J., Yu J., Liu S., Wang D., Li Y.: One-step synthesis of amino-reserved chitosan-*graft*-polycaprolactone as a promising substance of biomaterial. Carbohydrate Polymer, **80**, 498–503 (2010).
DOI: 10.1016/j.carbpol.2009.12.013

[33] Ng L-T., Swami S.: IPNs based on chitosan with NVP and NVP/HEMA synthesised through photoinitiator-free photopolymerisation technique for biomedical applications. Carbohydrate Polymers, **60**, 523–528 (2005).
DOI: 10.1016/j.carbpol.2005.03.009

[34] Sakurai K., Maegawa T., Takahashi T.: Glass transition temperature of chitosan and miscibility of chitosan/poly (*N*-vinyl pyrrolidone) blends. Polymer, **41**, 7051–7056 (2000).
DOI: 10.1016/S0032-3861(00)00067-7

[35] Pawlak A., Mucha M.: Thermogravimetric and FTIR studies of chitosan blends. Thermochimia Acta, **396**, 153–166 (2003).
DOI: 10.1016/S0040-6031(02)00523-3

eXPRESS Polymer Letters Vol.8, No.2 (2014) 95–106
Available online at www.expresspolymlett.com
DOI: 10.3144/expresspolymlett.2014.12

Curing kinetics, mechanism and chemorheological behavior of methanol etherified amino/novolac epoxy systems

S. F. Zhao[1], *G. P. Zhang*[1*], *R. Sun*[1], *C. P. Wong*[2]

[1]Shenzhen Institutes of Advanced Technology, Chinese Academy of Sciences, Shenzhen, China
[2]Department of Electronic Engineering, Faculty of Engineering, The Chinese University of Hong Kong, Hong Kong, China

Received 4 August 2013; accepted in revised form 29 September 2013

Abstract. The curing kinetics and mechanism of epoxy novolac resin (DEN) and modified epoxy novolac resin (MDEN) with methanol etherified amino resin were studied by means of differential scanning calorimetry (DSC), Fourier transform-infrared (FT-IR) spectroscopy and chemorheological analysis. Their kinetics parameters and models of the curing were examined utilizing isoconversional methods, Flynn-Wall-Ozawa and Friedman methods. For the DEN mixture, its average activation energy (E_a) was 71.05 kJ/mol and the autocatalytic model was established to describe the curing reaction. The MDEN mixture exhibited three dominant curing processes, termed as reaction 1, reaction 2 and reaction 3; and their E_a were 70.05, 106.55 and 101.91 kJ/mol, respectively. Besides, E_a of reaction 1 was similar to that of DEN mixture, while E_a of reactions 2 and 3 corresponded to that of the etherification reaction between hydroxyl and epoxide group. Moreover, these three dominant reactions were nth order in nature. Furthermore, their curing mechanisms were proposed from the results of DSC and FTIR. The chemorheological behavior was also investigated to obtain better plastics products via optimizing the processing schedules.

Keywords: *rheology, autocatalytic kinetic model, curing mechanism, activation energy*

1. Introduction

Epoxy resins have been widely applied in many areas such as aerospace and electronics industries in the form of surface coatings, structural adhesives, advanced composites and packaging materials due to their well-balanced properties. For example, epoxy resins possess excellent thermal stability, moisture resistance, chemical stability, superior electrical and mechanical properties and good adhesion to many substrates [1–3]. As well as known properties, such as, the superior mechanical and chemical properties of epoxy polymers are profited from the complicated curing processes, in which a low molecular weight oligomer is transformed into an infinite molecular weight polymer forming a three-dimensional network structure. Therefore, elucidation of the reaction mechanism of epoxy curing still attracts great interest for both fundamental and applied chemistry areas. Meanwhile, in the curing reaction of epoxy resins, amino resins are widely used as hardeners but the curing mechanism is still not completely revealed [4–6]. Yong Lv *et al.* [7] studied the curing kinetics of a diglycidyl ether of bisphenol A with a methanol etherified amino resin, but they did not discuss the origin of proton, which is important to methanol etherified amino resin. Besides, the curing process is related to the rheological behavior. The viscosity of curing system varies not only with temperature and flow conditions but also with reaction time. Therefore, in order to optimize the properties of the cured product, it is important to understand the relationship between the curing kinetics and rheological behavior of the entire epoxy system.

---

[*]Corresponding author, e-mail: gp.zhang@siat.ac.cn

Many efforts have been done to determine the appropriate models to describe the curing kinetics distinctly [8–12]. Because of the complex nature of thermosetting reactions, phenomenological models are the most popular for these systems. The simplest models are those based on n^{th} order kinetics. Another widely used model is the autocatalytic expression. Regarding rheological behavior, an advance was made from the correlation between viscosity and temperature that include kinetics and/or structure information [13, 14]. However, there are few studies to investigate the kinetic model from chemorheological behavior.

In our previous work, novolac epoxy resin of DEN 431 (abbreviated as DEN) was modified by p-hydroxybenzoic acid (PHBA). The modified novolac epoxy resin (MDEN) was cured with amino resin to prepare cured composites with superior thermal, mechanical and dielectric properties [15]. In this work, the curing kinetics, curing mechanism and chemorheological behavior of DEN/amino resin and MDEN/amino resin systems were further investigated to discuss their differences. The curing kinetics of the studied systems was examined by dynamic differential scanning calorimetry (DSC) at different heating rates, and the curing mechanism was proposed by the aid of the results of DSC and Fourier transform-infrared (FT-IR) spectra. Simultaneously, the chemorheological behavior was further investigated to optimize the process schedule.

2. Experimental

2.1. Materials

Novolac epoxy resin of DEN 431 with epoxy equivalent weight of 177–200 g/mol (Dow Chemical Company, Russellville, Arkansas, USA), methyl etherified amino resin of Cymel 303 (HMMM) (Cytec Industry, Penfield, NY, USA) and 2-ethyl-4-methylimidazole (EMI-24) (Shanghai Chemical Reagent Factory, Shanghai, China) were used as received without further purifications. Modified DEN (MDEN) was prepared according to our previous study [15]. These chemical structures were presented in Figure 1.

2.2. Characterization

The FT-IR spectra were recorded on a Bruker Vertex 70 spectrometer (Bruker Optik GmbH, Ettlingen, Germany) in the range of 4000–400 cm^{-1}. The curing kinetics analysis was conducted by a TA Q20-1173 DSC thermal system (TA instruments, New Castle, USA) with heating rates of 2.5, 5, 10, and 15°C/min, respectively, and ranging from 50 to 300°C. Nitrogen gas was purged at a flow rate of about 50 mL/min.

The chemorheological behavior was measured using an Anton Paar MCR302 rheometer (Anton Paar GmbH, Graz, Austria) with a heating rate of 2.5°C/min and ranging from 40 to 280°C.

2.3. Theoretical calculations

The heat flow measured in DSC is proportional to both the overall heat release and the curing rate, as shown by Equation (1) [16]:

$$\frac{\mathrm{d}Q}{\mathrm{d}t} = Q_{\text{thr}}\frac{\mathrm{d}a}{\mathrm{d}t} = Q_{\text{thr}}k(T)f(a) \tag{1}$$

where $\mathrm{d}Q/\mathrm{d}t$ is the heat flow, Q_{thr} is the total heat released when an uncured material is brought to complete cure, $\mathrm{d}a/\mathrm{d}t$ is the curing rate, a is the extent of reaction, $k(T)$ is the rate constant, T is the temperature, and $f(a)$ is the reaction model. For epoxy curing, $f(a)$ is usually taken in the form of $(1-a)^{\mathrm{n}}$ (n^{th}-order reaction) or of $a^{\mathrm{m}}(1-a)^{\mathrm{n}}$ (autocatalytic reaction). The explicit temperature dependence of the rate constant is introduced by replacing $k(T)$ with the Arrhenius equation (Equation (2)):

$$\frac{\mathrm{d}a}{\mathrm{d}t} = A\exp\left(-\frac{E}{RT}\right)f(a) \tag{2}$$

where A is the pre-exponential factor, E is the activation energy, and R is the gas constant. When a sample is heated at a constant rate, the explicit temporal dependence in Equation (2) is eliminated through the transformation shown by Equation (3):

$$\frac{\mathrm{d}a}{\mathrm{d}T} = \frac{A}{\beta}\exp\left(-\frac{E}{RT}\right)f(a) \tag{3}$$

where $\beta = \mathrm{d}T/\mathrm{d}t$ is the heating rate. Kinetics analysis of a nonisothermal resin-cured system can be performed by the multiple β. Two different isoconversional methods employed in this study were as follows, and the advantage of the two kinetics methods is that they do not assume a particular form of the reaction model.

2.3.1. Flynn-Wall-Ozama method

The isoconversional integral method was also proposed independently by Flynn, Wall and Ozawa using Doyle's approximation of the temperature integral [17, 18]. This method is based on Equations (4) and (5):

$$\ln\beta = \ln\left(A\frac{E_a}{R}\right) - \ln g(a) - 5.331 - 1.052\left(\frac{E_a}{RT}\right) \tag{4}$$

$$g(a) = \int_0^a \frac{\mathrm{d}a}{f(a)} \tag{5}$$

where $g(a)$ is the integral conversion function.

This method has been used in present computations of the activation energy at different values of conversion. Thus, for a constant a, the plot of ($\ln\beta$) vs. ($1/T$) obtained from DSC thermograms using various heating rates, should render a straight line where the slope allows the determination of the apparent activation energy. The experimentally evaluated values of the activation energy were used to determine the appropriate kinetic model which best described the conversion function of the process studied.

2.3.2. Friedman method

The Friedman method is also used to determine a kinetic model of the curing process [19]. The method is based on Equation (6):

$$\ln\frac{\mathrm{d}a}{\mathrm{d}t} = \ln\beta\frac{\mathrm{d}a}{\mathrm{d}T} = \ln[Af(a)] - \frac{E_a}{RT} \tag{6}$$

In case of the nth-order reaction, Equation (6) was transformed into Equation (7):

$$\ln[Af(a)] = \ln\left[\frac{\mathrm{d}a}{\mathrm{d}t}\right] + \frac{E_a}{RT} = \ln A + n\ln(1-a) \tag{7}$$

The value of $\ln[Af(a)]$ can be obtained from the known values of $\ln[\mathrm{d}a/\mathrm{d}t]$ and E_a/RT. Therefore, the plot of $\ln[Af(a)]$ and $\ln(1-a)$ yields a straight line where the slope corresponds to the reaction order (n). The intercept is the natural logarithm of the frequency factor if the reaction mechanism is nth-order kinetics. Otherwise, for autocatalytic process, the Friedman plot would reveal a maximum of $\ln(1-a)$ approximately around –0.51 to –0.22 which is equivalent to degree of curing (a) of about 0.2–0.4. This is due to the autocatalytic nature that shows the maximum reaction rate to be at 20–40% conversion.

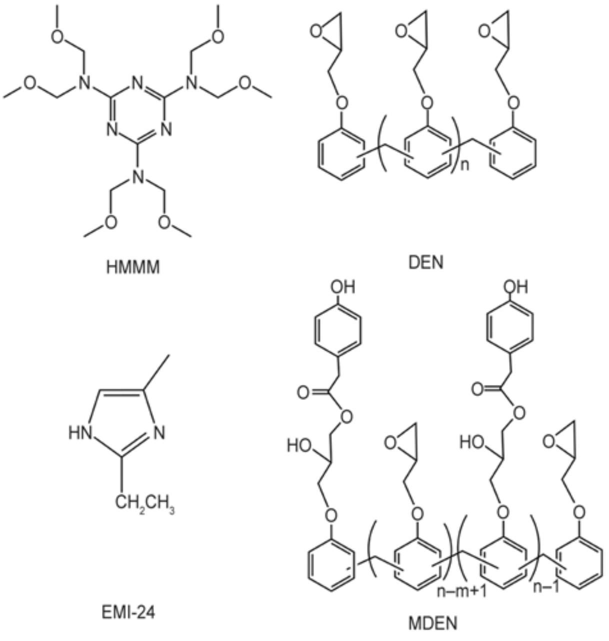

Figure 1. Chemical structures of HMMM, EMI-24, DEN and MDEN

3. Results and discussion

3.1. Reaction activities of DEN and MDEN

The reaction activities of DEN and MDEN were investigated by non-isothermal DSC with HMMM and EMI-24 as curing agent and accelerator, respectively. It can be seen from Figure 2 that there was no obvious exothermic peak appearing in the mixture of DEN/HMMM, which indicated that the reaction activity of the system was pretty low without cross linking reaction happening. Besides, in the mixture of DEN/HMMM, one sharp endothermic peak at about 155°C can be ascribed to the evaporation of residual solvent in DEN or HMMM, such as an ether. In contrast, there was a broad exothermic peak existing in MDEN/HMMM system between 85 and 275°C, which implied that the reaction activity of MDEN/HMMM system was higher than that of DEN/HMMM system. Interestingly, adding EMI-24 into the DEN/HMMM system, one obvious exothermic peak at about 150°C with much narrower

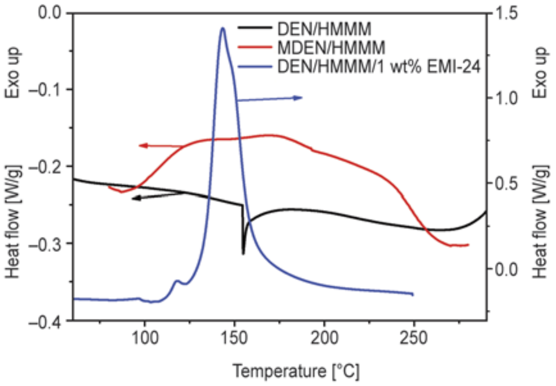

Figure 2. DSC curves based on the systems of DEN mixture and MDEN mixture at 10°C/min

temperature zone was present in the DSC curve. The higher reaction activity of MDEN was resulted from the phenol hydroxyl which could offer the acidic environment.

3.2. Non-isothermal reactions of DEN/HMMM/EMI-24 and MDEN/HMMM

The non-isothermal DSC curves for the epoxy resin system examined in the study at different heating rates ranging from 2.5 to 15°C/min were shown in Figures 3a, 3b and 3c. It can be found that two exothermic peaks were observed in the curing process of DEN/HMMM/EMI-24 as shown in Figure 3a. This phenomenon was conflicted with the curing reaction of common epoxy-amine system. For example, according to previous work of Sbirrazzuoli *et al*. [20], only a single exothermic peak was found in the stoichichiometric epoxy-amine system and the epoxy system with excess of amine. Besides, the onset, peak, and final cure temperature of exothermic peaks shifted to higher temperature area with increasing heating rates. This result can be ascribed that lower heating rates offered longer time for the reaction of chemical groups. However, at higher heating rates, there was not enough time for curing and therefore the DSC curves shifted to a higher temperature to compensate for the reduced time. In order to verify the origin of the low temperature peaks identified with arrow, the curing of DEN/EMI-24 systems was also traced at the same heating rates as shown in Figure 3b. It could be seen that the peak temperatures of DEN/EMI-24 were the same as these of DEN/HMMM/EMI-24 at lower temperature area at respective heating rates. Generally, imidazole with low content was used to catalyze and study the etherification. Heise and Martin [21] found that the –OH-adduct reaction occurred only for 1-unsubstituted imidazoleles (such as EMI-24) with a shoulder on the main exothermic peak at low EMI-24 concentrations. However, for the 1-substituted imidazoles, the OH-adduct reaction did not occur; only the O^--adduct reaction occurred through 3-N with the epoxide ring without similar shoulder. Regrettably, Heise and Martin [21] did not explain why OH-adduct reaction could form a shoulder and O^- adduct reaction could not form a shoulder. These observations were consistent with the results of Ooi *et al.* [4]. The curing mechanism of DGEBA/EMI-24 was studied by Chen and Liu [22] and they revealed that the whole curing reaction was divided into two independent stages. OH-adduct reaction and O^--adduct reaction were responsible for the first exothermic peak and etherification reaction led to the second exothermic peak.

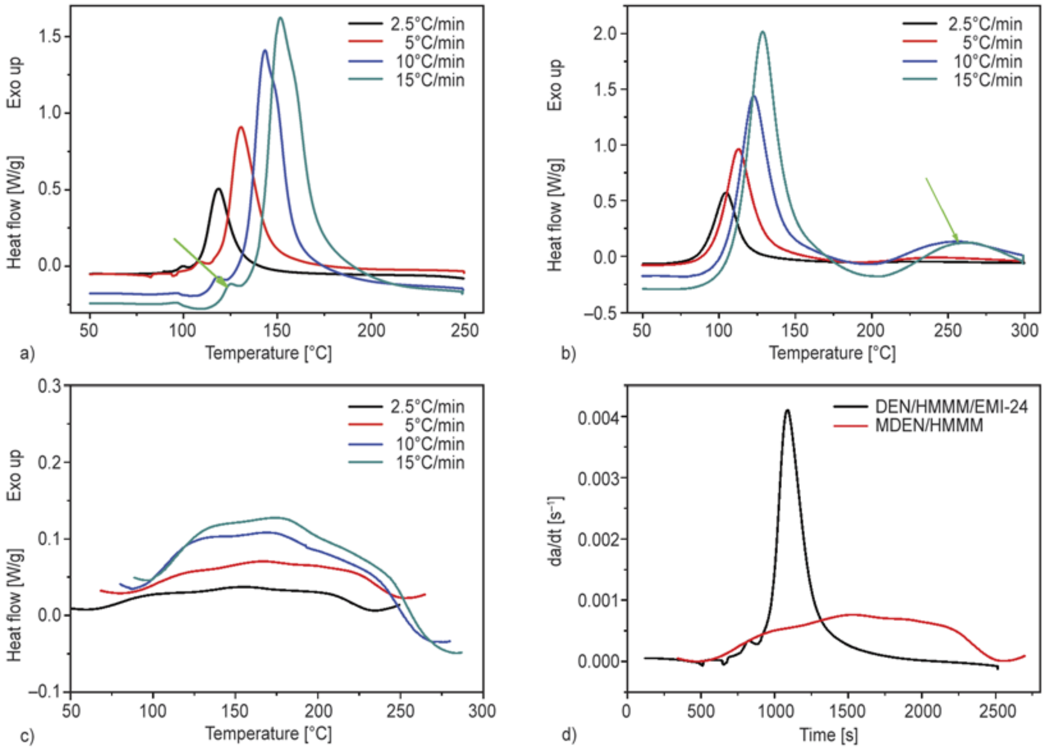

Figure 3. Non-isothermal DSC curing behavior of (a) DEN/HMMM/EMI-24, (b) DEN/EMI-24, (c) MDEN/HMMM and (d) their curing reaction rates at the heating rate of 5°C/min

However, the common results of previous work were that the first exothermic peak got smaller and smoother with the decrease of the concentrations of 1-unsubstituted imidazoles. In the previous study reported by Ooi *et al*. [4], it was difficult to observe that the lower temperature peak or shoulder was present at 1 wt% of 2-PhI. Therefore, it was understandable that no lower temperature peak or shoulder occurred in the DEN/EMI-24 system and the corresponding curing mechanism has now been generally accepted without debate. From Figure 3a and 3b, it could be concluded that the first exothermic peak was attributed to the reaction between DEN and EMI-24, and the main peak was due to the reaction between DEN and HMMM.

Figure 3c represented the dynamic thermograms of MDEN/HMMM system. Each of the DSC runs showed a broad exothermic peak with shoulders, which likely suggested that the non-isothermal reaction can be considered as a combination of different kinetics process from a statistical viewpoint [23]. Compared to DEN/HMMM/EMI-24, the value of heat flow was relatively low and stable during the whole curing process, which indicated the curing reaction was relatively mild. It would need much more time to complete the curing and decrease the internal stress during curing. This curing reaction behavior was further verified as shown in Figure 3d. For curing of DEN/HMMM/EMI-24 at the heating rate of 5°C/min, the maximum curing rate reached 0.004 s^{-1}, which was fivefold than that of MDEN/HMMMM (about 0.0008 s^{-1}). On the other hand, it needed about 2000 s to complete the curing reaction for the system of MDEN/HMMM at the above condition.

3.3. Kinetic model

From the aforementioned DSC results, it could be seen that MDEN had wider temperature range to complete the curing reaction, which indicated that their curing mechanisms were also different. In order to reveal their differences, the kinetic model was examined utilizing isoconversional methods. It was known that the reaction activation energy (E_a) represented the potential barrier and the evolution of the curing reaction [8]. As shown previously for epoxy curing, model-free iso-conversional kinetics analysis could allow one to yield reliable kinetics parameters as well as to accomplish agreement with isothermal data. Without assuming a particular form for the reaction model, these methods allow for evaluating E_a as a function of conversion (a). This E_a-a correlation usually corresponded to change of reaction mechanisms; it may reflect relative contributions of parallel reaction channels to overall reaction kinetics [24, 25]. In this work, Flynn-Wall-Ozawa method was employed to analyze the mechanism of the non-isothermal reaction. Based on Equation (4) through linear fitting of $\ln(\beta)$ versus $1/T$, the values of E_a were obtained for a particular a.

The variation of E_a with the conversion (a) and that of conversion with temperature were shown in Figure 4. It could be observed that the values of E_a varied with the increase of a and exhibited a significantly changing characteristic during the curing reaction. For DEN/HMMM/EMI-24, the curing process was characterized by a decrease in E_a from ≈80 to ≈50 kJ/mol. The decrease of E_a implied that the rate determining step of curing changed to a process with smaller E_a [26]. The curing rate was generally controlled by the rate of chemical reaction and the diffusion of reactants. When the molecular motion was hindered and molecules only experienced a series of diffusion jumps to engage in a chemical reaction, the diffusion became a rate determining factor. Therefore, the decrease in E_a was attributed to diffusion control [20]. An interpretation of this behavior of E_a variation with conversion was an apparent decrease in molecular mobility and the polymer gels or due to a kinetic compensation effect has been reported [23]. To eliminate these effects, the mean value of the E_a at the conversion of curing in ranges of 0.1–0.5, was found to be 71.05 kJ/mol, which was quite typical for epoxy/amine copolymerization [25]. However, for the sys-

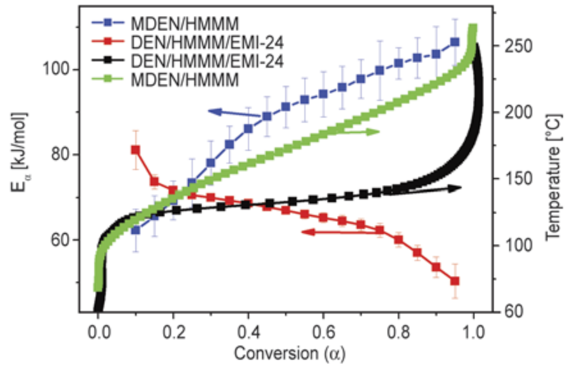

Figure 4. Variation of E_a on the conversion and the dependence of the conversion on temperature at the heating rate of 5°C/min for DEN/HMMM/EMI-24 and MDEN/HMMM systems

tem of MDEN/HMMM, the E_a of the curing process increased to ≈106 kJ/mol from the value of ≈61 kJ/mol. The increase in E_a indicated that chemical reaction was still a rate determining factor. Although, increase of the conversion resulted in the higher glass transition temperature (T_g) of the polymer products, as soon as the actual experimental temperature rose above the T_g, which did not result in the appearance of glass transition effect [27]. In MDEN/HMMM system of Figure 3d, the curing rate was so low that the curing did not increase the T_g obviously, and then the influence of chemical reaction on E_a outweighed that of the diffusion, which resulted in the increase of E_a. Besides, for MDEN/HMMM system, the mean value of E_a can be calculated as mentioned above method as 77.44 kJ/mol. From the curve of conversion vs. temperature, it can be seen that the extent of conversion in DEN/HMMM/EMI-24 was higher than that in MDEN/HMMM at the same temperature. This was consistent with the difference in the E_a and higher E_a value would lead to higher barrier [24].

To construct the kinetic model, the kinetics analysis of DSC curves was carried out by separating of the three dominant overlapping exothermic peaks using Gaussian distribution equation and analyzing the distinct characteristic of each exothermic peak. As an example of MDEN/HMMM, the DSC thermogram (solid line) and the calculated data (dashed line) with three resolved peaks were illustrated in Figure 5a, at a heating rate of 5°C/min [23, 28]. According to Flynn-Wall-Ozawa method, the variation of E_a for the three reactions at different conversion was shown in Figure 5b. It can be seen that the E_a values tended to increase with the increase of conversion for reaction 1 and the E_a values kept at a more comparative steady state for reactions 2 and 3. Besides, the mean E_a value (70.05 kJ/mol) for reaction 1 was almost the same as that (71.05 kJ/mol) of DEN/HMMM/EMI-24. This implied that the mechanism of reaction 1 was similar or same as the reaction of DEN/HMMM/EMI-24. By the aid of the catalyst (H^+), the $–OCH_3$ reacted with epoxide group and hydroxyl group as shown in Figure 9. Meanwhile, the mean E_a values for reactions 2 and 3 were 106.55 and 101.91 kJ/mol, respectively, which were in excellent agreement with those reported for etherification by Cole *et al.* [29] (101.4 kJ/mol) and Sbirrazzuoli *et al.* [30] (104 kJ/mol). This corresponding etherification was shown in Figure 9. Because the constancy of E_a indicated a single limiting process, reaction 2 was attributed to the ring-opening reaction of epoxide with phenol hydroxyl, and reaction 3 resulted from the ring-opening reaction of epoxide with hydroxyl activated by neighboring carbonyl group. From the chemical structure of MDEN, it could be seen that etherification may occur intramolecularly, which was influenced somewhat by diffusion.

In our case, the average E_a value obtained from Flynn-Wall-Ozawa method was used for the determination of the reaction order of the DEN/HMMM/EMI-24 and MDEN/HMMM. In general, the mechanisms of thermoset curing were classified into two major kinetic reactions, an n^{th}-order and an autocatalytic reaction. Friedman method was usually employed to construct kinetic model. Figure 6 depicted Friedman plots as an exemplification of DEN/HMMM/EMI-24, the reactions 1, 2 and 3 of MDEN/HMMM at a heating rate of 5°C/min. For DEN/HMMM/EMI-24, since $\ln[Af(a)]$ and $\ln(1 - a)$ were not linearly related and evidently showed a maximum in the range of the degree of conversion mentioned above. All the results suggested that cur-

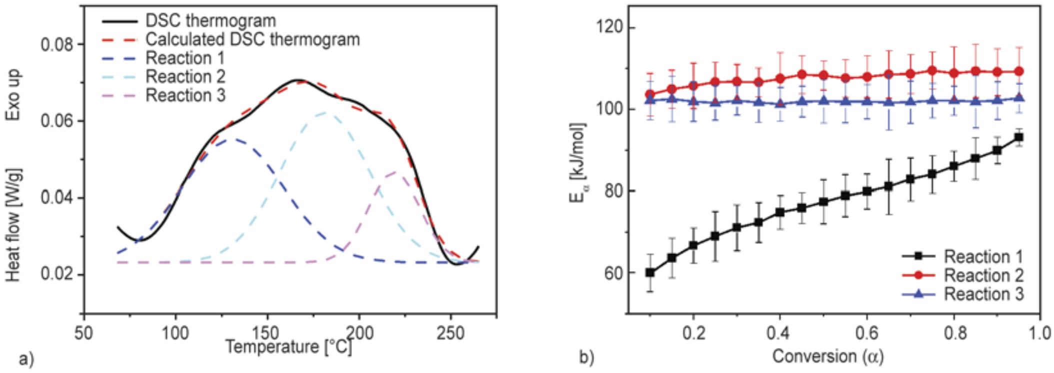

Figure 5. (a) DSC thermograms of MDEN/HMM recorded at 5°C/min and (b) values of the E_a of MDEN/HMMM obtained from Flynn-Wall-Ozawa method at different conversion of curing

ing reaction was autocatalytic in nature. The autocatalytic nature can be explained by the transformation of protons. For reactions 1, 2, and 3, $\ln[Af(a)]$ and $\ln(1-a)$ were perfectly linearly related in the range of the degree of conversion mentioned above, which indicated that all reactions were n^{th} order in nature.

For the n^{th}-order model, the kinetics parameters n and A could be obtained by the slope of the linear dependence $\ln[Af(a)]$ vs. $\ln(1-a)$, according to the Equation (7). The results of the kinetics parameters for reaction 1, reaction 2 and reaction 3 were listed in Table 1.

For the autocatalytic model, Equation (6) was transformed into Equation (8):

$$\ln[Af(a)] = \ln\left[\frac{\mathrm{d}a}{\mathrm{d}t}\right] + \frac{E_a}{RT} = \ln A + n\ln(1-a) + m\ln(a) \qquad (8)$$

Equation (8) can be solved by multiple linear regression, in which the dependent variable was $\ln(\mathrm{d}a/\mathrm{d}t)$, and the independent variables were $\ln(a)$, $\ln(1-a)$ and $1/T$. The results of the multiple linear regressions analysis for DEN/HMMM/EMI-24 were listed in Table 2. It can be seen that the variations of A, m, and n with the heating rate were in the same ranges as those reported by Hardis *et al.* [13].

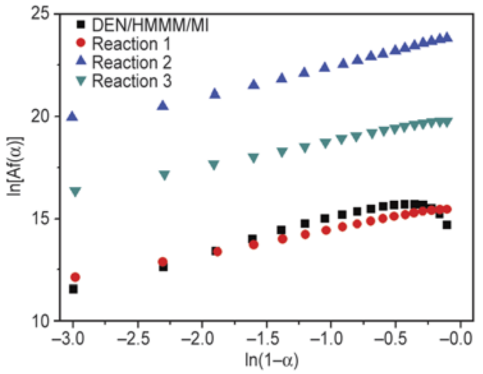

Figure 6. Plots of $\ln[Af(a)]$ vs. $\ln(1-a)$ of DEN/HMMM/EMI-24 and MDEN/HMMM based on the E_a from Flynn-Wall-Ozawa method at a heating rate of 5°C/min

3.4. Isothermal FTIR analysis

To elucidate the cross-linking mechanism, FTIR spectroscopy could be employed to track the changes of chemical bonds during the process of curing reaction. The rotation and vibration information was very specific to the chemical bonds, and the peaks in the spectrum corresponded to certain chemical bonds allowing simple identifications. The relative intensity of peaks was also directly proportional to the relative concentration of the components in a sample [31–33]. Isothermal FTIR analysis of the curing of DEN/HMMM/EMI-24 and MDEN/HMMM

Table 1. The kinetics parameters evaluated and their standard deviation (SD) for the curing of MDEN/HMMM system

	Heating rate [°C/min]	**E/SD [kJ/mol]**	**ln A [s^{-1}]**	**Mean/SD**	**n**	**Mean/SD**
Reaction 1	2.5	70.05/5.85	16.14	16.25/0.26	1.31	1.24/0.05
	5		15.96		1.21	
	10		16.34		1.25	
	15		16.57		1.20	
Reaction 2	2.5	106.55/1.57	23.91	24.26/0.24	1.43	1.58/0.10
	5		24.38		1.61	
	10		24.31		1.64	
	15		24.45		1.62	
Reaction 3	2.5	101.91/0.37	20.10	20.04/0.08	1.28	1.26/0.04
	5		20.03		1.23	
	10		19.94		1.27	
	15		20.11		1.27	

Table 2. The kinetics parameters evaluated and their standard deviation (SD) for the curing of DEN/HMMM/EMI-24 system

Heating rate [°C/min]	**E/SD [kJ/mol]**	**ln A [s^{-1}]**	**Mean/SD**	**n**	**Mean/SD**	**m**	**Mean/SD**
2.5	71.05/4.24	17.90	17.82/0.25	2.13	2.29/0.22	1.18	1.25/0.16
5		17.73		2.11		1.13	
10		18.11		2.59		1.48	
15		17.52		2.33		1.21	

with definite curing temperatures (160 and 200°C) and different curing time (0, 30, 45 and 60 min) were shown in Figures 7a, 7b and 7c, respectively. To the three samples, the specific peak at 1550 cm^{-1} attributed to stretching vibration of triazine ring remained unchanged throughout the curing reaction and could be considered as an internal standard. Meanwhile, their corresponding changes of group intensity at various times were also depicted in Figures 7d, 7e and 7f. The peaks at 915 cm^{-1} were corresponded to the epoxide group and the intensity was observed to decrease over time during the curing reaction. The decrease can be explained by the opening of the epoxide group in the curing process. Besides, it can be found that the characteristics peak at 1385 cm^{-1} assigned to –CH$_3$ stretching vibration in amino resin also decreased due to its reaction with epoxide group and hydroxyl group. Surprisingly, the peaks at 3447 cm^{-1} assigned to –OH stretching vibration increased over time in DEN/HMMM/EMI-24 system, which was due to the higher reaction activity of epoxide than that of hydroxyl, and the produced –OH was more than the consumed –OH, and these –OH increased the polar of cured polymer [34–37]. The relative high polarity of –OH resulted in high dielectric constant and water absorption, and the results were consistent with our previous works [15]. While in MDEN/HMMM system, the –OH decreased over time, and the higher curing temperature improved the conversion rate of reactive groups.

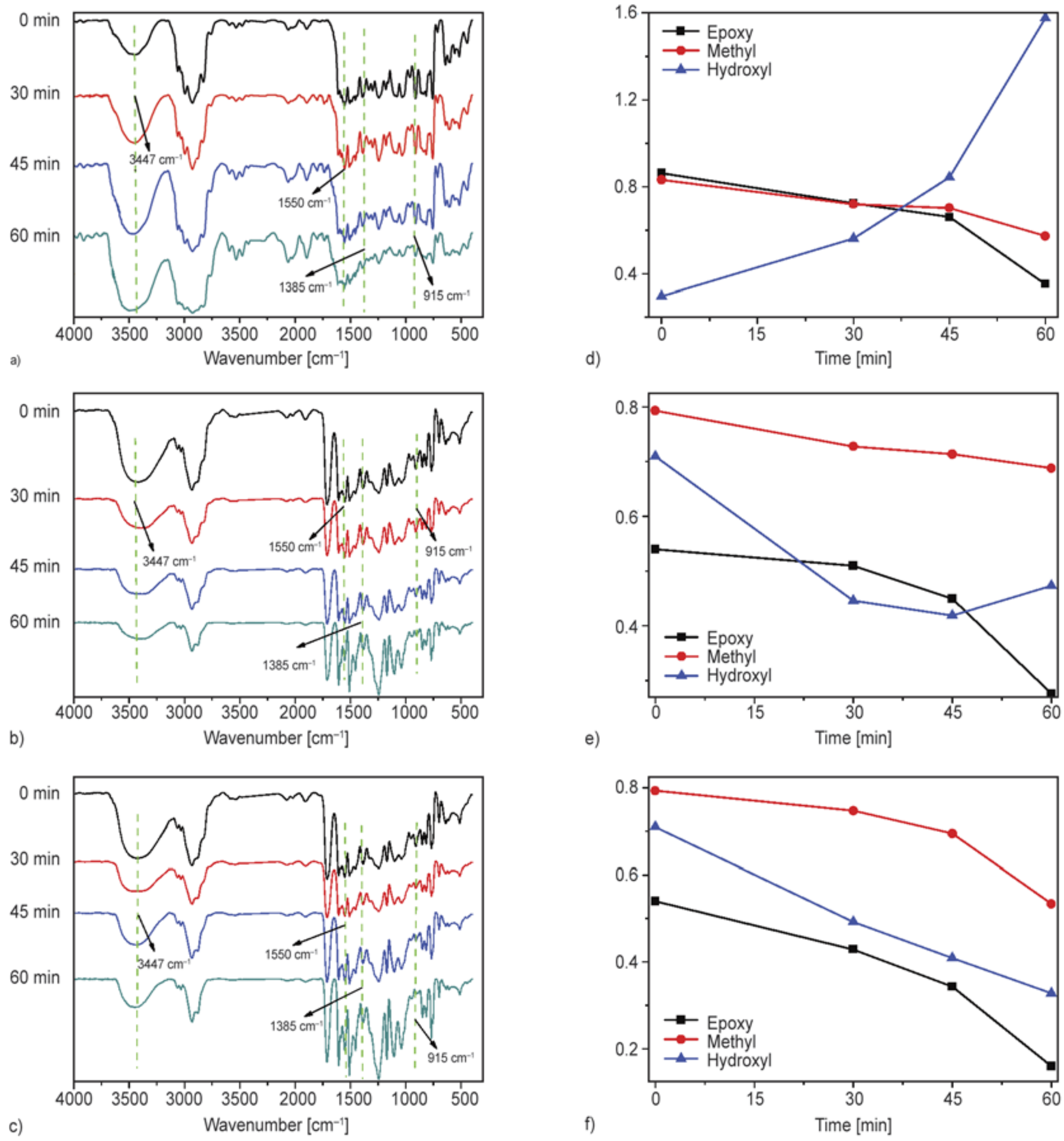

Figure 7. FTIR spectra of three samples at various curing time and their relative intensity change of different reactive groups: DEN/HMMM/EMI-24 at 160°C （a, d）; MDEN/HMMM at 160°C (b, e); MDEN/HMMM at 200°C (c, f)

3.5. Mechanism of DEN/HMMM/EMI-24 and MDEN/HMMM

According to the above results of DSC, FTIR and other relative studies [7, 21, 22, 38], the mechanisms of DEN/HMMM/EMI-24 and MDEN/HMMM were proposed as shown in Figures 8 and 9. From Figure 8, it could be seen that the transformation of proton can afford the acidic environment to assist the reaction between DEN and HMMM. Besides, due to the higher activity of epoxide, the produced –OH was more than the consumed –OH. Therefore, these mechanisms could explain that the kinetic model was autocatalytic and the cured DEN resin had higher dielectric constant and water absorption. Furthermore, from Figure 9, it was observed that phenol hydroxyl can afford the acidic environment, therefore, the phenol hydroxyl and the hydroxyl activated by carboxyl could attack the epoxide and methoxy group, which made the cross linking in intermolecular and intramolecular simultaneously. Compared with DEN/HMMM/EMI-24, the viscosity had less effect on the reaction in MDEN/HMMM, which could illustrate that the E_a increased with conversion.

3.6. Analysis of chemorheological behavior

In order to relate the viscosity of the reactive system to the reaction kinetics, the oscillatory shear flow

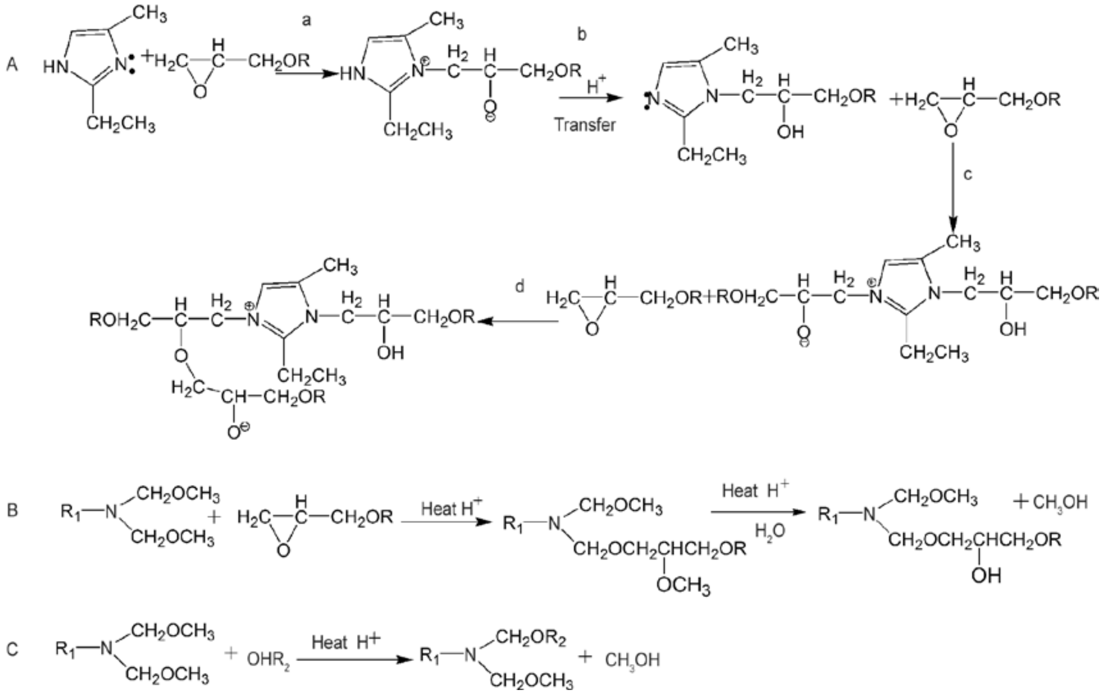

Figure 8. Proposed mechanism for the cure of DEN/HMMM/EMI-24

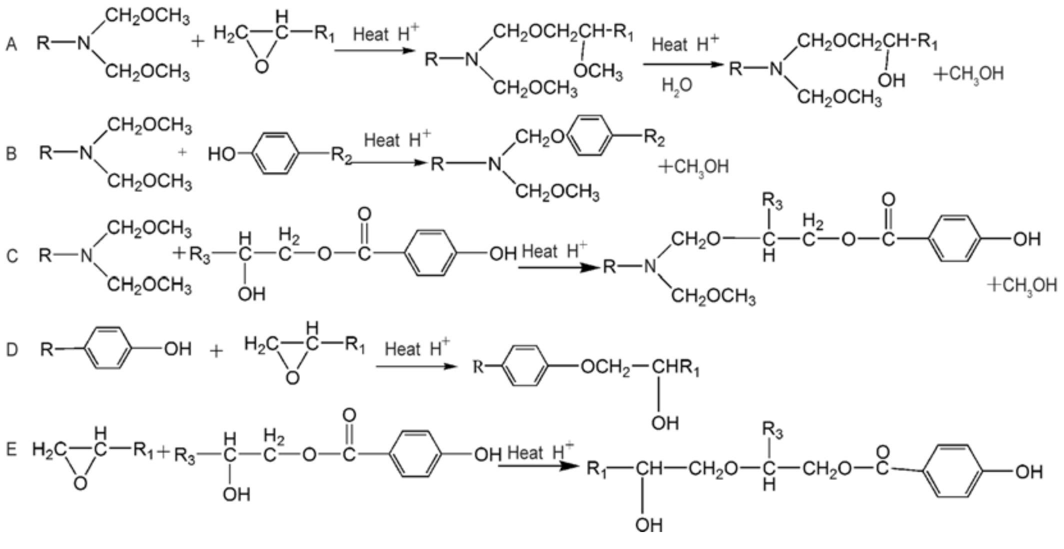

Figure 9. Proposed mechanisms for the cure of MDEN/HMMM

measurements were performed under non-isothermal condition as the thermocalorimetric measurements. The complex viscosity and the conversion as function of the temperature were plotted in Figure 10. At the beginning, the complex viscosity decreased with temperature, and then a lowest viscosity was obtained at a certain temperature. Thereafter, a very rapid increase of the viscosity was observed with obvious gelation. The following plateau in complex viscosity with temperature appeared ascribing to the dynamic modulus [14]. Besides, for DEN/HMMM/EMI-24, when the conversion (a) was below 0.2, the low complex viscosity cannot hinder the diffusion of molecule chains. Therefore, the curing was controlled by chemical reaction in this region. Meanwhile, when the conversion (a) was above 0.2, the viscosity increased rapidly with conversion, the diffusion of molecule chains got difficult, and the curing reaction was controlled by diffusion. Oppositely, for MDEN/HMMM, even the conversion (a) reached to 0.9, the viscosity was too low to hinder the diffusion of molecular chains. Therefore, the cure reaction was controlled by chemical reaction during almost the whole process. All these results were consistent with E_a. Moreover, the lowest viscosity can be considered as the watershed in control mechanism of viscosity. Before the watershed, the viscosity was sensitive to temperature and could be controlled by temperature. Therefore, this mode was called physical mechanism of viscous falling. After the watershed, increased temperature could only change the trend in viscosity increase and not decrease the viscosity of reactive system; this mode was called chemical mechanism of viscous increase. These control mechanism could conduct us to obtain better plastics products during resin molding [39, 40].

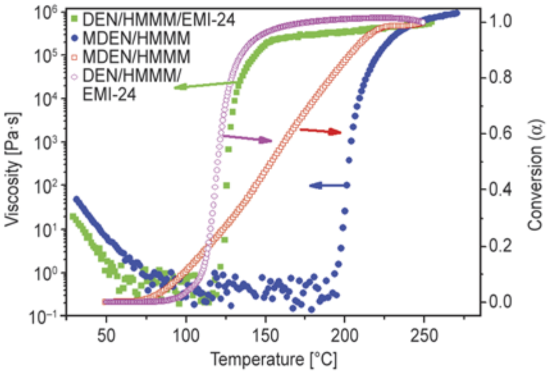

Figure 10. Variation of complex viscosity on temperature and the dependence of the conversion on temperature at the heating rate of 2.5°C/min for DEN/HMMM/EMI-24 and MDEN/HMMM system

4. Conclusions

The curing kinetics of epoxy novolac resin (DEN) and modified epoxy novolac resin (MDEN) with methanol etherified amino resin were studied. The curing reaction of DEN resin mixture was autocatalytic in nature, due to the transformation of protons and its average E_a was calculated to be 71.05 kJ/mol. The curing of MDEN resin mixture was consisted of three dominant reactions (reactions 1, 2 and 3), as evidenced by the presence of two shoulders in the DSC thermograms. Thereinto, the activation energy value of the reaction 1 was similar to that of the DEN resin curing; the activation energy values of reactions 2 and 3 were almost constant (106.55 and 101.91 kJ/mol, respectively), which were close to those of etherification. The reaction 2 was attributed to the ring-opening reaction of epoxide with phenol hydroxyl, and the reaction 3 was resulted from the ring-opening reaction of epoxide with hydroxyl activated by neighboring carbonyl group. Their possible mechanisms were proposed via the results of FTIR and DSC. At last, chemorheological behavior was also characterized to instruct us preparing better plastics products via controlling viscosity.

Acknowledgements

This work was financially supported by Guangdong and Shenzhen Innovative Research Team Program (No. 2011D052, KYPT20121228160843692), National Natural Science Foundation of China (Grant No. 21201175) and R&D Funds for basic Research Program of Shenzhen (Grant No. JCYJ20120615140007998).

References

[1] Lin C. H., Wang Y. R., Feng Y. R., Wang M. W., Juang T. Y.: An approach of modifying poly(aryl ether ketone) to phenol-containing poly(aryl ether) and its application in preparing high-performance epoxy thermosets. Polymer, **54**, 1612–1620 (2013).
DOI: 10.1016/j.polymer.2013.01.034

[2] Li T., Qiu H. J., Liu Y., Zhong X. H., Yu Y. F., Serra A.: Hyperbranched polyester as additives in filled and unfilled epoxy-novolac systems. Polymer, **53**, 5864–5872 (2013).
DOI: 10.1016/j.polymer.2012.10.028

[3] Xu K., Chen M. C., Zhang K., Hu J. W.: Synthesis and characterization of novel epoxy resin bearing naphthyl and limonene moieties, and its cured polymer. Polymer, **45**, 1133–1140 (2004).
DOI: 10.1016/j.polymer.2003.12.035

[4] Ooi S. K., Cook W. D., Simon G. P., Such C. H.: DSC studies of the curing mechanisms and kinetics of DGEBA using imidazole curing agents. Polymer, **41**, 3639–3649 (2000).
DOI: 10.1016/S0032-3861(99)00600-X

[5] Liu W. B., Qiu Q. H., Wang J., Huo Z. C., Sun H.: Curing kinetics and properties of epoxy resin–fluorenyl diamine systems. Polymer, **49**, 4399–4405 (2008).
DOI: 10.1016/j.polymer.2008.08.004

[6] Pan G. Y., Du Z. J., Zhang C., Li C. J., Yang X. P., Li H. Q.: Synthesis, characterization, and properties of novel novolac epoxy resin containing naphthalene moiety. Polymer, **48**, 3686–3693 (2007).
DOI: 10.1016/j.polymer.2007.04.032

[7] Lv Y., Song C., Long Z., Luo S. Y.: Curing reaction kinetic of a diglycidyl ether of bisphenol A with a methanol etherified amino resin (in Chinese). China Printing and Packaging Study, **3**, 44–49 (2011).
DOI: 10.3969/j.issn.1674-5752.2011.06.008

[8] Fu Y., Zhong W. H.: Cure kinetics behavior of a functionalized graphitic nanofiber modified epoxy resin. Thermochimica Acta, **516**, 58–63 (2011).
DOI: 10.1016/j.tca.2011.01.016

[9] Ke L. L., Hu D., Lu Y. B., Feng S., Xie Y. Y., Xu W. J: Copolymerization of maleimide-based benzoxazine with styrene and the curing kinetics of the resultant copolymer. Polymer Degradation and Stability, **97**, 132–138 (2012).
DOI: 10.1016/j.polymdegradstab.2011.11.011

[10] Liu L., Ye Z. P.: Effects of modified multi-walled carbon nanotubes on the curing behavior and thermal stability of boron phenolic resin. Polymer Degradation and Stability, **94**, 1972–1978 (2009).
DOI: 10.1016/j.polymdegradstab.2009.07.022

[11] Yoo M. J., Kim S. H., Park S. D., Lee W. S., Sun J. W. Choi J. H., Nahm S.: Investigation of curing kinetics of various cycloaliphatic epoxy resins using dynamic thermal analysis. European Polymer Journal, **46**, 1158–1162 (2010).
DOI: 10.1016/j.eurpolymj.2010.02.001

[12] Han S. O., Drzal L. T.: Curing characteristics of carboxyl functionalized glucose resin and epoxy resin. European Polymer Journal, **39**, 1377–1384 (2003).
DOI: 10.1016/S0014-3057(03)00036-3

[13] Hardis R., Jessop J. L. P., Peters F. E., Kessler M. R.: Cure kinetics characterization and monitoring of an epoxy resin using DSC, Raman spectroscopy, and DEA. Composites Part A: Applied Science and Manufacturing, **49**, 100–108 (2013).
DOI: 10.1016/j.compositesa.2013.01.021

[14] Ivankovic M., Incarnato L., Kenny J. M., Nicolais L.: Curing kinetics and chemorheology of epoxy/anhydride system. Journal of Applied Polymer Science, **90**, 3012–3019 (2003).
DOI: 10.1002/app.12976

[15] Zhao S. F., Zhang G. P., Sun R., Wong C. P.: Multifunctionalization of novolac epoxy resin and its influence on dielectric, thermal properties, viscoelastic and aging behavior. Journal of Applied Polymer Science, in press (2013).

[16] Sbirrazzuoli N., Vyazovkin S.: Learning about epoxy cure mechanisms from isoconversional analysis of DSC data. Thermochimica Acta, **388**, 289–298 (2002).
DOI: 10.1016/S0040-6031(02)00053-9

[17] Kissinger H. E.: Reaction kinetics in differential thermal analysis. Analytical Chemistry, **29**, 1702–1706 (1957).
DOI: 10.1021/ac60131a045

[18] Ozawa T.: A new method of analyzing thermogravimetric data. Bulletin of the Chemistry Society of Japan, **38**, 1881–1886 (1965).
DOI: 10.1246/bcsj.38.1881

[19] Friedman H. L.: Kinetics of thermal degradation of char-forming plastics from thermogravimetry. Application to a phenolic plastic. Journal of Polymer Science Part C: Polymer Symposia, **6**, 183–195 (1965).
DOI: 10.1002/polc.5070060121

[20] Sbirrazzuoli N., Vyazovkin S., Mititelu A., Sladic C., Vincent L.: A study of epoxy-amine cure kinetics by combining isoconversional analysis with temperature modulated DSC and dynamic rheometry. Macromolecular Chemistry and Physics, **204**, 1815–1821 (2003).
DOI: 10.1002/macp.200350051

[21] Heise M. S., Martin G. C.: Curing mechanism and thermal properties of epoxy-imidazole systems. Macromolecules, **22**, 99–104 (1989).
DOI: 10.1021/ma00191a020

[22] Chen P., Liu L. Z.: Curing mechanism, kinetic, reactivities of epoxy resins system cured with 2-ethyl-4-methylmidazole (in Chinese). Acta Polymerica Sinica, **6**, 641–646 (1994).

[23] Jubsilp C., Punson K., Takeichi T., Rimdusit S.: Curing kinetics of benzoxazine–epoxy copolymer investigated by non-isothermal differential scanning calorimetry. Polymer Degradation and Stability, **95**, 918–924 (2010).
DOI: 10.1016/j.polymdegradstab.2010.03.029

[24] Zhang Y. Y., Vyazovkin S.: Comparative cure behavior of DGEBA and DGEBP with 4-nitro-1,2-phenylenediamine. Polymer, **47**, 6659–6663 (2006).
DOI: 10.1016/j.polymer.2006.07.058

[25] Zvetkov V. L.: Comparative DSC kinetics of the reaction of DGEBA with aromatic diamines.: I. Non-isothermal kinetic study of the reaction of DGEBA with *m*-phenylene diamine. Polymer, **42**, 6687–6697 (2001).
DOI: 10.1016/S0032-3861(01)00160-4

[26] Lu M. G., Shim M. J., Kim S. W.: Curing reaction and phase change in a liquid crystalline monomer. Macromolecular Chemistry and Physics, **202**, 223–230 (2001).
DOI: 10.1002/1521-3935(20010101)202:2<223::AID-MACP223>3.0.CO;2-X

[27] Gan L., Sun Z. J., Gu Y. Z., Li M., Zhang Z. G.: Epoxy resin curing reaction studied by dynamic and isothermal model free kinetics. Acta Polymerica Sinica, **8**, 1016–1022 (2010).
DOI: 10.3724/SP.J.1105.2010.09319

[28] Wan J. T., Li B. G., Fan H., Bu Z. Y., Xu C. J.: Non-isothermal reaction, thermal stability and dynamic mechanical properties of epoxy system with novel nonlinear multifunctional polyamine hardener. Thermochimica Acta, **511**, 51–58 (2010).
DOI: 10.1016/j.tca.2010.07.024

[29] Cole K. C., Hechler J. J., Noel D.: A new approach to modeling the cure kinetics of epoxy/amine thermosetting resins. 2. Application to a typical system based on bis[4-(diglycidylamino)phenyl]methane and bis(4-aminophenyl) sulfone. Macromolecules, **24**, 3098–3110 (1991).
DOI: 10.1021/ma00011a012

[30] Sbirrazzuoli N., Mititelu-Mija A., Vincent L., Alzina C.: Isoconversional kinetic analysis of stoichiometric and off-stoichiometric epoxy-amine cures. Thermochimica Acta, **447**, 167–177 (2006).
DOI: 10.1016/j.tca.2006.06.005

[31] Li G., Huang Z. B., Li P., Xin C. L., Jia X. L., Wang B. H., He Y. D., Ryu S. K., Yang X. P.: Curing kinetics and mechanisms of polysulfone nanofibrous membranes toughened epoxy/ amine systems using isothermal DSC and NIR. Thermochimica Acta, **497**, 27–34 (2010).
DOI: 10.1016/j.tca.2009.08.005

[32] Passos S. P., Kimpara E. T., Bottino M. A., Santos G. C. Jr., Rizkalla A. S.: Effect of ceramic shade on the degree of conversion of a dual-cure resin cement analyzed by FTIR. Dental Materials, **29**, 317–323 (2013).
DOI: 10.1016/j.dental.2012.11.014

[33] Recalde L. B., Recalde D., García-Lopera R., Gómez C. M.: FTIR isothermal cure kinetics and morphology of dicyanate ester resin/polysulfone blends. European Polymer Journal, **41**, 2635–2643 (2005).
DOI: 10.1016/j.eurpolymj.2005.05.027

[34] Zhao S. F., Cheng L., Guo Y., Zheng Y. Y., Li B. M.: PA6 and Kevlar fiber reinforced isotactic polypropylene: Structure, mechanical properties and crystallization and melting behavior. Materials and Design, **35**, 749–753 (2012).
DOI: 10.1016/j.matdes.2011.10.039

[35] Zhao S. F., Qiu S. C., Zheng Y. Y., Cheng L., Guo Y.: Synthesis and characterization of kaolin with polystyrene via *in-situ* polymerization and their application on polypropylene. Materials and Design, **32**, 957–963 (2011).
DOI: 10.1016/j.matdes.2010.07.020

[36] Bortolato S. A., Thomas K. E., McDonough K., Gurney R. W., Martino D. M.: Evaluation of photo-induced crosslinking of thymine polymers using FT-IR spectroscopy and chemometric analysis. Polymer, **53**, 5285–5294 (2012).
DOI: 10.1016/j.polymer.2012.09.007

[37] Xiong X. H., Chen P., Ren R., Lu F., Yu Q.: Cure mechanism and thermal properties of the phthalide-containing bismaleimide/epoxy system. Thermochimica Acta, **559**, 52–58 (2013).
DOI: 10.1016/j.tca.2013.02.025

[38] Hong X. Y., Chen Q. D., Chen L., Chen M., Wu R. G., Mao H. Q.: Studies on the energy compensation effect in the hybrid polymerization of hexamethoxymethyl melamine(HMMM)-polyol-acrylate (in Chinese). Chemical Journal of Chinese Universities, **23**, 744–747 (2003).

[39] Dai X. Q., Zeng J. C., Xiao J. Y., Jiang D. Z., Yin C. P.: A new method for predicting the viscosity of reactive resin systems (in Chinese). Acta Materiea Compositae Sinica, **27**, 78–85 (2010).

[40] Monti M., Puglia D., Natali M., Torre L., Kenny J. M.: Effect of carbon nanofibers on the cure kinetics of unsaturated polyester resin: Thermal and chemorheological modelling. Composites Science and Technology, **71**, 1507–1516 (2011).
DOI: 10.1016/j.compscitech.2011.06.010

eXPRESS Polymer Letters Vol.8, No.2 (2014) 107–115
Available online at www.expresspolymlett.com
DOI: 10.3144/expresspolymlett.2014.13

Percolated conductive polyaniline-clay nanocomposite in polyvinyl chloride through the combined approach porous template and self-assembly

J. D. Sudha*, S. Sivakala, C. K. Chandrakanth, K. S. Neethu, K. N. Rohini, R. Ramakrishnan

Chemical Sciences and Technology Division, National Institute for Interdisciplinary Science and Technology (NIIST), CSIR, 695 019 Thiruvananthapuram, India

Received 31 July 2013; accepted in revised form 8 October 2013

Abstract. In this paper, we are reporting a novel strategy for the preparation of conductive polyaniline-clay nanocomposite in Polyvinylchloride (PVC) matrix by admicellar emulsion polymerization using a low cost renewable resource based surfactant cum dopant. The highly oriented percolated network of polyaniline-clay nanocomposite in PVC matrix was revealed from the studies made by scanning electron microscopy (SEM) and atomic force microscopy (AFM). Fourier transform infrared spectroscopy (FTIR) results suggested that porous template was formed by the noncovalent interactions among the hydroxyl groups present in the nanoclay edges and the chloride ions present in PVC matrix. Here, the bio-based surfactant, 4-hydroxy-2-pentadecyl benzene-1-sulphonic acid (PDPSA) performed multiple roles of dopant, emulsifier and soft template during the polymerization of anilinium$^+$PDPSA$^-$ (An$^+$PDPSA$^-$) in PVC-clay matrix. The prepared composite exhibited electrical conductivity (σ_{dc}) of $4.8\cdot10^{-2}$ S/cm and electromagnetic interference shielding efficiency (EMI SE) of 55.2 dB suggesting it as a prospectable candidate for the encapsulation of electronic devices in high technological applications.

Keywords: *nanocomposites, admicellar emulsion polymerization, conducting polymers*

1. Introduction

Nanostructured electrically conducting polymer composites are explored largely due to their combined properties of the conventional polymers such as ease of processability, low density, environmental stability and corrosion resistance with electrical properties of conducting polymers. Literature reveals that conducting polymers with nanoscale morphologies including tubes, wires and fibres can be constructed by either self-assembly [1, 2] or template approach [3–6] for the fabrication of electronic devices such as batteries, capacitors, light emitting diodes and sensors. Development of polyaniline (PANI) wires using self-assembled micelle of amphiphilic dopant by self-assembly approach has been reported earlier [7]. Carswell *et al*. [8] and other authors [9–11] have used adsorbed surfactants as templates for the synthesis of morphologically controlled PANI and polypyrrole nanowires on flat surfaces. Babu *et al*. [12] proposed solvent directed self-assembly of π–gelators for the preparation of hierarchically aligned orthophenylene vinylene amide nanofibers on polystyrene matrix. Polystyrene micro porous materials with porosity ranging from micro to nano range prepared through the sublimation of solvent by Guenet and coworkers [13, 14]. A new way to pattern conjugated polymers with nanoscale dimensions on a solid surface has been described by admicellar polymerization (AP) [15]. AP can be visualized as a technique analogous to emulsion polymerization where the adsorbed bilayered surfactant aggregates are used as tem-

---

*Corresponding author, e-mail: sudhajd2001@yahoo.co.in plates on various surfaces. Interactions between polymers and surfactants in the bulk have been extensively reviewed due to its relevance in many industrial applications.

Small diameter, high aspect ratio, excellent conductivity, and high thermo-mechanical stability are required to create conductive composites for high performance applications. Researchers have shown that nanocomposites with different morphologies can be produced by tuning of polymer-clay interactions [16–21]. Synthesis of conducting polyaniline-clay nanocomposites (PCN) is receiving attention in this respect since they are associated with the above mentioned novel properties. We have reported earlier that 'PDPSA' derived from cashew nut shell liquid played multiple role of intercalating agent, structure directing agent and dopant during the formation of nanostructured PCNs [14, 22]. In the present work, we are reporting a novel strategy for the preparation of highly oriented percolated patterns of PCN in PVC matrix (PVCPCN) using a combined mechanism of porous template and self-assembly approach. Onset of percolation threshold concentration (PTC) was manifested from the morphological studies in combination with electrical conductivity measurements. The entanglement among the clay, PANI and PVC in PVCPCN composite was manifested from rheological measurements and FTIR. Electrical conductivity, thermal properties and EMI SE of these composites were evaluated.

2. Experimental

2.1. Materials

Bentonite clay with cation exchange capacity of 80 meq/100 g and a chemical formula of $(Na, Ca)_{0..33}(Al_{1.67}Mg_{0.33})Si_4O_{10}(OH)_2{\cdot}nH_2O$ was purchased from Loba Chemie, Bombay, India. Aniline monomer, methyl alcohol and ammonium persulphate (APS) obtained from s.d.fine chem limited, Bombay, India. PDPSA was prepared through the sulphonation of 3-pentadecyl phenol, (cashew export promotion council, India) based on the procedure reported earlier [8]. Polyvinyl chloride [molecular weight: M_n = 61 500, M_w = 88 500, PDI = 1.4] was procured from Nikunj enterprises, Bombay, India. Aniline was vacuum distilled prior to use.

2.1.1. Preparation of An^+PDPSA^- micelle

An^+PDPSA^- micelles were prepared by mixing stoichiometric proportion of 0.025 g of aniline ($2.9{\cdot}10^{-3}$ mole) and 0.011 g ($2.9{\cdot}10^{-3}$ mole) of PDPSA in water at 60°C for 1 hr.

2.1.2. Preparation of PVC-Clay dispersion

2.5 g of PVC in 250 mL chloroform was taken in a 500 mL three-necked round bottomed flask and was fitted with a mechanical stirrer and a reflux condenser. Then it was heated with stirring under reflux for 1 hr until the complete dispersion of PVC. Clay dispersion was prepared separately by stirring 0.025 g clay in 25 mL water at 60°C for 4 hrs. Then the prepared clay dispersion was added drop wise to the PVC dispersion and stirred well for getting a homogeneous system.

2.1.3. Preparation of electrically conductive PVCPCN

Electrically conductive PCN percolates in PVC matrix were prepared by admicellar polymerization of 'An^+PDPSA^-' in PVC – clay dispersion using APS as oxidant initiator. 100 mL of 10^{-3} M solution of An^+PDPSA^- was added drop wise to the PVC-clay dispersion and stirred for 2 hrs. The mixture was then cooled down to 0°C by keeping in an ice bath and a solution of APS (0.03 mole) dissolved in 50 mL water was added drop wise to initiate the polymerization. Reaction continued for another 3 to 4 hrs. The emeraldine green colored conductive composite formed was isolated by precipitating from methanol. It was then filtered, washed several times with methanol and dried in a vacuum oven for 3 days at 60°C. The purified product is designated as PVCPCN. The procedure was repeated for developing composites with varying weight percentage of conductive PCN and the details are depicted in Table 1.

The same procedure is repeated for the preparation of composites without clay and was designated as PVCPN and the details were given in Table 1. PANICN and PANI-PDPSA were prepared as per the procedure reported earlier [22].

2.2. Fabrication of conductive films

Electrically conductive PVCPCN and PVCPN composites were cast into film from an electrically heated film making press. The compression moulded samples (thickness 10 mm, planar area $5.2{\cdot}10^{-4}$ m^2) were prepared by keeping the composites at 100°C for five minutes under pressure. Then films were allowed to cool at room temperature and measurements were made after keeping for 24 hr.

Table 1. Electrical conductivity and EMI SE of PVCPN and PVCPCN composites

Sample code	wt% of PANI	wt% of clay	Conductivity [S/cm]	EMI SE [dB] at 10 GHz
PVC	0.0	–	–	–
PANI-PDPSA	100.0	–	3.5	–
PVCPN 1	5.0	–	$2.33\cdot10^{-4}$	7.1
PVCPN 2	7.5	–	$2.45\cdot10^{-2}$	8.2
PVCPN 3	10.0	–	$2.20\cdot10^{-2}$	14.8
PVCPCN 1	2.5	10	$8.46\cdot10^{-6}$	35.3
PVCPCN 2	5.0	10	$4.26\cdot10^{-4}$	56.7
PVCPCN 3	7.5	10	$4.73\cdot10^{-4}$	66.0
PVCPCN 4	10.0	10	$4.58\cdot10^{-4}$	73.2

2.3. Characterization techniques

UV-Vis absorption spectra of the PVCPCN composites were studied using UV-Vis spectrophotometer [Shimadzu model 2100, Japan] in the range of 300–1100 nm. FT-IR measurements of the composites were made using fully computerized Nicolet impact 400D FT-IR spectrophotometer (Czech Republic, EU). X-ray diffraction studies were done using powder X-ray diffractometer (Philips X'pert Pro, Netherlands) with CuK_α radiation ($\lambda \sim 0.154$ nm) employing X'celarator detector and monochromator at the diffraction beam side. Thin films casted on glass plates were used employing standard sample holder. Electrical conductivity (σ_{dc}) of films was measured using the standard spring loaded pressure contact four probe conductivity meter supplied by Keithley (Germany) as per the standard procedure ASTM F 43-99. The conductivity (σ_0) was calculated using Van der Pauw relation $\sigma_0 = [\ln2/(\pi\cdot d)]\cdot(I/V)$. Where d is the thickness of the film, I is the current and V is the voltage. Morphology of the hard and soft template formation was observed under AFM. Images were recorded under ambient conditions using Ntegra multimode Nanoscope IV (Netherlands) operating in the tapping mode regime. Micro fabricated silicon cantilever tips (MPP-11100-10) with a resonance frequency of 284–299 kHz and a spring constant of 20–80 Nm^{-1} were used. The scan rate varied from 0.5 to 1.5 Hz. Complementary studies were made using scanning electron microscope (SEM, JEOL make, model JSM 5600 LV,Germany) at 15 kV accelerating voltage. ESEM experiments with the dispersion of PVC-clay were carried out using the FEG Quanta ESEM instrument (Hitachi, Japan). TEM measurements were carried out using FEI (Tecnai G2 30 S-TWIN, USA) with an accelerating voltage of 100 kV. For TEM measurements, the sample solutions were coated on a formvar coated copper grid and dried in vacuum at room temperature before observation. Thermal analysis of the composites was performed with TA instruments (Differential Scanning Calorimetry 2920, Switzerland) instrument under nitrogen atmosphere. Rheological property of the conductive composite was measured using Modulated Compact Rheometre-150 Physica (Germany). Parallel plate sensor with a diameter of 50 mm and a gap size of 0.25 mm were used and measurements were done in dynamic oscillatory mode at 100°C (frequency range 0.001–1000 rad/s). EMI SE of the prepared samples have been measured using a laboratory developed one-port coaxial sample holder backed by short on Vector network analyzer (VNA) Wiltron 37247B (Germany) in the desired frequency range. The return loss (RLin dB) of the sample was measured on the calibrated VNA by connecting the one port sample holder at the test port without and with the sample. Half of this measured RL is the EMI SE of the sample in dBs.

3. Results and discussion

3.1. Mechanism for the formation of 'percolated conductive composite, PVCPCN

Percolated pattern of electrically conductive PVCPCN prepared by admicellar oxidative radical polymerization of $\text{An}^+\text{PDPSA}^-$ in PVC-clay dispersion using APS as initiator and is shown in Figure 1. Formation of 'porous template' was manifested from the studies made using SEM, AFM and TEM in combination with FTIR. FT-IR spectra of PANI, PVC-clay dispersion, PVC, PVCPCN and clay are shown in Figure 2, respectively. PANI showed characteristic bands at 1552 and 1483 cm^{-1} (stretching vibration of quinoid ring and benzenoid ring), 3100 cm^{-1}(N-H str), 2900 and 2850 cm^{-1}(C-H str), and 1297 cm^{-1}(C-N). PVC exhibited charac-

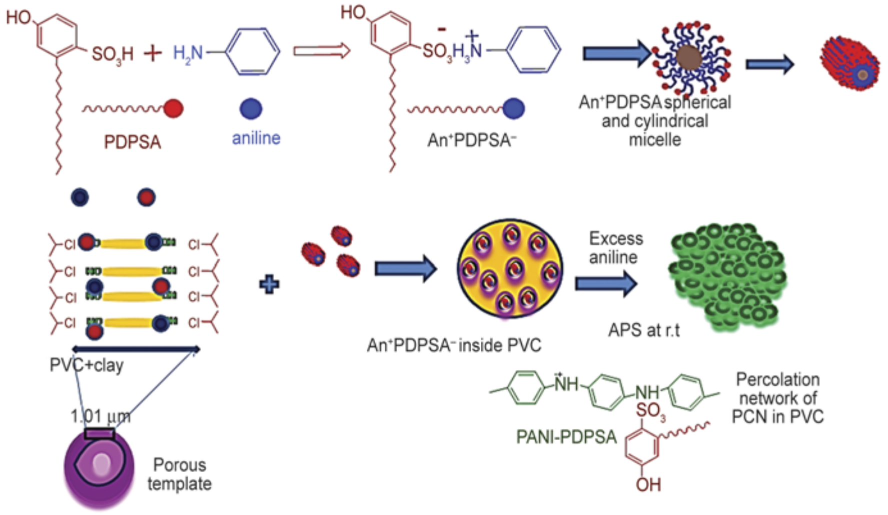

Figure 1. Preparation of conductive composite

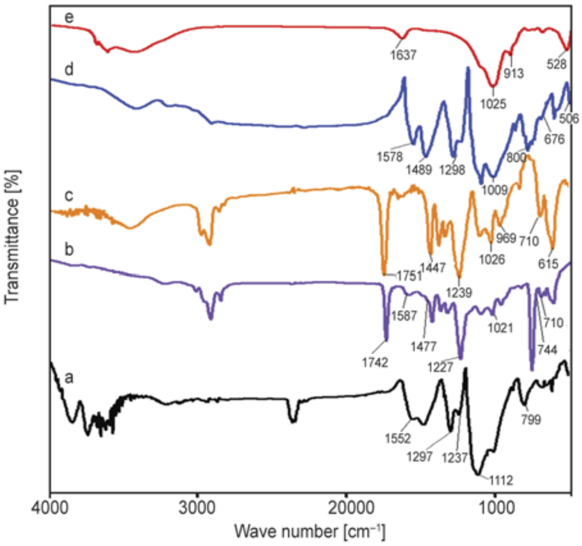

Figure 2. FT-IR spectra of (a) PANI, (b) PVC clay dispersion, (c) PVC, (d) PVCPCN, (e) clay

teristic bands at 1447 cm^{-1}(CH_2), 1239 cm^{-1}(C-H of CHCl), 1026 cm^{-1}(C-C), 969 cm^{-1}(CH_2 rocking) and 710, 615 cm^{-1}(C-Cl) [12]. Clay showed characteristic peaks at 1025 cm^{-1} [υ (Si-O)], 913 cm^{-1} [υ (Al-OH)] and 528 cm^{-1} [υ (Si-O-Al)]. However, the FTIR spectra of PVC-clay dispersion exhibited the bands at 1477, 1227, 1021, 744 and 710 cm^{-1}. The observed shift in the bands of PVC-clay dispersion compared to the characteristic bands of PVC and clay revealed the presence of noncovalent interactions among clay and PVC moieties. These interactions are responsible for the formation of porous template. Microscopic analysis of PVC-clay dispersion exhibited almost uniform microporous shapes having pore diameter of ~1.5 µm ESEM and ordinary SEM images were shown in Figure 3a and 3b, respectively. Dimension of the pore size and thickness were further confirmed by AFM studies and the corresponding image of the PVC-clay was shown in Figure 3c. The AFM image of a single pore is given in Figure 3e and its height profile is depicted in Figure 3d. Pore size of the template is measured to be ~1.32 µm which is almost matching with the observation from SEM analysis and wall thickness of the pore is measured as ~100 nm. The pore wall was formed by parallel stack of silicate layers and its aggregates through edge to edge association as reported earlier [23]. Further formation of porous template was confirmed by TEM analysis and the image of the same is given in Figure 4. Here also the image measured pore size of ~1.3 µm with well defined wall thickness of 98 nm.

FTIR spectrum of PVCPCN exhibited bands at 1578, 1489, 1298, 1009, 800, 676, 506 cm^{-1} and shown in Figure 2 curve d. The observed shift in the positions of bands in PVCPCN compared to the characteristic bands of PANI, clay and PVC can be ascribed due to the formation of noncovalent interaction among the clay, PANI and PVC moieties. Thus, the various noncovalent and covalent interactions among the various entities present in clay, PANI and PVC are responsible for the formation of steady and uniform films.

The mechanism for the formation of steady and uniform conductive films can be explained by the results obtained from FTIR and morphological analysis. Initially, aniline combines with the amphiphilic dopant PDPSA to form An^+PDPSA^- by the acid-base reaction. Later they will self-assemble in water to form cylindrical micelles as shown in Figure 1.

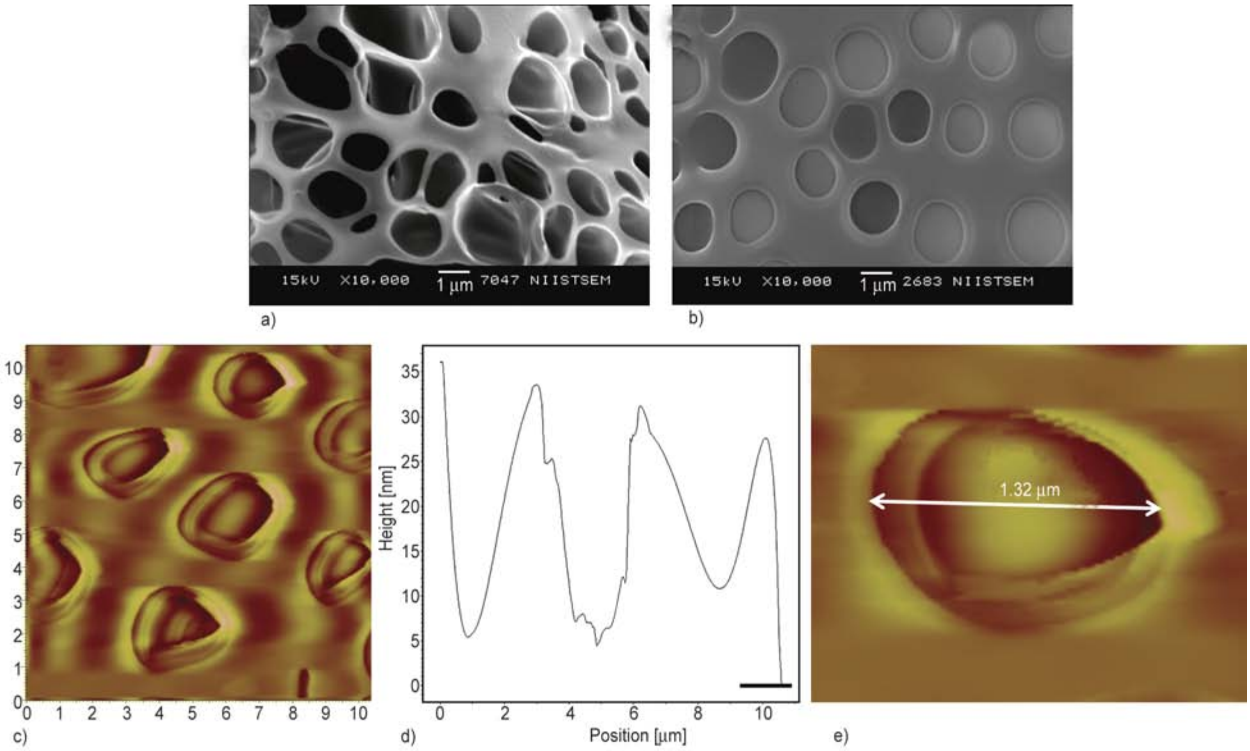

Figure 3. SEM image of porous template (a) ESEM, (b) ordinary SEM, (c) AFM image of PVC-clay pores, (d) AFM profile of porous template, (e) AFM image of a single pore

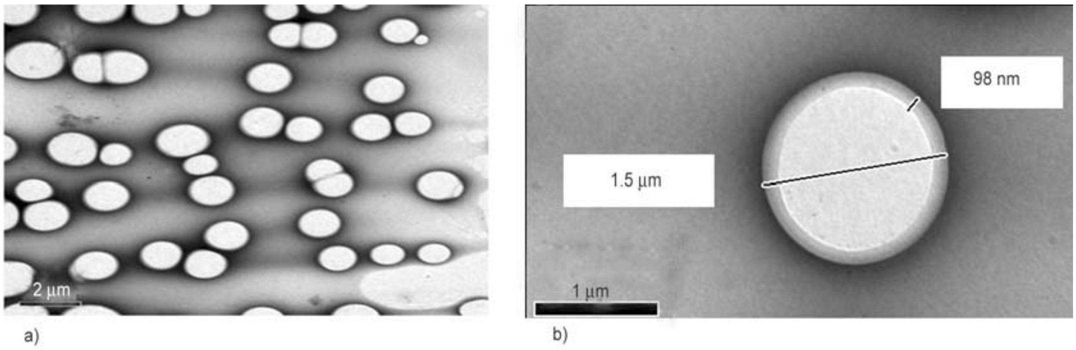

Figure 4. TEM image of (a) porous templates of PVC-clay, (b) single pore

During agitation An^+PDPSA^- micelles present in the emulsion can be easily introduced into the hydrophilic pores present in PVC-clay dispersion through the driving force of interfacial attraction between the hydrophilic charges present in the walls of the pore towards the micelle. In the presence of excess aniline, some portion of the aniline will imbibe inside the cylindrical micelle and some portion will be retaining in the chloroform layer. In the presence of oxidative radical intiator APS, polymerization initiates inside the pore and propagates through the walls. Similar polymerization propagation process guided by the hydrophilic groups present in the hard template was reported earlier and it strengthens our observation [24–26]. As polymerization proceeds further, the various covalent and noncovalent interactions among clay tactoids, PVC and PANI become stronger and this may cause collapsing the walls of pores to form percolated network structure in PVCPCN. This mechanism is supported by the studies made by other researchers [27]. The AFM micrographs of PVCPCN are shown in Figure 5a (cast in glass plate) and Figure 5b (casted in HOPG plate). SEM picture of the same is given as Figure 5c. Both micrographs exhibited percolated wires of PCN (bright shade) in PVC matrix (dark shade) having micrometer in length and diameter of ~20 nm. The AFM height profiles of the same are shown in Figure 5d and 5e respectively. Topographical analysis showed that the heights of the PCN particles are in ~5 to 20 nm suggesting the formation of nanostructured conducting particles of

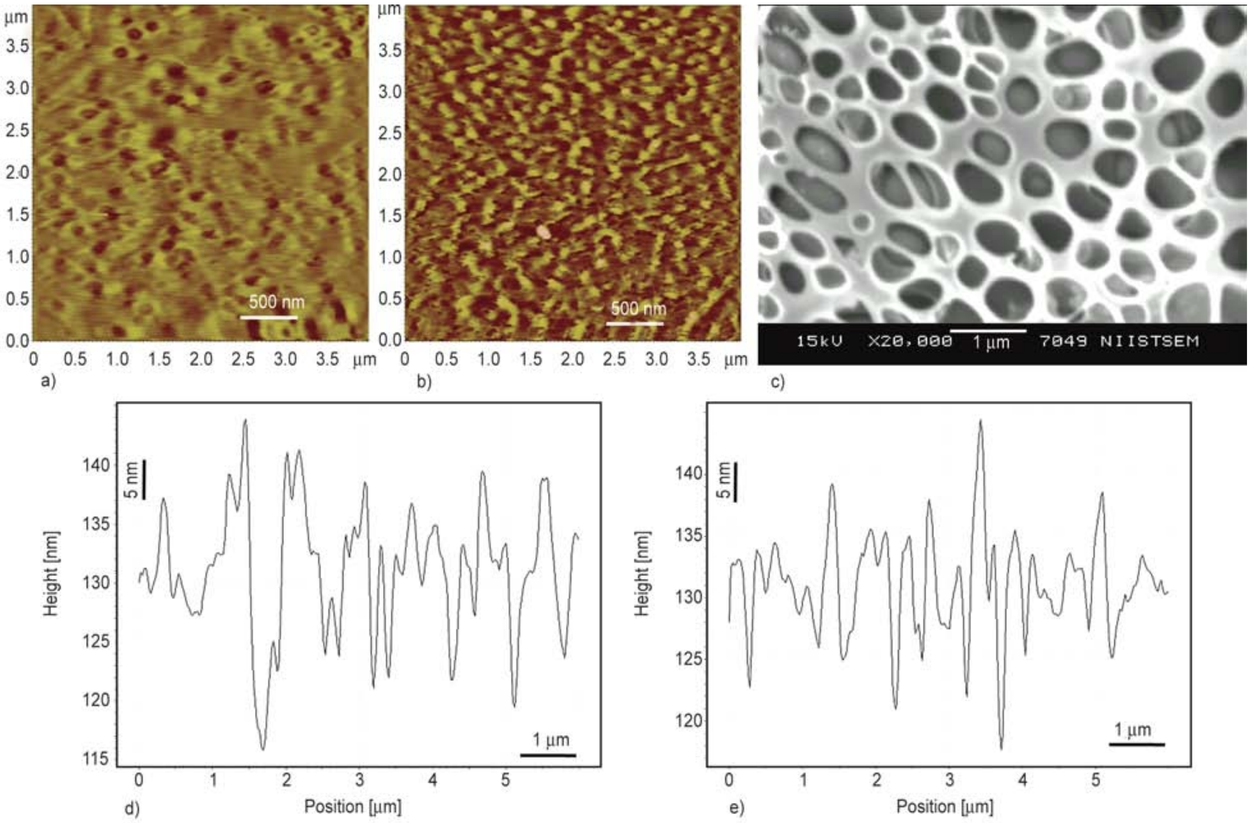

Figure 5. AFM micrographs of PVCPCN observed during the onset of percolation (a) casted in glass plate, (b) casted in HOPG substrate and (c) SEM image of PVCPCN (d, e) AFM height profile of PVCPCN during onset of polymerization casted in glass plate and HOPG substrate respectively

PCN in PVC matrix. The surface roughness of the film was measured to be 1.776 nm. Based on the morphological and spectroscopic experimental evidence, a plausible mechanism for the formation of highly oriented percolated structures of nanowires of PCN in PVC is illustrated as per Figure 1.

3.2. UV-Vis spectroscopy

Electronic state of the conductive composite was manifested from UV-Vis spectroscopy. UV-vis spectra of PANI, PCN, PVCPN and PVCPCN are shown in Figure 6. PANI exists in the emeraldine salt state. PANI exhibited three peaks at (i) 340 nm corresponding to π–π* transition of benzenoid structure, (ii) 440 nm corresponding to the polaron band to π* (iii) 700–900 nm corresponding to π-polaron bandpresent in the PANI chain. However, PCN and PVCPN exhibited a broad absorption maximum at 460 nm due to the merging of two initial peaks (330 and 460 nm) and a second absorption maximum at 750 nm. The absorption spectra of PVCPCN showed similar pattern with a red shift in the polaron band with a free carrier tail at 900 nm. This red shift observed in the composites when compared to PVCPN is due to the formation of more number of delocalized charge carriers present in the polaron band.

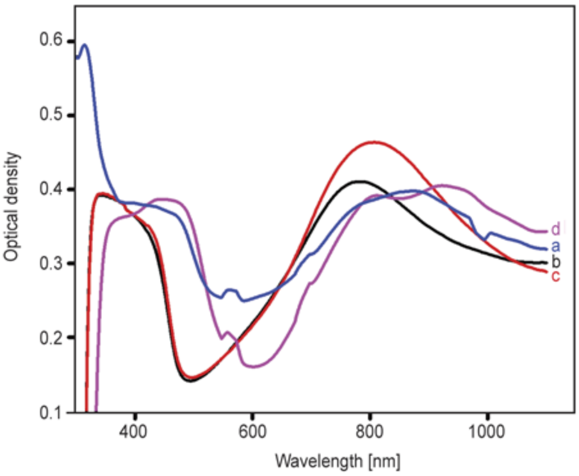

Figure 6. UV-visible spectra of (a) PANI, (b) PCN, (c) PVCPN, (d) PVCPCN

3.3. X-ray diffraction studies

X-ray diffractograms of clay, PANI-PDPSA, PVCPN and PVCPCN were recorded using thin films of samples having 100 µm thicknesses and are shown

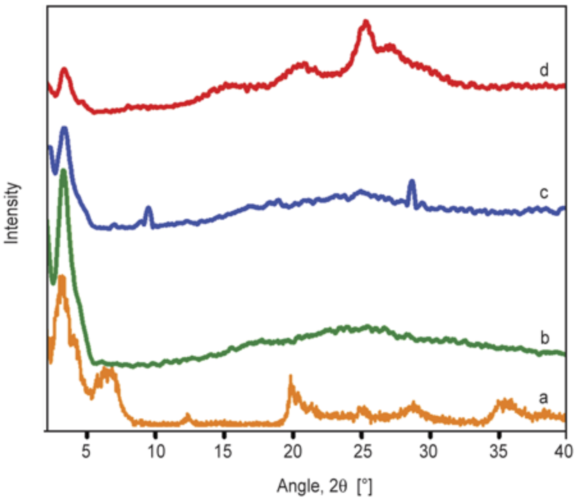

Figure 7. XRD plots of (a) clay, (b) PANI-PDPSA, (c) PVCPN, (d) PVCPCN

in Figure 7. Clay showed d001 basal spacing of 12.1 Å at 2θ = 6.7° corresponding to the distance between the layers along the c-axis direction. PANI exhibited characteristic broad peak at 2θ = 23.4° and a sharp reflection at 2θ = 3.4° corresponding to the self assembled aggregated structure. PVCPN exhibited diffraction peaks at 2θ = 3.3, 9.4, 28.6° with d-spacing of 25.5, 9.0, 3.0 Å respectively. In PVCPCN, the diffraction peak corresponding to the d_{001} plane of clay completely shifted to 2θ = 3.3° with d-spacing of 26.4 Å and might have merged with the aggregated peak of self assembled PANI-PDPSA.It exhibited peaks at broad peaks at 20.52, 25.22, 27.26° with d-spacing of 4.21, 3.43 and 3.18 Å, respectively.

3.4. Electrical conductivity and EMI shielding efficiency

Electrical conductivity measurement of the PVCPN and PVCPCN were done using thin films of uniform thickness and the values are depicted in Table 1. PANI-PDPSA exhibited conductivity of 3.5 S/cm. PTC of the conductive material in the composite was determined by plotting electrical conductivity measurements against the concentration of conductive material. It was observed that electrical conductivity exhibited a plateau beyond certain concentration and is considered as the onset of a conductive path in the matrix. This value depends upon the shape and size distribution of conductive particles in the polymer matrix and has been applied to describe electrical conductivity observations within various composites. For PVCPN, PTC is observed to be 7.5 weight percentage with conductivity $2.45\cdot10^{-2}$ S/cm and that of PVCPCN showed PTC at 5 weight percentage with conductivity $4.26\cdot10^{-2}$ S/cm. Similar observations were made by other researchers [28]. Thus, the electrical conductivity measurement also substantiated the formation of more ordered conductive network in presence of clay. This observation is complimentary to the observations from SEM and AFM.

Effect of PVCPN and PVCPCN on EMI SE was studied and the details are showed in Table 1. It was observed that as the amount of conductive filler loading increased, EMI SE also showed a hike in the values. The EMI SE of conductive films of PVCPN containing PANI 5, 7.5 and 10% were measured to be 7.1, 8.2 and 14.8 dB respectively. EMI SE measurement of PVCPCN films containing conductive fillers of 2.5, 5, 7.5 and 10% exhibited EMI SE of 35.3, 56.7 66 and 73.2 dB respectively. The higher EMI SE value observed for PVCPCNs is attributed from the higher extent of attenuation favoured by the multiple reflection mechanism induced by the nano clay layers having high interfacial area [29]. Thus the films containing PCNs could attenuate electromagnetic radiation by two mechanisms of absorption and multiple reflections.

3.5. DSC

PVC showed a thermal transition at 75°C corresponding to the glass transition of PVC. PANI exhibited a broad endothermic transition at 106°C due to breaking of the intermolecular hydrogen bonding present in the bulk PANI. PVCPN exhibited a broad endothermic transition between 79–106°C which can be considered as the energy transition due to the noncovalent interaction among the various moieties present in PVCPN. But PVCPCN showed three transitions between 102–123°C, which can be ascribed due to the unwinding of PCN chains through breaking the noncovalent interactions between clay tactoids and PVC.

3.6. Rheology

The presence of exfoliated nanoclay layers and the interaction between the conductive filler-host matrix was manifested from rheological property measurements. Loss modulus (G'') and storage modulus (G') were measured as a function of frequency at 100°C under angular frequency sweep of 0.001 to 1000 rad/sec at 5% strain. The G' is related to the

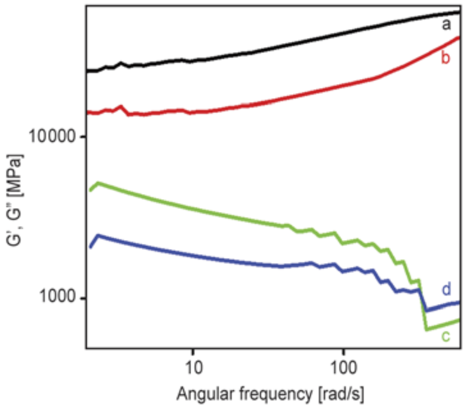

Figure 8. Variation of G' and G'' with angular frequency: (a) G' of PVCPCN (b) G'' of PVCPCN (c) G' of PVCPN and (d) G'' of PVCPN

ability of the material to store energy when an oscillatory force is applied to the specimen and the G'' is related to the ability to lose the energy. These properties were measured to examine the degree of entanglement in the conductive composite of PVCPCN. Variation of G' and G'' with angular frequency of PVCPN and PVCPCN are shown in Figure 8. Both exhibited distinctly different oscillatory responses. G' and G'' of PVCPCN is found to be greater than that of PVCPN. This could be due to the presence of entanglement induced by the percolated nanoaggregates present in PVCPCN [30, 31].

4. Conclusions

In summary, electrically conductive films with highly ordered percolated conductive network pattern (PVCPCN) were successfully prepared by self-assembly cum porous template based strategy. Here, the surfactant cum dopant, PDPSA derived from a low cost renewable resource based product could function as soft template and structure-directing agent. Thus the combination of self-assembly growth with hydrophilic porous template allows the formation of large scale percolated patterns of nanowires. This capability in retaining template without post processing is challenging in organic electronic devices. Moreover, property evaluation of this material exhibited excellent electrical conductivity and EMI SE which makes them a promising candidate for EMI/electrostatic dissipating matrix for high technological applications. Further, the proposed strategy can be exploited for the development of percolated patterns of nanostructured conductive molecules in other insulative matrices for the fabrication of nanoelectronic devices.

Acknowledgements

We thank the Indian Space Research Organization ISRO RESPOND (GAP 109439) programme and CSIR NWP-54 for their financial support. We are also thankful to Dr. Suresh Das, Director, NIIST, CSIR, TVM for all the encouragement and support and Dr. A. Ajayaghosh, NIIST, Trivandrum and Mr. M.R. Chandran, Kiran Mohan, Mr. P. Guruswamy, NIIST Trivandrum, for SEM, TEM and WAXRD analysis.

References

[1] Zhang Z., Wei Z., Wan M.: Nanostructures of polyaniline doped with inorganic acids. Macromolecules, **35**, 5937–5942 (2002).
DOI: 10.1021/ma020199v

[2] Jang J., Yoon H.: Facile fabrication of polypyrrole nanotubes using reverse microemulsion polymerization. Chemical Communications, **6**, 720–721 (2003).
DOI: 10.1039/B211716A

[3] Shi L., Wu X., Lu L., Yang X., Wang X.: Molecular mechanism for formation of polyaniline lamella from a lyotropic liquid crystal: An NMR study. Journal of Physical Chemistry B, **113**, 2725–2733 (2009).
DOI: 10.1021/jp9002824

[4] Rabatic B. M., Pralle M. U., Tew G. N., Stupp S. I.: Nanostructured semiconductors templated by cholesteryl-oligo(ethylene oxide) amphiphiles. Chemistry of Materials, **15**, 1249–1255 (2003).
DOI: 10.1021/cm020899e

[5] Hong B. H., Lee J. Y., Lee C-W., Kim J. C., Bae S. C., Kim K. S.: Self-assembled arrays of organic nanotubes with infinitely long one-dimensional H-bond chains. Journal of the American Chemical Society, **123**, 10748–10749 (2001).
DOI: 10.1021/ja016526g

[6] Collins S. K., Yap G. P. A., Fallis A. G.: The synthesis of a novel strained diyneparacyclophane and its dimer by metal-mediated coupling. Angewandte Chemie International Edition, **39**, 385–388 (2000).
DOI: 10.1002/(SICI)1521-3773(20000117)39:2<385::AID-ANIE385>3.0.CO;2-I

[7] Qiu H., Zhai J., Li S., Jiang L., Wan M.: Oriented growth of self-assembled polyaniline nanowire arrays using a novel method. Advanced Functional Materials, **13**, 925–928 (2003).
DOI: 10.1002/adfm.200304366

[8] Carswell A. D. W., O'Rea E. A., Grady B. P.: Adsorbed surfactants as templates for the synthesis of morphologically controlled polyaniline and polypyrrole nanostructures on flat surfaces: From spheres to wires to flat films. Journal of the American Chemical Society, **125**, 14793–14800 (2003).
DOI: 10.1021/ja0365983

[9] Jadhav A. S., Maldar N. N., Shinde B. M., Vernekar S. P.: Synthesis and characterization of silicon-containing polyamides from aromatic sulfone ether diamines and aromatic organosilicon diacid chlorides. Journal of Polymer Science Part A: Polymer Chemistry, **37**, 147–153 (1991).
DOI: 10.1002/pola.1991.080290202

[10] Zhang X., Zhang J., Liu Z., Robinson C.: Inorganic/organic mesostructure directed synthesis of wire/ribbon-like polypyrrole nanostructures. Chemical Communications, **16**, 1852–1853 (2004).
DOI: 10.1039/B405255B

[11] Abdou M. S. A., Xie Z. W., Leung A. M., Holdcroft S.: Laser, direct-write microlithography of soluble polythiophenes. Synthetic Metals, **52**, 159–170 (1992).
DOI: 10.1016/0379-6779(92)90304-2

[12] Babu S. S., Mahesh S., Kartha K. K., Ajayaghosh A.: Solvent-directed self-assembly of π gelators to hierarchical macroporous structures and aligned fiber bundles. Chemistry – An Asian Journal, **4**, 824–829 (2009).
DOI: 10.1002/asia.200900145

[13] Malik S., Roizard D., Guenet J-M.: Multiporous material from fibrillar syndiotactic polystyrene intercalates. Macromolecules, **39**, 5957–5959 (2006).
DOI: 10.1021/ma060770g

[14] Dasgupta D., Manna S., Malik S., Rochas C., Guenet J. M., Nandi A. K.: Thermodynamic structural and morphological investigation of poly(vinylidene fluoride)–camphor systems, preparing porous gels from a solid solvent. Macromolecules, **38**, 5602–5608 (2005).
DOI: 10.1021/ma050582a

[15] Pongprayoon T., Yanumet N., O'Rear E. A.: Admicellar polymerization of styrene on cotton. Journal of Colloid and Interface Science, **249**, 227–234 (2002).
DOI: 10.1006/jcis.2002.8230

[16] Okada A., Usuki A.: Twenty years of polymer-clay nanocomposites. Macromolecular Materials and Engineering, **291**, 1449–1476 (2006).
DOI: 10.1002/mame.200600260

[17] Tjong S. C.: Structural and mechanical properties of polymer nanocomposites. Materials Science and Engineering R: Reports, **53**, 73–197 (2006).
DOI: 10.1016/j.mser.2006.06.001

[18] Ren J., Krishnamoorti R.: Nonlinear viscoelastic properties of layered-silicate-based intercalated nanocomposites. Macromolecules, **36**, 4443–4451 (2003).
DOI: 10.1021/ma020412n

[19] Haraguchi K., Ebato M., Takehisa T.: Polymer–clay nanocomposites exhibiting abnormal necking phenomena accompanied by extremely large reversible elongations and excellent transparency. Advanced Materials, **18**, 2250–2254 (2006).
DOI: 10.1002/adma.200600143

[20] Toombes G. E. S., Mahajan S., Thomas M., Du P., Tate M. W., Gruner S. M., Wiesner U.: Hexagonally patterned lamellar morphology in ABC triblock copolymer/aluminosilicate nanocomposites. Chemistry of Materials, **20**, 3278–3287 (2008).
DOI: 10.1021/cm702842b

[21] Negrete-Herrera N., Putaux J-L., David L., De Haas F., Bourgeat-Lami E.: Polymer/laponite composite LATEXES: Particle morphology, film microstructure, and properties. Macromolecular Rapid Communications, **28**, 1567–1573 (2007).
DOI: 10.1002/marc.200700212

[22] Sudha J. D., Reena V. L., Pavithran C.: Facile green strategy for micro/nano structured conducting polyaniline-clay nanocomposite via template polymerization using amphiphilic dopant, 3-pentadecyl phenol 4-sulphonic acid. Journal of Polymer Science Part B: Polymer Physics, **45**, 2664–2673 (2007).
DOI: 10.1002/polb.21273

[23] Kieffer J.: Mechanical degradation and viscous dissipation in B_2O_3. Physical Review B, **50**, 17–29 (1994).
DOI: 10.1103/PhysRevB.50.17

[24] Sudha J. D., Sivakala S.: Conducting polystyrene/polyaniline blend through template-assisted emulsion polymerization. Colloid and Polymer Science, **287**, 1347–1354 (2009).
DOI: 10.1007/s00396-009-2101-5

[25] Nam P. H., Maiti P., Okamoto M., Kotaka T., Hasegawa N., Usuki A.: A hierarchical structure and properties of intercalated polypropylene/clay nanocomposites. Polymer, **42**, 9633–9640 (2001).
DOI: 10.1016/S0032-3861(01)00512-2

[26] Nair B. P., Pavithran C., Sudha J. D., Prasad V. S.: Microvesicles through self-assembly of polystyrene–clay nanocomposite. Langmuir, **26**, 1431–1434 (2010).
DOI: 10.1021/la903360e

[27] Pielichowski K.: Thermal degradation of poly(vinyl chloride)/polyaniline conducting blends. Journal of Thermal Analysis and Calorimetry, **54**, 171–175 (1998).
DOI: 10.1023/A:1010129205138

[28] Conn C., Booth N., Unsworth J.: Preparation of a flexible polyaniline-pvc composite. Advanced Materials, **7**, 790–792 (1995).
DOI: 10.1002/adma.19950070905

[29] Yang S., Lozano K., Lomeli A., Foltz H. D., Jones R.: Electromagnetic interference shielding effectiveness of carbon nanofiber/LCP composites. Composites Part A: Applied Science and Manufacturing, **36**, 691–697 (2005).
DOI: 10.1016/j.compositesa.2004.07.009

[30] Filippone G., Dintcheva N. T., Acierno D., La Mantia F. P.: The role of organoclay in promoting co-continuous morphology in high-density poly(ethylene)/poly(amide) 6 blends. Polymer, **49**, 1312–1322 (2008).
DOI: 10.1016/j.polymer.2008.01.045

[31] Wang Y., Jing X.: Intrinsically conducting polymers for electromagnetic interference shielding. Polymers for Advanced Technologies, **16**, 344–351 (2005).
DOI: 10.1002/pat.589

eXPRESS Polymer Letters Vol.8, No.2 (2014) 116–122
Available online at www.expresspolymlett.com
DOI: 10.3144/expresspolymlett.2014.14

Fast curing ethylene vinyl acetate films with dual curing agent towards application as encapsulation materials for photovoltaic modules

H-Y. Xue[1,2], W-H. Ruan[2*], M-Q. Zhang[2], M-Z. Rong[2]

[1]Key Laboratory for Polymeric Composite and Functional Materials of Ministry of Education, Zhongshan University, 510275 Guangzhou, P. R. China
[2]Materials Science Institute, The School of Chemistry and Chemical Engineering, Zhongshan University, 510275 Guangzhou, P. R. China

Received 7 August 2013; accepted in revised form 8 October 2013

Abstract. To speed up curing of ethylene vinyl acetate (EVA) films as encapsulation materials for photovoltaic modules, a dual curing agent of benzoyl peroxide (BPO) and butylperoxy 2-ethylhexyl carbonate (TBEC) was introduced in this work. The experimental results indicated that for the weight ratio of BPO/TBEC of 0.6/2.4, over 80% gel content of EVA was yielded after curing at 130°C for 12 min. Compared with the case of single curing agent, the present one obviously operated at much lower temperature with faster rate. By carefully studying the influence of curing agent proportion and curing conditions on gel content of EVA films, as well as rheology and curing kinetics, the mechanism involved was analyzed and verified. The results are believed to be useful for developing new curing system of EVA encapsulation films with improved processability.

Keywords: *industrial applications, ethylene vinyl acetate (EVA) films, curing, dual curing agent, properties*

1. Introduction

Silicon wafers in solar cells (also called photovoltaic (PV) modules) are generally embedded in encapsulation polymer films by either glass/glass or glass/plastic technology. The latter plays a vital role to bond different components. So far, the most common encapsulation material for PV modules is ethylene vinyl acetate (EVA) because of its balanced performance [1–3]. To provide high transparency, electrical insulation and mechanical stability for photovoltaic system, EVA films have to be cured during encapsulation [4], which has a direct impact on the production efficiency and products quality.

It is worth noting that curing of EVA is quite time-consuming. When dicumyl peroxide (DCP) acts as curing agent, the lamination process typically proceeds under vacuum and high pressure at 150–160°C for a while (>30 min) [5]. To accelerate curing of EVA films, efforts to develop advanced curing agent have been made. Butylperoxy 2-ethylhexyl carbonate (TBEC), for example, was found to be able to decrease the curing temperature and time to 145°C and 20–25 min, respectively [6]. In addition, benzoyl peroxide (BPO) was applied, which allowed for curing below 100°C. Nevertheless, the high exhaust rate of BPO caused damage to surface roughness and pre-curing would occur as decomposition temperature of BPO was close to the processing temperature.

Meanwhile, Beheshty *et al.* [7] studied curing of unsaturated polyester with acetyl acetone peroxide (AAP) solution as low temperature curing agent

---

*Corresponding author, e-mail: cesrwh@mail.sysu.edu.cn

and t-butyl perbenzoate (TBPB) as high temperature curing agent. The results showed that the curing temperature was reduced by 10°C and the curing speed was increased. Firstly, the low temperature curing agent was decomposed to initiate the curing, increasing local temperature of the polymer owing to the exotherm. Then, decomposition of the high temperature curing agent is triggered, which further increase the curing rate [8]. Xia and Cook [9] also used dual radical initiator system of two peroxides with different initiation rates to polymerize nona-ethylene glycol dimethacrylate. The maximum heat flow was reduced and polymerization process was spread over a broader range of temperature without affecting the degree of curing.

The above review suggests that dual curing agent rather than single curing agent would be more effective for accelerating curing of EVA films. In this context, we combine BPO and TBEC into one group. It is hoped that the BPO could induce crosslinking reaction of EVA at lower temperature, while TBEC takes effect at higher temperature as mentioned above. Hereinafter, the influences of compounding proportion and curing conditions on gel content of EVA films are investigated to verify our design. Kinetics and rheology of curing as well as optical property and storage performance of EVA films are also studied. The outcomes of this work will be helpful for industrial applications in practice.

2. Experimental section

2.1. Materials

Granulated EVA copolymer with 32% vinyl acetate (VA) content (EVA MA-10, melt flow index = 40 g/10 min, melting point = 65°C, density = 0.950 g/cm^3) was supplied by Polyolefin Company (Singapore) Pte, Ltd. The low temperature curing agent BPO was purchased from Shanghai Aladdin, China. The high temperature curing agent TBEC was bought from Shangyu Shaofeng Chemical Co., Ltd., China. The anti-ageing system of EVA encapsulation films was provided by cooperative enterprise [10]. Ultraviolet absorbent 329, antioxidant 1010 and light stabilizer 944 were also bought from Shangyu Shaofeng Chemical Co., Ltd., China.

2.2. Preparation of EVA films

EVA films containing BPO/TBEC were prepared as follows. EVA granules (45.0 g) and a certain portion of the additives were mixed by a HAAKE mixer (RC300p, HAAKE, Germany) at 70°C with a rotor speed of 50 r/min. Afterwards, the compounds were pressed into films 0.40 mm thick (with a 0.15 mm gas exhaust layer) by a laminator (CHTECH, CH-0205, China). For comparison, EVA films with single curing agent TBEC were fabricated under the same way.

The curing of EVA films took place in a RGFDY-002 solar cell laminator (Jinan Rui PV Machinery Co., Ltd., China) in vacuum. Effects of curing time and temperature were studied.

2.3. Characterization

Cured EVA films were extracted by xylene at 150°C for 24 h (ASTM D5492). After extraction, the samples were dried a vacuum at 80°C for 24 h. Gel content, *GC*, was calculated from Equation (1):

$$GC = \frac{W_1 - W_2}{W_1} \cdot 100\% \qquad (1)$$

where W_1 denotes the weight of EVA films before extraction, W_2 the weight of EVA films after extraction. To check stability of the curing performance, the EVA films containing curing agent were stored at 60°C for a month and then cured. Then, gel content was determined by the xylene extraction.

To monitor the curing process, EVA films with the curing agents were mixed in a HAAKE torque rheometer (RC300p, HAAKE, Germany) for 20 min at different temperatures (110, 120, 130 and 140°C) with a rotor speed of 30 r/min. Torque-time and temperature-time curves were recorded.

Kinetics study of curing of EVA films was carried out by differential scanning calorimeter (DSC) with TA instruments Q10 under nitrogen atmosphere at different heating rates (1, 3, 5, 7 and 9°C/min) from –50 to 250°C. The weights of all the specimens were approximately 3–5 mg.

A transmittance haze meter (WGT-S, Bogoo, China) was used to measure light-transmittance and haze values of cured EVA films according to the method of ASTM D 1003: 2007 [11].

The storage performance test is according to the following steps. After been stored at 60°C for a month, the EVA films were cured by a solar cell laminator (Jinan Rui PV Machinery Co., Ltd., RGFDY-002) in a vacuum. The gel contents (*GC*%) of EVA films were tested by xylene extraction.

3. Results and discussion

Crosslinked EVA chains are insoluble in hot xylene, while the non-crosslinked ones are dissolvable. On the basis of this principle, the gel content measurement not only reflects crosslinking degree of cured EVA films, but also can be used to optimize curing conditions. Figure 1 shows the dependence of gel content of cured EVA films on relative proportions of the dual curing agent. It is seen that under the curing temperature of 130°C, the gel content of the cured EVA films with BPO/TBEC ratio of 0.8/2.2 is about 85%. With a rise in the concentration of TBEC, the gel content gradually decreases. Similar trend also appears for the curing at 120°C. Since the gel content at BPO/TBEC ratio of 0.8/2.2 resembles that at 0.6/2.4, the latter value is chosen as the optimal one from the viewpoint of economic benefit considering that BPO is much cheaper than TBEC.

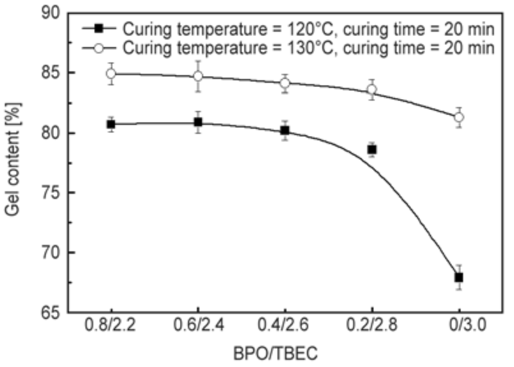

Figure 1. Gel contents of EVA films cured by BPO/TBEC at different temperatures as a function of BPO/TBEC weight ratio

Figure 2 further reveals the effect of curing time. The gel content of cured EVA films increases with increasing curing time as usual. The most interesting issue lies in the fact that for the curing temperature from 110 to 130°C, the gel content of the EVA films cured by BPO/TBEC is higher than that of the EVA films cured only by TBEC. When the curing temperature is raised to 140°C, the TBEC cured EVA films possess higher gel content. These phenomena imply that BPO serves as an accelerator for TBEC, which reduces both curing time and curing temperature of EVA system. Synergy between dual curing agent can be used to explain this phenomenon that the low temperature curing agent was decomposed to initiate the curing, increasing local temperature of the polymer owing to the exotherm. Then, decomposition of the high temperature curing agent is triggered, which further increase the curing rate [8]. Consequently, the gel content of the EVA films cured by the dual curing agent at 130°C is almost the same as that cured by TBEC alone at 140°C (cf. Figure 2c and 2d).

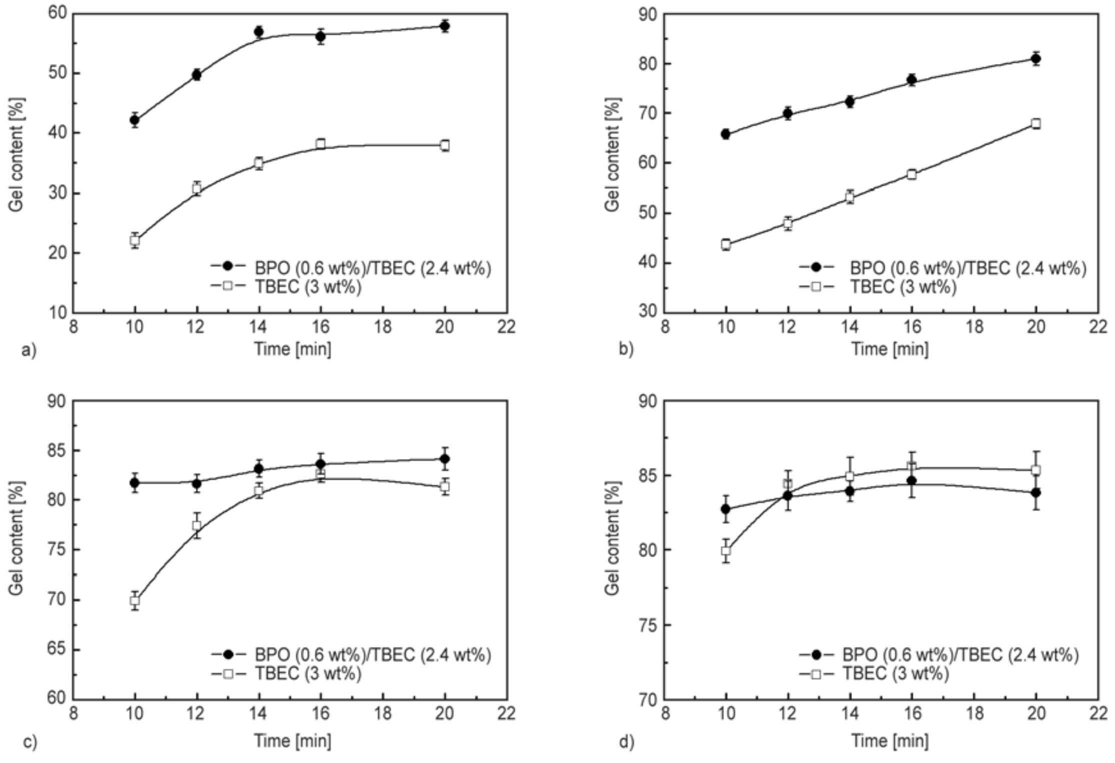

Figure 2. Gel contents of EVA films cured for different times. Curing temperature: (a) 110°C, (b) 120°C, (c) 130°C, and (d) 140°C

Since a gel content of 80% fits the requirements of practical usage, the optimum curing conditions can thus be determined: curing temperature = 130°C, curing time = 12 min, and BPO/TBEC = 0.6/2.4, which will be applied in the subsequent tests.

Crosslinked networks are built up in the course of curing, which must affect rheological behavior of the polymer. Examination of changes in torque as a function of time would in turn gives us some insight into the curing behavior. Figure 3 shows that following the feeding peak at the beginning, the torque of EVA increases with time due to viscosity increase originating from curing reaction. The torque reaches maximum when curing completes, and then decreases with further increasing time. Figure 3a exhibits that for the curing temperature of 110°C, the torque of EVA cured by BPO/TBEC increases more rapidly than that by TBEC. The curing time corresponding to the maximum torque, t_c [12, 13], of EVA with BPO/TBEC is 9.5 min, while that with TBEC is more than 20 min. In the case of higher curing temperature, the difference of rheological behavior between EVA with BPO/TBEC and EVA with TBEC declines, as characterized by the more and more smaller difference in t_c. Clearly, BPO takes effect in the dual curing agent system within a relatively wide temperature range. Even in the case of 140°C, its accelerating role is still perceived.

To investigate curing kinetics of the EVA system, DSC measurements were conducted. It can be observed from Figure 4 that there are several transitions during heating of EVA containing curing agents. Two exothermic peaks appear in the region of 40–80°C, one of which at about 50°C is attributed to a secondary crystallization, whereas the peak around 65–70°C is the thermo-dynamical melting point of the PE crystallites of EVA [14–16]. The curing of EVA occurs in the region of 100–180°C by the emergence of a double exothermic peak. For EVA with TBEC, enthalpy of the endothermic peak at 125°C is 0.48 J/g and that of the endothermic peak at 150°C is 15.9 J/g. The latter corresponds to the decomposition of TBEC. When the curing agent is replaced by BPO/TBEC, enthalpy of the endother-

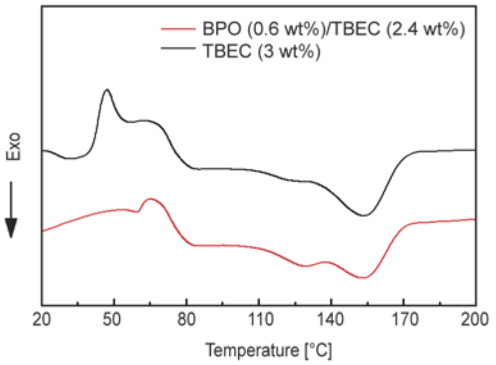

Figure 4. DSC heating curves of EVA with different curing agents recorded at a heating rate of 3 °C/min

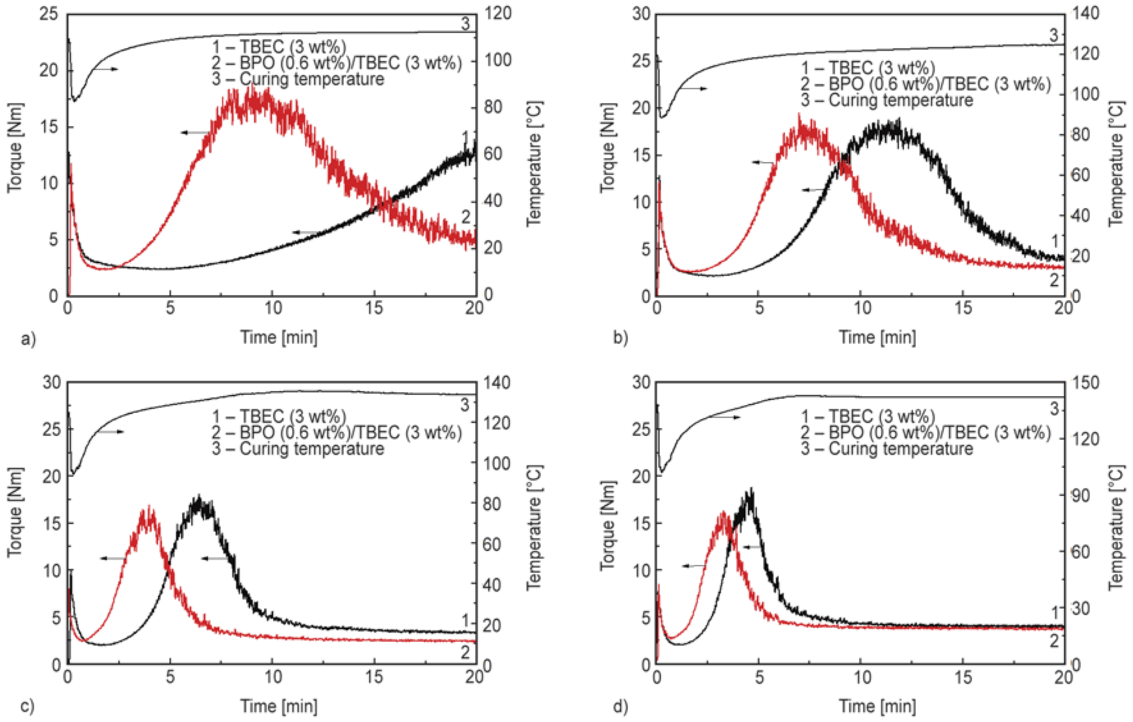

Figure 3. Torque versus time of EVA cured at different curing temperatures: a) 110°C, b) 120°C, c) 130°C, d) 140°C

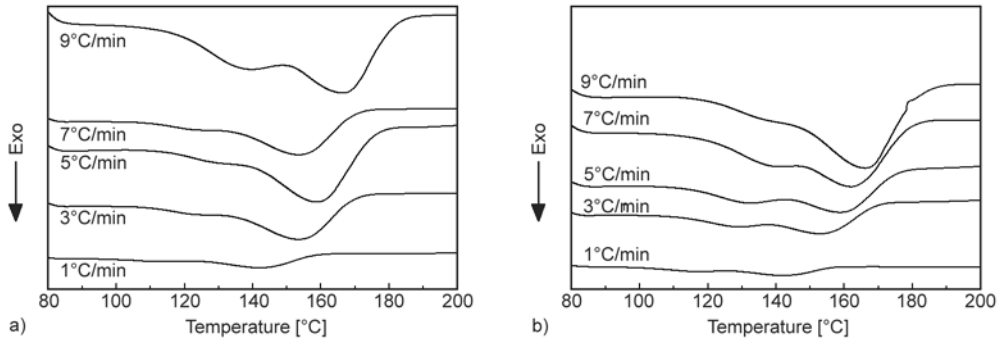

Figure 5. DSC heating curves of EVA containing (a) TEBC (3 wt%) and (b) BPO (0.6 wt%)/TEBC (2.4 wt%) recorded at different heating rates

Table 1. Curing kinetics characteristics of EVA films at different heating rates tested by DSC

	EVA film with TBEC (EVA:TBEC = 100:3)					**EVA film with BPO/TBEC (EVA:BPO:TBEC = 100:0.6:2.4)**				
β	**1**	**3**	**5**	**7**	**9**	**1**	**3**	**5**	**7**	**90**
T_i^* [K]	370.46	382.59	387.73	387.47	391.09	355.57	383.61	387.98	390.23	392.06
T_p [K]	416.19	427.67	433.26	436.55	440.45	414.98	426.61	433.75	436.19	439.65
T_f^* [K]	432.20	445.36	450.21	454.32	455.97	429.42	443.01	448.43	452.59	458.80

*T_i is the start temperature of curing and T_f is the end temperature of curing

mic peak at 125°C becomes 2.1 J/g. In combination with the above results of torque rheometer, a conclusion can be drawn that decomposition of BPO indeed initiates the curing of EVA at lower temperature and accelerates the curing of EVA as expected.

Further research on curing kinetics of EVA films was also carried out by DSC at different dynamic heating rate (Figure 5) and corresponding kinetics characteristics are listed in Table 1.

The activation energy used to reflect the curing rate can be calculated by classic Kissinger equation (Equation (2)) [17] according to the data in Table 1:

$$-\ln\frac{\beta}{T_p^2} = -\ln A + \frac{E_\alpha}{RT} \qquad (2)$$

R is the gas constant, T_p is the Kelvin temperature, A and E_α are material constants. The constant E_α, called the activation energy, is often interpreted as the energy barrier opposing the reaction. The constant A, most often called the frequency factor, is a measure of the probability that a molecule having energy E_α will participate in a reaction.

Plotted $-\ln\beta/T_p^2$ versus $1/T_p$ curve in Figure 6a give a straight line with a slope of $-E_\alpha/R$. Caculated E_α for EVA film with TBEC and EVA film with BPO/TBEC were listed in Table 2.

Table 2. Curing activation energies of EVA respectively cured by TBEC and BPO/TBEC

Content of curing agent	**Kissinger [J/mol]**	**Ozawa [J/mol]**
TBEC (3 wt%)	132.9	133.0
BPO (0.6 wt%)/TBEC (2.4 wt%)	123.2	123.7

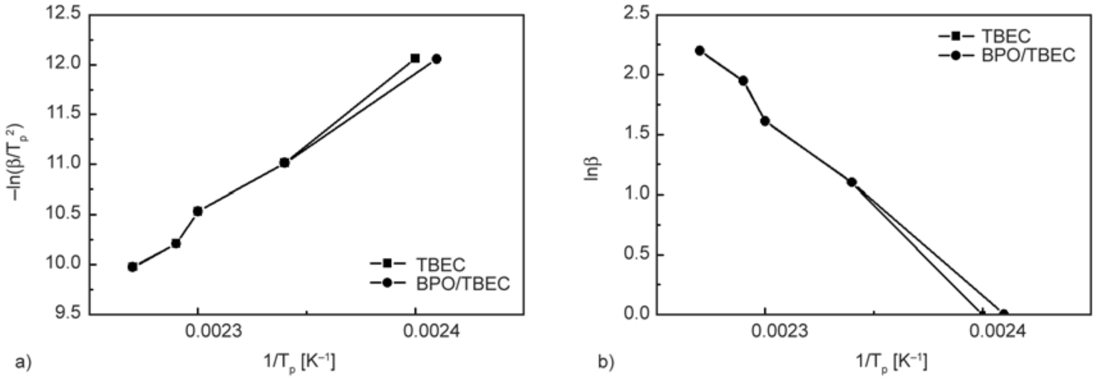

Figure 6. Corresponding data obtained from DSC caculation for EVA films: a) curves for Kissinger equation, b) curves for Ozawa equation

Table 3. Light-transmittance and haze values of EVA films cured with different curing agents

Content of curing agent	Light-transmittance [%]	Haze value [‰]
TBEC (3 wt%)	91.0 (±0.04)	0.33 (±0.006)
BPO (0.2 wt%)/TBEC (2.8 wt%)	90.9 (±0.06)	0.34 (±0.002)
BPO (0.4 wt%)/TBEC (2.6 wt%)	90.8 (±0.02)	0.36 (±0.004)
BPO (0.6 wt%)/TBEC (2.4 wt%)	90.8 (±0.02)	0.39 (±0.002)
BPO (0.8 wt%)/TBEC (2.2 wt%)	90.9 (±0.02)	0.38 (±0.002)
BPO (1 wt%)/TBEC (2 wt%)	90.8 (±0.04)	0.40 (±0.004)

For comparison, the activation energy was also calculated by Ozawa equation (Equation (3)) [18]. Corresponding lnβ versus $1/T$ curve was plotted in Figure 6b and calculated E_α were also listed in Table 2:

$$\log\beta = \log\frac{AE_\alpha}{g(\alpha)R} - 2.315 - \frac{0.4578E_\alpha}{RT_\mathrm{p}} \qquad (3)$$

As listed in Table 3, the curing activation energies of EVA estimated by the two methods are similar to each other. It means that the data have a high reliability. In the case of dual curing agent, the curing activation energy is 123.7 J/mol, which is lower than that of EVA cured by TBEC (133.0 J/mol) [19, 20]. It manifests that the curing reaction of EVA becomes easier so that it can be conducted at lower temperature. The accelerating effect of BPO is proved again.

Optical losses in a PV module consist of reflection losses and absorption losses of the encapsulations in the front [21, 22]. After curing, optical properties of EVA films might change. Table 3 shows light-transmittance and haze values of EVA films after curing. The light-transmittance of the EVA films cured by TBEC is 91.0% and the haze value is 0.33‰. It's fortunately to see that the two parameters of the EVA films with BPO/TBEC are close to those of EVA films without BPO. The addition of BPO particles does not affect optical property of EVA films owing to its decomposition during curing. This ensures application of the EVA films in practice.

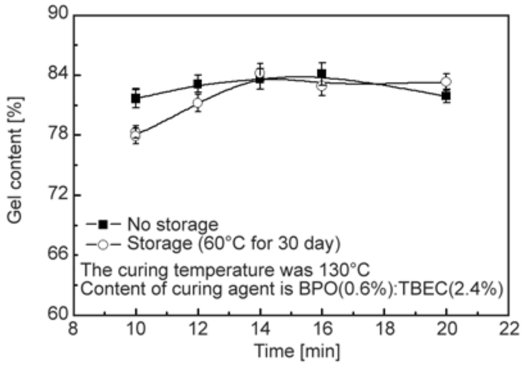

Figure 7. Gel contents of nonstored and stored EVA films cured at 130°C for different times

In general, EVA films have to be stored in warehouse for a period of time before packaging. During this period, temperature fluctuation might make the pre-compounded curing agents inactivate, especially when the low temperature curing agent is incorporated. (The self-accelerating decomposition temperature of BPO is 83°C and its half-life of 10 h is 72°C). Therefore, curing performance of the EVA films after storage should be checked. Figure 7 compares gel contents of the cured EVA before and after storage at 60°C. The two plots almost overlap each other. Basically, the gel contents are greater than 80% regardless of curing time. It is evident that the EVA films with BPO/TBEC have acquired sufficient stability for industrial applications.

4. Conclusions

The dual curing agent of BPO/TBEC proves to be able to significantly lower curing temperature and speed up curing process of EVA films as characterized by evolution of gel content and rheology behavior. Because decomposition of peroxide curing agent BPO under lower temperature initiates the curing of EVA and the exotherm further triggers decomposition of the high temperature curing agent TBEC, the curing activation energy of EVA is reduced. Meanwhile, the optical properties of cured EVA films meet the requirements for practical use with light-transmittances of ~91% and haze values of ~0.35‰. On the other hand, the addition of the dual curing agent does not affect storage stability of the EVA films. Crosslinking degree of the EVA films pre-stored at 60°C for one month is identical to that of the films without experiencing the storage.

Acknowledgements

The authors are grateful for the cooperation with Guangzhou Lushan New Materials Co., Ltd. and the support of the Science and Technology Department of Guangdong Province (Grants: 2011A091102003, 2011B090500004, 2011BZ100051, 2011BC100181), Natural Science Foundation of China (Grant: 51173207), and Key Project of Guangdong Education Office (Grant: cxzd1101).

References

[1] Pern F. J.: Ethylene-vinyl acetate (EVA) encapsulants for photovoltaic modules: Degradation and discoloration mechanisms and formulation modifications for improved photostability. Die Angewandte Makromolekulare Chemie, **252**, 195–216 (1997).
DOI: 10.1002/apmc.1997.052520114

[2] Pern F-J., Glick S. H.: Improved photostability of NREL-developed EVA pottant formulations for PV module encapsulation. in 'Proceedings of the 26th IEEE Photovoltaic Specialists Conference, Anaheim, USA' p9 (1997).

[3] Mei Z., Pern F. J., Glick S. H.: Modified EVA encapsulant formulations for low temperature processing. in 'NCPV Program Review Meeting, Lakewood, USA' p4 (2001).

[4] Czanderna A. W., Pern F. J.: Encapsulation of PV modules using ethylene vinyl acetate copolymer as a pottant: A critical review. Solar Energy Materials and Solar Cells, **43**, 101–181 (1995).
DOI: 10.1016/0927-0248(95)00150-6

[5] Ganesh B., Unnikrishnan G.: Cure characteristics, morphology, mechanical properties, and aging characteristics of silicone rubber/ethylene vinyl acetate blends. Journal of Applied Polymer Science, **99**, 1069–1082 (2006).
DOI: 10.1002/app.22621

[6] Kajari-Schröder S., Eitner U., Oprisoni C., Alshuth T., Köntges M., Brendel R.: Modelling the curing dynamics of ethylene-vinyl acetate. in 'Proceedings of the 25th European Photovoltaic Solar Energy Conference, Valencia, Spain' 4AV.3.25, p5 (2010).

[7] Beheshty M. H., Nasiri H., Vafayan M.: Gel time and exotherm behaviour studies of an unsaturated polyester resin initiated and promoted with dual systems. Iranian Polymer Journal, **14**, 990–999 (2005).

[8] Pern F. J., Czanderna A. W.: Characterization of ethylene vinyl acetate (EVA) encapsulant: Effects of thermal processing and weathering degradation on its discoloration. Solar Energy Materials and Solar Cells, **25**, 3–23 (1992).
DOI: 10.1016/0927-0248(92)90013-F

[9] Xia Z. W., Cook D. W.: Exotherm control in the thermal polymerization of nona-ethylene glycol dimethacrylate (NEGDM) using a dual radical initiator system. Polymer, **44**, 79–88 (2003).
DOI: 10.1016/S0032-3861(02)00766-8

[10] Yu P., Rong M. Z., Zhang M. Q., Xue H. Y., Ruan W. H.: A EVA (ethylene vinyl acetate) encapsulation film for photovoltaic modules and its preparation method. Chinese Patent, CN102604557 A, China (2003).

[11] ASTM D1003-07: Standard test method for haze and luminous transmittance of transparent plastics (2007).

[12] Bondan F., Soares M. R. F., Bianchi O.: Effect of dynamic cross-linking on phase morphology and dynamic mechanical properties of polyamide 12/ethylene vinyl acetate copolymer blends. Polymer Bulletin, in press (2013).
DOI: 10.1007/s00289-013-1051-8

[13] Kim S-J., Shin B-S., Hong J-L., Cho W-J., Ha C-S.: Reactive compatibilization of the PBT/EVA blend by maleic anhydride. Polymer, **42**, 4073–4080 (2001).
DOI: 10.1016/S0032-3861(00)00810-7

[14] Hirschl C., Biebl–Rydlo M., DeBiasio M., Mühleisen W., Neumaier L., Scherf W., Oreski G., Eder G., Chernev B., Schwab W., Kraf M.: Determining the degree of crosslinking of ethylene vinyl acetate photovoltaic module encapsulants – A comparative study. Solar Energy Materials and Solar Cells, **116**, 203–218 (2013).
DOI: 10.1016/j.solmat.2013.04.022

[15] Woo L., Ling M. T. K., Westphal S. P.: Dynamic mechanical studies on secondary relaxations of ethylene copolymers. Thermochimica Acta, **243**, 147–154 (1994).
DOI: 10.1016/0040-6031(94)85049-6

[16] Androsch R.: Melting and crystallization of poly(ethylene-*co*-octene) measured by modulated d.s.c. and temperature-resolved X-ray diffraction. Polymer, **40**, 2805–2812 (1999).
DOI: 10.1016/S0032-3861(98)00470-4

[17] Kissinger H. E.: Variation of peak temperature with heating rate in differential thermal analysis. Journal of Research of the National Bureau of Standards, **57**, 217–221 (1956).
DOI: 10.6028/jres.057.026

[18] Ozawa T.: A new method of analyzing thermogravimetric data. Bulletin of the Chemical Society of Japan, **38**, 1881–1886 (1965).
DOI: 10.1246/bcsj.38.1881

[19] Stark W., Jaunich M.: Investigation of ethylene/vinyl acetate copolymer (EVA) by thermal analysis DSC and DMA. Polymer Testing, **30**, 236–242 (2011).
DOI: 10.1016/j.polymertesting.2010.12.003

[20] Agroui K., Maallemi A., Boumaour M., Collins G., Salama M.: Thermal stability of slow and fast cure EVA encapsulant material for photovoltaic module manufacturing process. Solar Energy Materials and Solar Cells, **15**, 2509–2514 (2006).
DOI: 10.1016/j.solmat.2006.03.023

[21] Khoo Y. S., Walsh T. M., Lu F., Aberle A. G.: Method for quantifying optical parasitic absorptance loss of glass and encapsulant materials of silicon wafer based photovoltaic modules. Solar Energy Materials and Solar Cells, **102**, 153–158 (2012).
DOI: 10.1016/j.solmat.2012.03.008

[22] Lu Z. H., Yao Q.: Energy analysis of silicon solar cell modules based on an optical model for arbitrary layers. Solar Energy, **81**, 636–647 (2007).
DOI: 10.1016/j.solener.2006.08.014

eXPRESS Polymer Letters Vol.8, No.2 (2014) 123–132
Available online at www.expresspolymlett.com
DOI: 10.3144/expresspolymlett.2014.15

Preparation and characterization of novel thermoset polyimide and polyimide-peo doped with $LiCF_3SO_3$

M. H. Uğur, R. D. Toker, N. Kayaman-Apohan, A. Güngör[*]

Marmara University, Department of Chemistry, 34722 Istanbul, Turkey

Received 29 July 2013; accepted in revised form 14 October 2013

Abstract. This paper deals with the synthesis and characterization of a new type of anhydrous ionic conducting lithium doped membranes consist of polyimide (PI), poly (ethylene oxide) (PEO) and lithium trifluoromethanesulfonate ($LiCF_3SO_3$) for solid polymer electrolyte (SPE). For this purpose, different molar ratios of lithium salt (Li-salt) solution are added into poly (amic acid) (PAA) intermediate prepared from the reaction of 3,3′,4,4′-benzophenon tetracarboxylic dianhydride (BTDA) and 4,4′-oxydianiline (ODA). PEO is incorporated into PAA since it forms more stable complexes and possess high ionic conductivities. Then, Li-salt containing PAA solutions are imidized by thermal process. The effect of interaction between host polymer and Li-salt is characterized by FT-IR (Fourier Transform Infrared) spectroscopy and SEM (scanning electron micrsocopy). The conductivities of Li-salt and PEO containing PI composite membranes are in the range of 10^{-7}–10^{-5} S·cm^{-1}. The conductivity increases with incorporation of PEO. Thermogravimetric analysis results reveal that the PI/PEO/$LiCF_3SO_3$ composite polymer electrolyte membranes are thermally stable up to 500°C.

Keywords: *polymer composites, polymer membranes, ionic conductivity*

1. Introduction

Polyimides (PIs) belong to the important class of polymeric materials known as ‘high performance’ polymers due to their high thermo-oxidative stability [1], their exceptional mechanical properties, good film forming ability and superior chemical resistance [2–6]. Although, high performance polyimides are widely used in the microelectronics industry because the imide rings may provide permittivities equivalent to those of high dielectric constant to materials [7]. Work on polymer/salt mixtures has increased during recent years due to the growing interest in these systems as fast ion conducting systems. Several types of lithium ion conducting polymer electrolytes have been prepared as perfect homogenous mixtures of the components, namely, PEO as the polymer matrix which is capable of solving different alkali metal salts, and lithium trifluoromethanesulfonate ($LiCF_3SO_3$), lithium tetrafluoroborate ($LiBF_4$) and lithium perchlorate ($LiClO_4$) as a lithium salt [8]. However, these electrolytes show satisfactory ionic conductivity only at temperatures above 70°C. The conventional belief has been that the high degree of local order (‘crystallinity’) is what makes the ionic conductivity too low at ambient temperatures. Therefore, much attention has been devoted to the task of increasing the amorphous content of the PEO electrolyte; either by using large-anion lithium salts, by adding liquid plasticizers or ceramic fillers to the polymer [9–12]. When the electrolytic component is in the form of a dry polymer matrix, it consist of a high molecular weight homo or copolymer, which is cross-linkable or non-cross-linkable and includes a heteroatom in its repeating unit such as oxygen or nitrogen for example, in which an

---

[*]Corresponding author, e-mail: atillag@marmara.edu.tr

alkali metal salt is dissolved such as $LiCF_3SO_3$, $LiClO_4$, LiTFSI etc. In the literature, ion-conducting polyimide membranes are selected as promising candidates for separating the electrodes because such a membrane has the mechanical stability to prevent shorts on rough handling, the chemical stability to prevent decomposition reactions that organic liquid electrolytes are prone to suffer at elevated temperatures, and the ability to resist penetration of lithium dendrites [13]. In the literature, there are only a few studies similar to the work that has been carried out by several research groups [14–22]. For instance, U.S. Patent 5888672 issued to Gustafson and Antonucci [14] disclosure a battery wherein each of the anode, cathode and electrolyte layer is based upon soluble, amorphous and thermoplastic polyimide. In another study, Johnson *et al.* [15] explored to comprise a solid, thermoset polyimide matrix doped with a lithium salt (LiTFSI). Wensley prepared several optically clear polyimide based electrolytes and determined the minimum required amount of lithium per mole of imide ring in soluble polyimide for rechargeable batteries [16]. The aim of the present work is to investigate the effects of Li-salt and PEO on the ionic conductivity and morphological behavior of PI based polymer electrolyte.

2. Experimental

2.1. Materials

3,3′,4,4′-Benzophenone tetracarboxylic dianhydride (BTDA, Aldrich, Steinheim-Germany), 4,4′-Oxydianiline (ODA, Aldrich, Steinheim-Germany), Poly(ethylene oxide) (average $M_w = 100.000\ g\cdot mol^{-1}$, powder, Aldrich, Steinheim-Germany), Lithium trifluoromethanesulfonate ($LiCF_3SO_3$, 99.995%-Aldrich, Steinheim-Germany), Dimethylacetamide (DMAc, Aldrich, Steinheim-Germany) were dried under vacuum before being used and stored in home-designed glove box (Ercom Kompresör, Kartal/İstanbul, Turkey) until use.

2.2. Preparation of lithium salt containing polyimide membrane

ODA and DMAc were placed into a 100 mL three-neck flask under nitrogen purge. The mixture was stirred until the solution was clear. BTDA in equal molar amount to that of ODA was added to the solution and stirred for 24 h at room temperature to give a viscous, transparent and yellow solution of PAA (Figure 1) which afforded approximately 20% solid by weight. PAA solutions containing different amounts of $LiCF_3SO_3$ salt were converted to polyimide by thermal imidization technique heating one hour each at 80–100–150–200–250°C ranges applied onto glass plates (F1–F4) (Figure 2). Polyimides having long PEO moieties in the main chain (F5 and F6) have been prepared by heating overnight at relatively low temperatures to prevent the degradation of polyether chain (≈150°C).

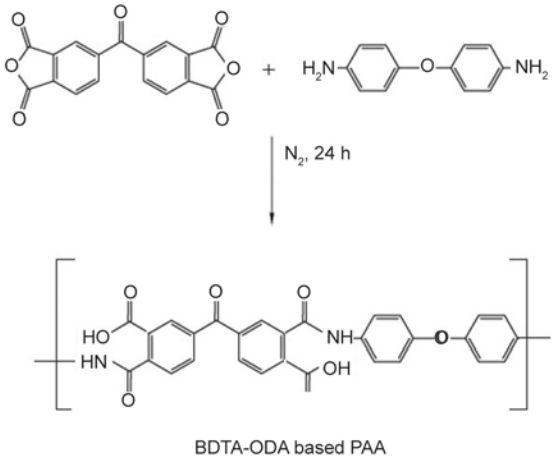

Figure 1. Shematic representation of synthesis BTDA-ODA based PAA

2.3. Characterization

FT-IR spectrum was recorded on Perkin Elmer Spectrum 100 ATR-FTIR spectrophotometer (Perkin Elmer, Waltham, MA, USA). SEM imaging of the films were performed on Philips XL30 ESEM-FEG/EDAX (Philips, Eindhoven, The Netherlands). The specimens were prepared for SEM by freeze fracturing in liquid nitrogen and applying a gold coating. The thermal stability of the samples was tested in the temperature range of 30–800°C by thermogravimetric analysis (TGA) using a PerkinElmer STA 6000 instrument (PerkinElmer, Waltham, MA, USA) under air atmosphere at a heating rate of 10°C/min. Differential scanning calorimetry (DSC) measurements were carried out with a Perkin Elmer Pyris Diamond (PerkinElmer, Shelton, CT, USA). The samples were analyzed under a nitrogen atmosphere in the temperature range –100 to 400ºC at a heating rate of 10ºC/min and cooling rate of 100ºC/min. Standard tensile stress-strain experiments were performed at room temperature on a Materials Testing Machine Z010/TN2S (Zwick GmbH&Co. KG, Ulm, Germany) using a crosshead speed of 5 $mm\cdot min^{-1}$. The mechanical properties of

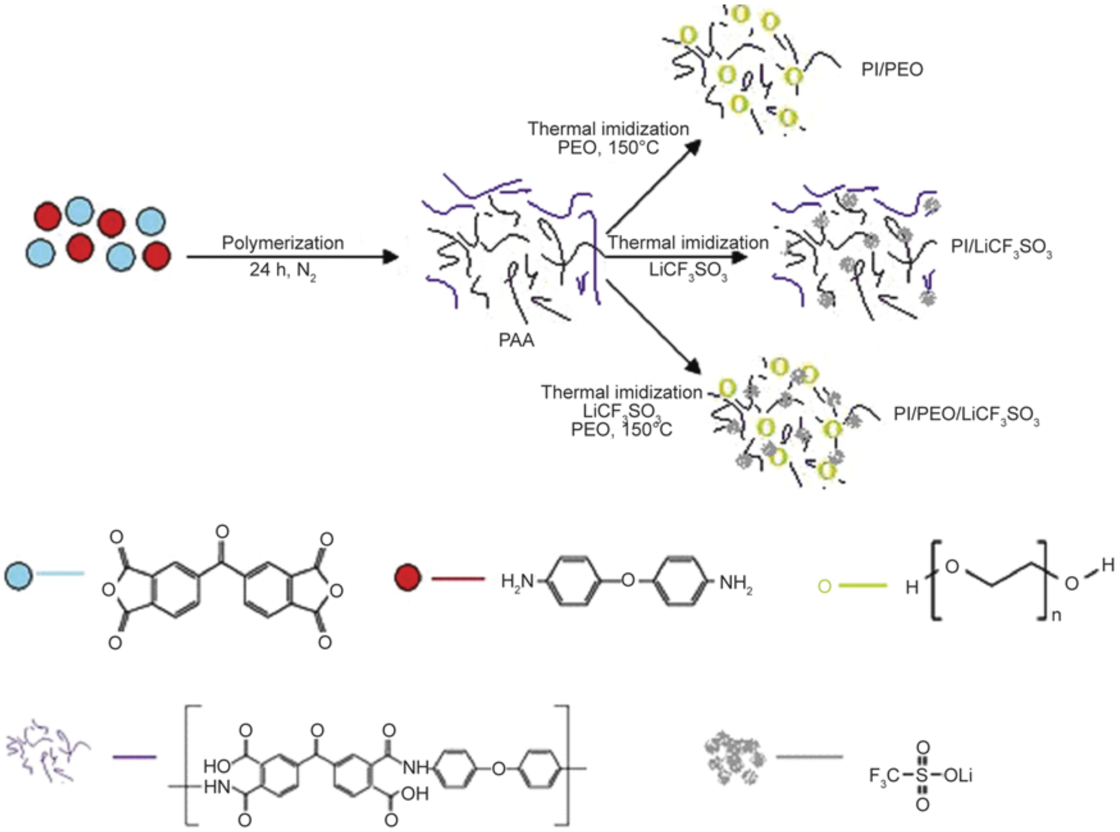

Figure 2. Shematic representation of preparation of Li-salt-doped polyimide membrane

the PI based polymer electrolytes were determined by standard tensile stress–strain tests in order to measure tensile strength and elongation at break. The specimen dimensions were 60.00 mm in length and 8.00 mm in width. Four parallel measurements were carried out for each sample.

Ionic conductivity measurements were recorded using a Gamry Potentiostat/Galvanostat/ZRA (Gamry Series G 750, Warminster, PA, USA) with Gamry Framework software system EIS300. EIS spectra were analyzed using Echem Analyst 5.67 software. The polymer electrolyte (PE) was placed between two SS (type 304, 0.025 mm thick, Alfa Aesar, Karlsruhe, Germany) electrodes in a cell. The thickness of the membrane was measured before and after the EIS measurement, to assure a constant thickness throughout the experiment. Ionic conductivity was measured under an argon atmosphere using a potantiostat/galvanostat and a home-design glove box with conductivity cell. The frequency ranged from 40 Hz to 100 mHz at a perturbation voltage of 5 mV. The ionic conductivity values of the polymer electrolyte systems are calculated from the intercept of real part of the complex impedance plot, which is resistance of the film and known area using the Equation (1) [19, 20]:

$$\sigma = \left(\frac{1}{R}\right)\cdot\left(\frac{L}{A}\right) \tag{1}$$

where σ is conductivity; L/A is geometrical factor, L is the thickness of the electrolyte film; R is resistance of the electrolyte film; and A is the area of the film.

Linear Sweep Voltammetry (LSV) measurement was recorded using a Gamry Potentiostat/Galvanostat/ZRA (Gamry Series G 750, Warminster, PA, USA) with Gamry Framework Software System PHE200 (Physical Electrochemistry Software, Warminster, PA, USA). LSV experiment was performed to investigate the electrochemical stability window of the polymer electrolyte (F5) employing SS as working electrode and lithium foil (Sigma-Aldrich, Steinheim-Germany) as reference and counter electrodes. Cell assembly was carried out in argon atmosphere inside the glove box. The scanning rate was 1 $\mathrm{mV\cdot s^{-1}}$ and the potential ranged from open circuit potential to 5.0 V (vs. $\mathrm{Li/Li^{+}}$).

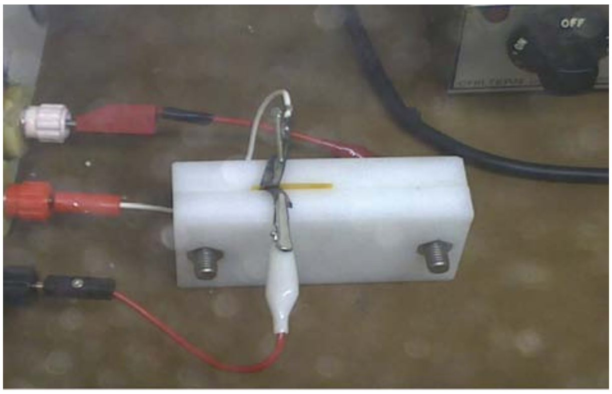

Figure 3. Picture of the conductivity cell

All the electrochemical experiments were carried out in an Argon atmosphere in a home-designed glove box at room temperature (Figure 3).

3. Results and discussions

3.1. FT-IR

The structures of membranes were investigated by FTIR. To evaluate the molecular interactions between PI and PEO, the FTIR spectrum of pure PEO was also displayed in the insert of Figure 4. Figure 4 shows the FTIR spectra of (a) membrane F0, (b) membrane F1, (c) membrane F5, (d) membrane F6 and (e) pure PEO. In all these work, the complexation is confirmed by the appearance of new peaks, frequency shifts, changes in intensities or shape of existing peaks in the FTIR spectra. The chemical bonding between PEO chain, $LiCF_3SO_3$, PEO-$LiCF_3SO_3$ and PI structure was discussed below.

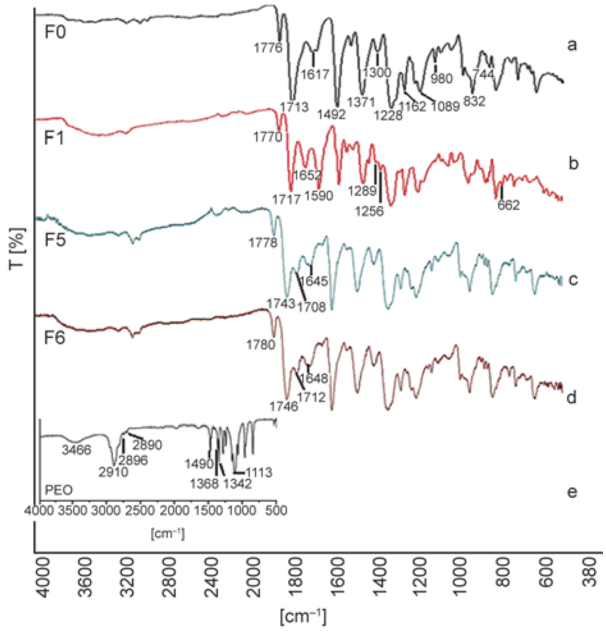

Figure 4. FT-IR spectra of a) PI and b) PI-$LiCF_3SO_3$ c) PI-PEO and d) PI-PEO-$LiCF_3SO_3$ e) pure PEO

The FT-IR spectroscopy indicated that complexation has occurred between polymer matrix and salt. Figure 4 curve a is FT-IR spectra for polyimide film without the addition of a Li salt or any solvent. The characteristic absorption bands of the imide groups near 1776 (asym. imide carbonyl stretching), 1713 (sym. imide carbonyl stretching) and 1371 cm^{-1} (imide C–N stretching) were observed in the FTIR spectrum after thermal imidization of the poly (amic acid). Meanwhile, the characteristic absorption of the amide carbonyl at 1640 cm^{-1} did not appear in the spectrum, indicating that the imidization reaction is complete. Strong bands in the range of 1300 cm^{-1} (imide C–N stretching) and 744 cm^{-1} (imide C–H bending) are also observed in the spectrum. Other absorption bands at 1617 and 1492 cm^{-1} are aromatic C=C stretching and benzene ring vibrations, respectively. Moreover, the spectra of membrane F0 show asymmetric stretching ether (C–O–C) bands at 1228, 1162 and 1089 and aromatic C–H bending bands between 980 to 832 cm^{-1} [23].

On the other hand, Figure 4 curve b shows FT-IR spectrum of PI-$LiCF_3SO_3$ membrane. The resulting polyimide electrolyte shows strong peaks at about 1652 and 1590 cm^{-1}. Previously it was reported that, polyimide electrolyte shows a very strong doublet at about 1670 and 1640 cm^{-1}. These peaks are the evidence for the complex between lithium salt and the imide rings of the polyimide [24]. Slight shifts observed in these peaks could be attributed to the use of different salts and different polyimide materials. Also it can be seen that, the characteristic polyimide peaks at 1776 and 1713 cm^{-1} are shifted to 1770 and 1717 cm^{-1}, respectively. The other bands at 1256 and 1289 cm^{-1} related sym. CF_3 stretching and asymm. SO_3 stretching modes. Also the complexation of the $LiCF_3SO_3$ salt with PI was confirmed by the presence of new peak at 662 cm^{-1} corresponding to free SO_3^- ion [25]. Furthermore it indicates an interaction/complexation between polyimide material and Li-salt. It is known that Li^+ is a very good complex forming species and therefore, it may possibly form some strong coordinate bond with the imide nitrogen atom or the imide carbonyl [26].

As can be seen in Figure 4 curve e, in the pure PEO spectrum a large broad band appears centered at

3466 cm^{-1}. Pure PEO shows a large, broad band of CH_2 stretching at 2910 cm^{-1}. However, the band is split into two at 2918 and 2884 cm^{-1} corresponding to asymmetric and symmetric CH_2 stretching, respectively [27]. Other bands at 1490, 1368–1342 and 1113 cm^{-1} are CH_2 scissoring, CH_2 wagging, C–O–C stretching modes [28, 29].

The existence of chemical interchain between PEO with PI was proved by FTIR study. As it can be seen in Figure 4 curves c and d, the band at 1743 and 1746 cm^{-1} corresponds to the esther carbonyl groups. The presence of ester bonds resulted in a shift of the peak of the imide carbonyl groups at around 1708 (curve c) and 1712 cm^{-1} (curve d). In these spectra, the peaks at 1645 and 1648 cm^{-1} were attributed to the amide carbonyl groups due to partially imidization of membranes F5 and F6 which were imidized at low temperatures.

3.2. Morphology properties of polyimide membranes

The morphologies of the PI, PI-PEO and their composite polyelectrolyte membranes were studied by scanning electron microscopy (SEM) as shown in Figure 5. As seen in Figure 5a, the fractured surface of the PI membrane is dense and homogeneous. Since the thermal imidization was performed by stepwise heating up to 250°C, microporosity was not observed on the membrane. However, the surface morphology of the Li salt containing membrane is rough compared with neat PI film as seen in the SEM image (Figure 5b). In Figure 5c the random distribution of PEO structure in PI matrix can be seen. Since the imidization was performed at low temperature to protect the polyether chain from thermal degradation, course voids appeared in the membrane due to the low rate of solvent evaporation. The characteristic semi crystalline morphology of PEO chain was undetectable in the PI-PEO membrane. When only PEO or $LiCF_3SO_3$ or PEO/$LiCF_3SO_3$ mixture was incorporated into PI matrix rough morphology was obtained (Figure 5b–5d).

3.3. Thermal and mechanical properties of polyimide based polymer electrolytes

Thermo-oxidative stabilities of the polymers were determined by thermogravimetric analysis in air. Figure 6 shows TGA thermograms of polyimides. The dynamic TGA experiments were run from 30 to 800°C, at a heating rate of 10°C/min under air atmosphere. The first stage of decomposition started at about 250°C due to the degradation of organic group of $LiCF_3SO_3$ salt (–CF_3–SO_3 bridge) and PEO (C–O–C), which were the weakest linkages along the main chain. The second stage of decomposition started from 450°C corresponding to the degrading of the aromatic imido groups; this is typical for aromatic polyimides in general [30]. In addition, although PEO decomposition temperature is much lower than polyimide, TGA curves of PEO containing polyimide membranes (F5–F6) have approximately same thermal properties. This result is

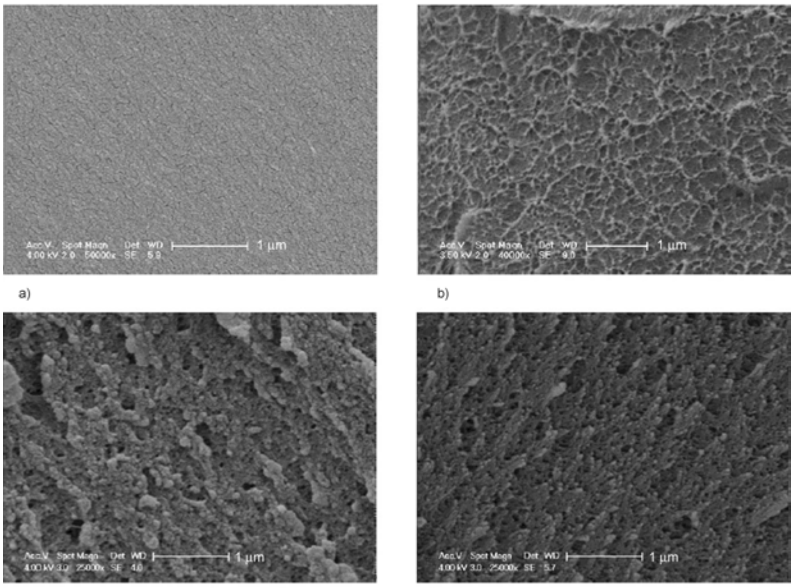

Figure 5. SEM cross-section images of a) PI (F0), b) PI-$LiCF_3SO_3$ (F1), c) PI-PEO-$LiCF_3SO_3$ (F5), d) PI-PEO (F6) and e) pure PEO

explained by seconder interaction between molecules and also incorporating very low concentrations of PEO.

The TG and derivative thermogravimetric analysis (DTG) curves of PI based membranes under air indicate three stages of thermal decomposition. However, the resulting curve, shown in Figure 6 stable up PI based electrolytes approximately not less than 50% of their mass, which was illustrated in all of the PI membranes, had excellent stability.

The glass transition temperature (T_g) of neat PI (F0) was found as 297.4 °C. When Li salt was added, the T_g of the composite film decreased to 271.6°C. Thus, it can be said that the Li salt particles decrease the chain interactions in the PI matrix by settling between polymer chains. On the other hand, in thermal imidization conditions (150°C for membranes F5 and F6) when PEO and the Li salt were incorporated into PI matrix, T_g was further reduced to 211.7°C. Partly remained solvent's effect is related to a weakening of the dipole-dipole interactions between the polymer chains. This result in a reduction of the T_g value. Therefore, this helps to soften the polymer backbone and increase its segmental motion. Relatively, this situation was attributed to the increased free volume at the molecular level due to presence of flexible PEO chains.

It is known that the mechanical properties of the SPEs are as important as the ionic conductivity at room temperature for their practical applications. Elongation at break and tensile strength of polymer electrolyte membranes are displayed in Table 2. For F1 to F4 membranes, decreasing Li content in the membrane decreases the elongation and tensile modules in the same manner. This behaviour was attributed decreasing the level of the hydrogen bond the carbonyl oxygen. When membranes F5 and F6 were compared, it is clearly observable that the addition of Li salt within the PEO containing PI membrane caused negligible changes. When membranes F2 and F5 were compared, it is clearly observable that the addition of PEO causes drastic reduction in the tensile strength and elongation at break. This could be attributed to the etheric structure of PEO. Finally, as can be seen in Table 2, raising the glass transition temperature of polymer electrolytes improves ionic conductivity but leads to a decrease in mechanical properties.

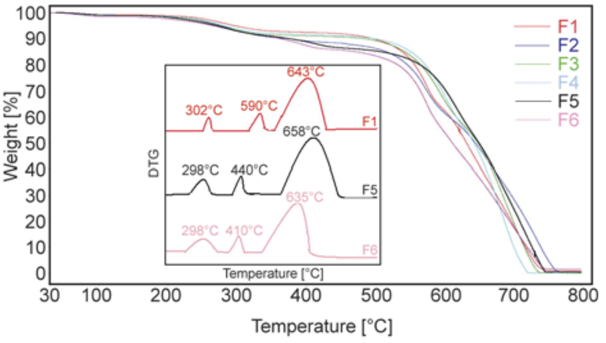

Figure 6. TGA thermograms of F1–F6 films recorded at a heating rate of 10°C/min for the polyimides containing various PEO, $LiCF_3SO_3$ and PEO-$LiCF_3SO_3$ contents. Inset Figure: The DTG curve shows stepwise decomposition of F1, F5 and F6 membranes.

3.4. Ionic conductivity

The ionic conductivity of a polymer electrolyte depends on the concentration of ion carriers and on their mobility. The ionic conductivity in polymer electrolytes is assumed to occur by Lewis acid-base interactions between the cations and the polymer solvent. It is also generally accepted that the ionic conduction occurs mainly in the amorphous component of polymer electrolytes above their T_g with the chain segment mobility playing a critical role in the conductivity mechanism [31].

In the case of solvent free polymer electrolytes, the motions of the polymer host are responsible for the ionic mobility; ions move only if polymer segments undergo fairly large-amplitude motions [32–34] related to T_g. Polymer electrolytes show fast ionic conduction above their T_g where they are largely comprised of amorphous phases. Thus, a low T_g polymer like PEO (poly (ethylene oxide)); T_g, –50 to –57°C [35] has become an important polymer for solvent free electrolytes, and amorphization of this polymer is being researched [36, 37] as a way to increase its ionic conductivity.

In this study, the conductivity of the polymer electrolyte membranes was calculated from the measured resistance of the film for the known area and thickness of the polymer film. Table 1 and Figure 7 summarize the compositions and Nyquist diagrams of the thermoset PI based polymer electrolytes. Firstly, the ionic conductivity was studied as a function of Li salt concentration within PI matrix (F1–F4). As can be seen in Table 1, the Li^+ ion conductivity changed according to [O]/[Li] ratio where [O] is the number of mole of oxygen atoms in polyimide structure from membrane F1 to membrane

Table 1. The conditions, Li^+ ion conductivity values and [O]/[Li] ratios of membranes

	F1	F2	F3	F4	F5	F6
Metod	**Thermal imidization**	**Thermal imidization**	**Thermal imidization**	**Thermal imidization**	**Thermal imidization**	**Thermal imidization**
Process temperature [°C]	**80–100–150–200–250**	**80–100–150–200–250**	**80–100–150–200–250**	**80–100–150–200–250**	**80–100–150**	**80–100–150**
Codes	$PI/LiCF_3SO_3$	$PI/LiCF_3SO_3$	$PI/LiCF_3SO_3$	$PI/LiCF_3SO_3$	$PI/PEO/LiCF_3SO_3$	PI/PEO
*[O]/[Li] ratio	1:1	2:1	4:1	8:1	1:1	–
PEO [mole]	–	–	–	–	10^{-6}	10^{-6}
Iomic conductivity [$S\cdot cm^{-1}$]	$9.2\cdot10^{-7}$	$1.08\cdot10^{-6}$	$4.44\cdot10^{-6}$	$8.7\cdot10^{-6}$	$2.04\cdot10^{-5}$	–

*[O] mole number of oxygen atoms is polyimide structure

Table 2. Thermal and mechanical properties of novel PI based thermoset polymer electrolytes

Sample code	Tensile strength [N/mm^2]	Elongation at break [%]	Max weight loss temperature [°C]	The glass transition temperature [°C]
F0	130.80	5.40	668	297.4
F1	64.53	1.07	643	271.6
F2	33.52	0.84	660	231.3
F3	17.80	0.60	659	220.8
F4	16.64	0.42	650	213.2
F5	16.80	0.41	658	211.7
F6	17.68	0.40	635	205.8

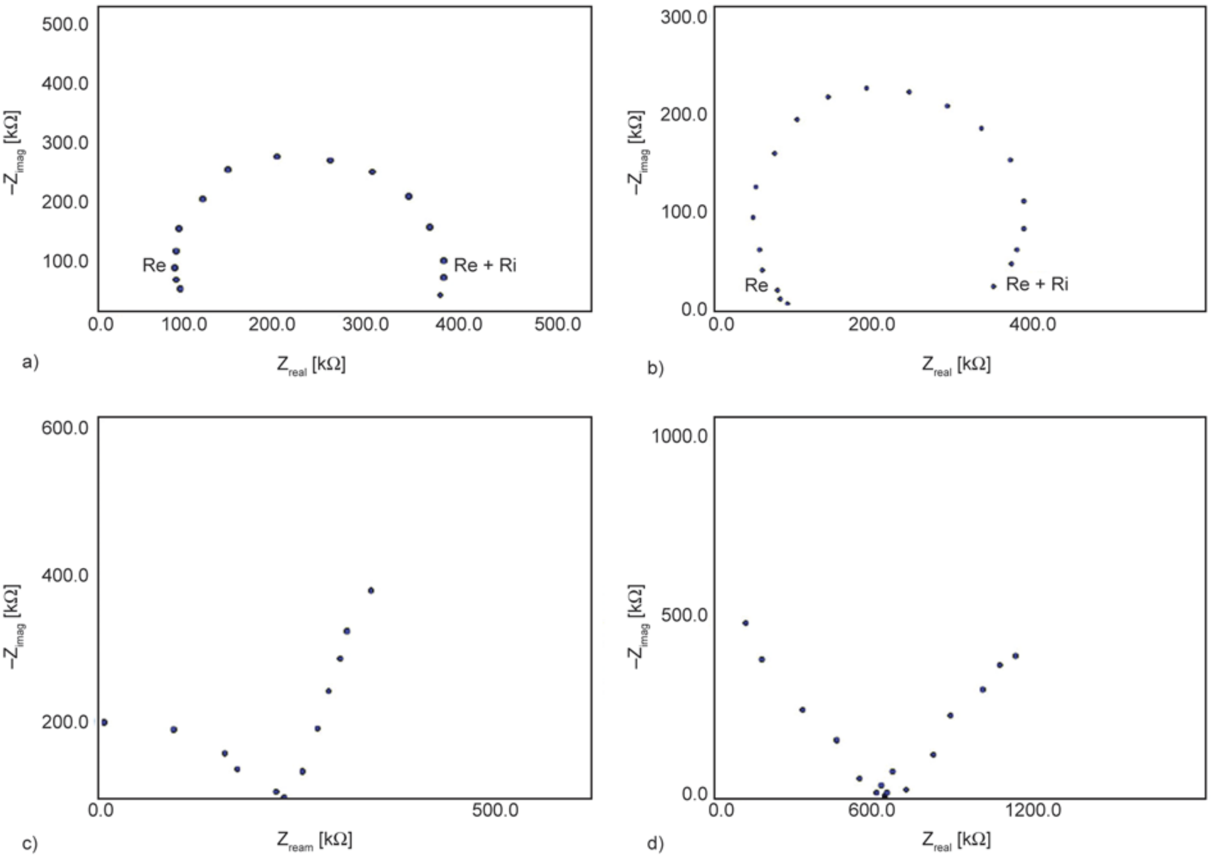

Figure 7. Impedance diagrams of ion-conductive polyimide membranes a) $PI/PEO/LiCF_3SO_3$ (F5) b) $PI/LiCF_3SO_3$ (F4) c) $PI/LiCF_3SO_3$ (F3) d) $PI/LiCF_3SO_3$ (F2)

F4. At lower [O]/[Li] ratio, ion conductivity significantly decreased. This can be explained by the increased amount of Li^+ ion concentration in thermoset polyimide materials which was limited the mobility of polymer chains [24]. In other words, further increase of Li ion concentration results in reduction of conductivity, explained by an increase in transient ionic crosslinks within polymer network, causing a decrease in chain segment mobility. It has also been suggested that at high salt content formation of ion aggregates will contribute to a decrease in conductivity [38]. Hence, membrane F4 showed highest ionic conductivity of $8.7\cdot10^{-6}$ S·cm^{-1} compared the other membranes (F1, F2 and F3) at room temperature.

On the other hand, the polymer–salt complexes are formed by complexes between salts of alkali metals and polymer containing solvating heteroatoms such as O, N, S, etc. The most common examples are complexation between PEO and alkali metal salts [39]. The ether oxygens in PEO are hard Lewis bases, thus they have low polarizability and high electronegativity. They coordinate well to hard Lewis acids, which in general are small cations, e.g., Li^{+1}, Na^{+1} and Mg^{+2}. These cations then, in turn, form salts with low lattice energies together with large, e.g., PF_6^-, $CF_3SO_3^-$ and $(CF_3SO_3)_2N^-$. These larger anions can sometimes also have a plasticizing effect on the polymer [40]. In addition, the increase in amorphous content is probably due to the large $CF_3SO_3^-$ anion that reduces the crystallinity of the complex. It can be suggested the increase in conductivity in our system is due to the amorphizing properties of the large $CF_3SO_3^-$ ion present in the system. The spectroscopically 'free' ions are believed to be responsible for ionic charge transport in polymer electrolyte. They can be temporarily complexed or attached to the polymer chain (Li^+ can attach to oxygen atoms on PEO) during segmental motion of the polymer and then hop to the next site. The fraction of 'free' ions will indicate the effectiveness of various electrolyte components in increasing charge concentration and subsequent ion conduction [41]. Thus, the increasing ionic conductivity of PI-PEO-$LiCF_3SO_3$ film suggested that, even a small amount of PEO added to PI-$LiCF_3SO_3$ membrane, increases the free volume and decreases the T_g which leads to increase molecular mobility. Hence this will cause to increase conductivity. In the PI-PEO-$LiCF_3SO_3$ electrolyte system (F5) the composition with the highest conductivity is recorded which reaches $2.04\cdot10^{-5}$ S·cm^{-1} at room temperature.

3.5. Linear sweep voltammetry (LSV)

Electrochemical measurements showed that the cells prepared from using a stainless steel (SS) electrode, a lithium counter, and a lithium reference electrodes had a wide range electrochemical stability. Thus, the high stability of the PI based electrolyte membrane (F5) may be attributed to the absence of impurities, which is a welcome feature because it permits their use in high-voltage battery applications. Figure 8 shows the current-voltage response of the solid polymer membrane obtained in the potential range between open circuit and 5.0 V vs. Li at room temperature. As it can be seen, the plateau is very flat and straight; this very low residual current level prior to breakdown voltage, with no peaks in the 2.0–3.5 V voltage range. So, it confirms the high purity of the SPE membrane was obtained. In addition, the onset of the current during anodic scan, which is representative of the decomposition of the electrolyte, indicates an anodic break-down voltage of approximately 4.3 V vs. Li. So, membrane F5 showed an appreciable anodic breakdown voltage [42].

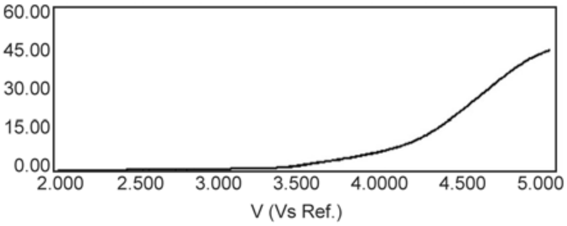

Figure 8. Electrochemical stability window at room temperature for PI based polymer electrolyte (F5), potential scan rate: 1 mV·s^{-1}

4. Conclusions

Novel PI-based composite polymer electrolytes were prepared by the incorporation of $LiCF_3SO_3$ and PEO. Characterizations were carried out by FTIR, TGA, DSC, mechanical properties, SEM, impedance measurements and LSV. The thermal imidization technique was adopted to prepare polymer electrolyte membranes. BTDA and ODA based polyimide synthesized by step-growth polymerization method. In order to improve the conductivity behaviour of membranes, we have been focused on introducing the PEO and $LiCF_3SO_3$ into the polymer backbone. FT-IR measurements showed the existence of the complex formation between lithium salt and imide ring of the polyimide. F1 and F5 films showed an ionic conductivity of $9.2 \cdot 10^{-7}$ and $2.04 \cdot 10^{-5}$ S·cm^{-1} respectively at room temperature which is acceptable value for lithium rechargeable batteries. However, this conductivity is still low for practical use in lithium-polymer or lithium-metal batteries. The final solid polymer electrolyte is not soluble in the liquid electrolyte and also stable over a wide range of temperatures.

Acknowledgements

This work was supported by Marmara University, Commission of Scientific Research Project under grant Project FEN-E-090113-0006.

References

[1] Critchley J. P., Knight G. J., Wright W. W.: Heat-resistant polymers: Technologically useful materials. Plenum Press, New York (1983).

[2] Mittal K. L.: Polyimides: Synthesis, characterization and applications. Plenum Press, New York (1984).

[3] Bessonov M. T., Koton M. M., Kudryavtsev V. V., Laius L. A.: Polyimides: Thermally stable polymers. Consultants Bureau, New York (1987).

[4] Wilson D., Stenzenberger H. D., Hergenrother P. M.: Polyimides. Blackie, Glasgow (1990).

[5] Ghosh M. K., Mittal K. L.: Polyimides: Fundamentals and applications. Marcel Dekker, New York (1996).

[6] Yamanaka K., Jikei M., Kakimoto M-A.: Preparation and properties of hyperbranched aromatic polyimides via polyamic acid methyl ester precursors. Macromolecules, **33**, 6937–6944 (2000).
DOI: 10.1021/ma000725n

[7] Negi Y. S., Suzuki Y-I., Kawamura I., Hagiwara T., Takahashi Y., Iijima M., Kakimoto M-A., Imai Y.: Synthesis and properties of polyimides based on 2,2-bis[4-(4-aminophenoxy)phenyl]propane and 2,2-bis[4-(4-aminophenoxy)phenyl]hexafluoropropane. Journal of Polymer Science Part A: Polymer Chemistry, **30**, 2281–2284 (1992).
DOI: 10.1002/pola.1992.080301026

[8] Vallee A., Brouilette D., Pugh J. K., Guindy W. W. J.: Polyimide-based lithium metal battery. U.S. Patent 7824808 B2, USA (2010).

[9] Benrabah D., Sanchez J-Y., Armand M.: Synthesis and electrochemical characterization of a new family of lithium salts. Solid State Ionics, **60**, 87–92 (1993).
DOI: 10.1016/0167-2738(93)90279-C

[10] Silva M. M., Barros S. C., Smith M. J., MacCallum J. R.: Study of novel lithium salt-based, plasticized polymer electrolytes. Journal of Power Sources, **111**, 52–57 (2002).
DOI: 10.1016/S0378-7753(02)00229-X

[11] Croce F., Appetecchi G. B., Persi L., Scrosati B.: Nanocomposite polymer electrolytes for lithium batteries. Nature, **394**, 456–458 (1998).
DOI: 10.1038/28818

[12] Reiche A., Weinkauf A., Sander B., Rittig F., Fleischer G.: Alternating copolymers for novel polymer electrolytes: The electrochemical properties. Electrochimica Acta, **45**, 1327–1334 (2000).
DOI: 10.1016/S0013-4686(99)00340-0

[13] Meyer W. H.: Polymer electrolytes for lithium-ion batteries. Advanced Materials, **10**, 439–448 (1998).
DOI: 10.1002/(SICI)1521-4095(199804)10:6<439::AID-ADMA439>3.0.CO;2-I

[14] Gustafson S., Antonucci J. T.: Polyimid battery. U.S. Patent 5888672 A, USA (1999).

[15] Johnson L. G., Allie L. A., Muller J. R.: Solid, lithium-salt-doped, thermoset polyimide polymer electrolyte and electrochemical cell employing same. U.S. Patent 20130011745, USA (2013).

[16] Wensley C. G., Vallée A., Brouillette D., Gustafson S.: Polyimide matrix electrolyte. U.S. Patent 7198870 B2, USA (2007).

[17] Tigelaar D. M., Palker A. E., Meador M. A. B., Bennett W. R.: Synthesis and compatibility of ionic liquid containing rod-coil polyimide gel electrolytes with lithium metal electrodes. Journal of the Electrochemical Society, **155**, 768–774 (2008).
DOI: 10.1149/1.2967723

[18] Pak Y. S., Xu G.: Ionic transport measurements of $LiCF_3SO_3$ doped polyimide-diaminobenzenesulfonic acid copolymer. Solid State Ionics, **67**, 165–169 (1993).
DOI: 10.1016/0167-2738(93)90322-T

[19] Tian S. B., Pak Y. S., Xu G.: Polyimide-polysiloxane-segmented copolymers as high-temperature polymer electrolytes. Journal of Polymer Science Part B: Polymer Physics, **32**, 2019–2023 (1994).
DOI: 10.1002/polb.1994.090321208

[20] Park J-H., Kim J-S., Shim E-G., Park K-W., Hong Y. T., Lee Y-S., Lee S-Y.: Polyimide gel polymer electrolyte-nanoencapsulated $LiCoO_2$ cathode materials for high-voltage Li-ion batteries. Electrochemistry Communications, **12**, 1099–1102 (2010).
DOI: 10.1016/j.elecom.2010.05.038

[21] Gustafson S., Wensley C. G.: Polyimide matrix electrolyte. U.S. Patent 20040229127, USA (2004).

[22] Wensley C. G., Gustafson S., Nelson C. R., Singleton R. W., Vallee A., Brouillette D.: Polyimide matrix electrolyte and improved batteries therefrom. U.S. Patent 7129005, USA (2006).

[23] Davenas J., Xu X. L., Boiteux G. Sage D.: Relation between structure and electronic properties of ion irradiated polymers. Nuclear Instruments and Methods in Physics Research Section B: Beam Interactions with Materials and Atoms, **39**, 754–763 (1989).
DOI: 10.1016/0168-583X(89)90891-4

[24] Wensley C. G., Vallee A., Brouillette D., Gustafson S.: Polyimide matrix electrolyte. U.S. Patent 7198870 B2, USA (2007).

[25] de Zea Bermudez V., Alcácer L., Acosta J. L., Morales E.: Synthesis and characterization of novel urethane cross-linked ormolytes for solid-state lithium batteries. Solid State Ionics, **116**, 197–209 (1999).
DOI: 10.1016/S0167-2738(98)00346-4

[26] Cotton F. A., Wilkinson G.: Advanced inorganic chemistry. Wiley, New York (1988).

[27] Ramesh S., Yuen T. F., Shen C. J.: Conductivity and FTIR studies on PEO–LiX [X: $CF_3SO_3^-$, SO_4^{2-}] polymer electrolytes. Spectrochimica Acta Part A: Molecular and Biomolecular Spectroscopy, **69**, 670–675 (2008).
DOI: 10.1016/j.saa.2007.05.029

[28] Rocco A. M., da Fonseca C. P., Pereira R. B.: A polymeric solid electrolyte based on a binary blend of poly (ethylene oxide), poly(methyl vinyl ether-maleic acid) and $LiClO_4$. Polymer, **43**, 3601–3609 (2002).
DOI: 10.1016/S0032-3861(02)00173-8

[29] Tang Z., Wang J., Chen Q., He W., Shen C., Mao X-X., Zhang J.: A novel PEO-based composite polymer electrolyte with absorptive glass mat for Li-ion batteries. Electrochimica Acta, **52**, 6638–6643 (2007).
DOI: 10.1016/j.electacta.2007.04.062

[30] Dhara M. G., Banerjee S.: Fluorinated high-performance polymers: Poly(arylene ether)s and aromatic polyimides containing trifluoromethyl groups. Progress in Polymer Science, **35**, 1022–1077 (2010).
DOI: 10.1016/j.progpolymsci.2010.04.003

[31] Berthier C., Gorecki W., Minier M., Armand M. B., Chabagno J. M., Rigaud P.: Microscopic investigation of ionic conductivity in alkali metal salts-poly(ethylene oxide) adducts. Solid State Ionics, **11**, 91–95 (1983).
DOI: 10.1016/0167-2738(83)90068-1

[32] Wakihara M.: Recent developments in lithium ion batteries. Materials Science and Engineering R: Reports, **33**, 109–134 (2001).
DOI: 10.1016/S0927-796X(01)00030-4

[33] Ratner M. A., Shriver D. F.: Ion transport in solvent-free polymers. Chemical Reviews, **88**, 109–124 (1988).
DOI: 10.1021/cr00083a006

[34] Papke B. L., Ratner M. A., Shriver D. F.: Conformation and ion-transport models for the structure and ionic conductivity in complexes of polyethers with alkali metal salts. Journal of the Electrochemical Society, **129**, 1694–1701 (1982).
DOI: 10.1149/1.2124252

[35] Brandup J., Immergut E. H., Grulke E. A., Abe A., Bloch D. R.: Polymer handbook. Wiley, New York (1999).

[36] Le Nest J. F., Callens S., Gandini A., Armand M.: A new polymer network for ionic conduction. Electrochimica Acta, **37**, 1585–1588 (1992).
DOI: 10.1016/0013-4686(92)80116-4

[37] Nishimoto A., Watanabe M., Ikeda Y., Kohjiya S.: High ionic conductivity of new polymer electrolytes based on high molecular weight polyether comb polymers. Electrochimica Acta, **43**, 1177–1184 (1998).
DOI: 10.1016/S0013-4686(97)10017-2

[38] Angell C. A., Xu K., Zhang S-S., Videa M.: Variations on the salt-polymer electrolyte theme for flexible solid electrolytes. Solid State Ionics, **86**, 17–28 (1996).
DOI: 10.1016/0167-2738(96)00088-4

[39] Chandrasekhar V.: Polymer solid electrolytes: Synthesis and structure. Advances in Polymer Science, **135**, 139–205 (1998).
DOI: 10.1007/3-540-69191-X_2

[40] Armand M., Gorecki W., Andreani R.: Perfluorosulphonimide salts as solute for polymer electrolytes. in ‘Second International Symposium on Polymer Electrolytes’ (ed.: Scrosati B.) Elsevier, London, 91–97 (1990).

[41] Tang C., Hackenberg K., Fu Q., Ajayan P. M., Ardebili H.: High ion conducting polymer nanocomposite electrolytes using hybrid nanofillers. Nano Letters, **12**, 1152–1156 (2012).
DOI: 10.1021/nl202692y

[42] Appetecchi G. B., Croce F., Dautzenberg G., Mastragostino M., Ronci F., Scrosati B., Soavi F., Zanelli A., Alessandrini F., Prosini P. P.: Composite polymer electrolytes with improved lithium metal electrode interfacial properties I. Elechtrochemical Properties of Dry PEO-LiX. Journal of the Electrochemical Society, **145**, 4126–4132 (1998).
DOI: 10.1149/1.1838925

eXPRESS Polymer Letters Vol.8, No.2 (2014) 133–141
Available online at www.expresspolymlett.com
DOI: 10.3144/expresspolymlett.2014.16

Effect of a new surface-grafting method for nano-hydroxyapatite on the dispersion and the mechanical enhancement for poly(lactide-*co*-glycolide)

L. X. Jiang[1,2,3], *L. Y. Jiang*[1*], *L. J. Xu*[1,2], *C. T. Han*[1,2], *C. D. Xiong*[1]

[1]Chengdu Institute of Organic Chemistry, Chinese Academy of Sciences, 610041 Chengdu, PR China
[2]Graduated School of Chinese Academy of Sciences, 100039 Beijing, PR China
[3]Shenzhen Institute of Advanced Technology, Chinese Academy of Sciences, 518067 Shenzhen, PR China

Received 19 August 2013; accepted in revised form 14 October 2013

Abstract. In this paper, a new surface-grafting D, L-lactide (DLLA) for nano-hydroxyapatite (n-HA) with the assist of citric acid was designed. The dispersion of new surface modified n-HA was characterized by Fourier transformation infrared (FTIR) spectroscopy, thermal gravimetric analysis (TGA), X-ray powder diffraction (XRD), transmission electron microscopy (TEM) and dispersion test, and the mechanical enhancement effect for poly(lactide-*co*-glycolide) (PLGA) was evaluated by scanning electron microscopy (SEM), differential scanning calorimeter measurements (DSC) and electromechanical universal tester. The results showed that citric acid played a critical role in surface-grafting, which could greatly increase grafting amount and improve dispersion of n-HA, so that it resulted in better interfacial adhesion throughout PLGA matrix, higher crystallinity and better mechanical enhancement for PLGA than the surface-grafting method for n-HA without citric acid, whose bending strength and tensile strength were both over 20% higher than those of pure PLGA when 3 wt% n-HA was added, and it still enhanced 8 and 6% higher than those of pure PLGA even the introduction of 15 wt% n-HA, respectively. The above results suggested that the surface-grafting for n-HA with the aid of citric acid was an ideal novel surface modification method, which could greatly improve the dispersion of n-HA and exhibit excellent mechanical enhancement effect for PLGA, suggesting it has a great potential in the bone fracture internal fixation application in future.

Keywords: *polymer composites, nanocomposites, nano-hydoxyapatite, surface modification, mechanical properties*

1. Introduction

Poly (lactic acid-*co*-glycolic acid) (PLGA) has been widely studied as bone fracture internal fixation materials [1]. However, the relatively poor mechanical property is insufficient to apply in dense bone, and the lack of bioactivity is unfavorable to bone fracture healing quickly [2, 3]. While nano-hydroxyapatite (n-HA) is similar to the inorganic component of natural bone, which not only has good biocompatibility and osteo-conductivity, but also has good mechanical enhancement effect for polymer as nanoparticles [4, 5]. Therefore, extensive efforts have been devoted to the research of introducing n-HA to PLGA, which is expected to enhance its mechanical property and improve its bioactivity [6–8].

However, the incorporation of unmodified n-HA would decrease mechanical property of PLGA, due to the agglomeration of the n-HA in the PLGA matrix and the lack of adhesion between the n-HA particles and the PLGA matrix [9], which might limit the application of PLGA as bone fracture internal fixation materials. So surface-modification for n-HA is a vey key technique. Consequently, various surface modifications for n-HA have been developed, such as silane coupling agents, zirconyl salt, polyacids, isocyanate, dodecyl alcohol and lac-

---

[*]Corresponding author, e-mail: jlytxg@163.com

tide (LA) [10–14]. Among the above surface modification for n-HA, grafting ring-opening polymerization of LA onto the surface of n-HA particles is a very effective way to improve the interfacial affinity of n-HA to the PLGA matrix. However, when n-HA is directly treated by LA, the grafting amount is still low because of the poor reactivity of the hydroxyl groups on the surface of n-HA and the bad dispersion of n-HA in hydrophobic solvent. Accordingly, the mechanical enhancement effect for PLGA isn't ideal when higher n-HA content was added into PLGA [15]. However, generally speaking, the higher addition content of n-HA, the better osteological bioactivity of PLGA [16]. Therefore, new surface-grafting methods for n-HA should be explored so as to have both better mechanical enhancement effect and higher n-HA addition content for PLGA.

In our previous study, we have investigated some surface-grafting methods for n-HA. For example, we found that the surface modification method of combining stearic acid with surface-grafting L-lactide was an effective modification method for n-HA, where stearic acid could improve the dispersion of n-HA during surface-grafting L-lactide, so the addition of 3 wt% n-HA into PLGA had the best mechanical enhancement for PLGA, while the addition of 15 wt% n-HA decreased markedly its bending strength [17, 18]. Subsequently, we designed another surface-grafting method of combining silane coupling reagent (KH550) with surface-grafting L-lactide (L-LA), where KH550 not only could improve the hydrophobicity of n-HA acting as coupling agent but also could provide amino group to graft-polymerize with L-lactide onto the n-HA surface, so the mechanical enhancement effect was far more excellent than corresponding unmodified n-HA, however, the maximum addition content of n-HA into PLGA was only 10 wt% [19].

Based on the above results, to further improve the dispersion of n-HA and the mechanical enhancement for PLGA by the addition of higher n-HA content, a new surface-grafting method with the assistance of citric acid was reported in this paper, where molecular structure of citric acid has three carboxyl groups and one hydroxyl group, and the steric hindrance of citric acid is conducive to improve the dispersion of n-HA, so it is expected to improve grafting amount for n-HA by forming a Ca carboxylate bond with citric acid, and D, L-lactide could be ring-opening graft-polymerized onto the n-HA surface by the hydroxyl group of citric acid, based on the literature [20]. Moreover, the new surface-grafted n-HA was introduced into PLGA matrix with different contents of 3, 8, 15 and 25wt% to investigate the mechanical enhancement effect for PLGA, comparing with the surface-grafted n-HA without citric acid. The main aim of the study is to provide an ideal novel surface modification method for n-HA, so that it could improve the dispersion of n-HA and mechanical enhancement effect for PLGA, and it would have a great potential in the bone fracture internal fixation application in future.

2. Materials and methods

2.1. Materials

n-HA was prepared in our laboratory, whose average size of nanoparticles was about 100–120 nm in length and 20–40 nm in width. PLGA, whose copolymer composition (LA:GA) is 95:05 (mol:mol), $M_w = 3.6\cdot10^5$-$3.9\cdot10^5$, was also prepared in our laboratory. Citric acid, AR, purchased from chemical reagent factory, Kelong, Chengdu. D, L-lactide (DLLA, Purac company) was recrystallized from ethyl acetate under argon atmosphere. Stannous octanoate was obtained from Sigma Company. All other reagents were of the analytical grade.

2.2. Surface modification of n-HA with the assist of citric acid

10 g citric acid in DMF was added into 10 g n-HA suspended in DMF with stirring. The reaction was maintained at 150°C for 11 h under nitrogen. The powder product was washed by ethanol and vacuum-dried, and 8 g n-HA product powder of surface-modified by citric acid was uniformly dispersed in dimethylbenzene by ultrasonic treatment. Then 8 g DLLA and 0.004 g $Sn(Oct)_2$ were added under nitrogen. The mixture was maintained at 140°C for 20 h under nitrogen. After it was washed with excessive dichloromethane and vacuum-dried, the obtained product powder was named as g1-n-HA. The n-HA of surface-grafted without citric acid was prepared in the same procedure as the control, which was named as g2-n-HA.

2.3. Characteristics of surface-modified n-HA

The IR analysis of unmodified n-HA and two surface-grafted n-HA powders were performed using Fourier transform infrared spectroscopy (Thermo Nicolet 670, USA) in KBr disks.

The amount of grafted organic materials were determined by TGA (Perkin-Elmer 7 series thermal analysis system) at a heating rate of 10°C/min from room temperature to 700°C under a high-purity nitrogen atmosphere.

X-ray diffraction analysis were carried out by XRD powder diffractometer (Philips, X' Pert Pro, Cu K_α). A scan axis of 2θ was used to obtain diffraction patterns of a scan range from 15 to 70°. The voltage used was 40 kV and the current was 45 mA.

TEM (JME-100CX, Seike Instruments) investigations were taken on a 200 kV acceleration voltage. The specimens were prepared by dripping a drop of 0.1% suspension onto a TEM grid covered with carbon film and evaporated the solvent completely at room temperature.

The dispersion test was valued by the colloid stability according to the intuitive photographs taken by a conventional camera at different time. The powder was dispersed in dicholomathane (1.0 g/L).

2.4. Preparation of g-n-HA/PLGA composites

The pure PLGA was dissolved in dichloromethane, and pre-calculated two surface-grafted n-HA uniformly dispersed in ethanol and dichloromethane were slowly added into PLGA solution by the addition of 3, 8, 15 and 25 wt%, respectively. Then the mixtures were stirred with ultrasonic treatment for more than 4 h. The precipitates were washed with excessive ethanol and dried under vacuum at 40°C for 48 h.

2.5. Properties of g-n-HA/PLGA composites

Fracture surfaces of PLGA after different addition contents of two surface-grafted were observed by SEM (S-520, Hitachi, Japan) after gold coating, which was used to investigate the dispersion of the g-n-HA nanoparticles in PLGA matrix and the interface microstructure.

The thermal properties of PLGA after different addition contents of two surface-grafted were measured by DSC (Q20, TA instruments, USA) at a heating rate of 10°C/min from room temperature to 190°C with flowing nitrogen gas, holding at 190°C for 5 min to erase thermal history, then cooled to 40°C with 10°C/min cooling rate, finally heated to 190°C with 10°C/min rate again, and the second heat curve was analyzed. The crystallinity (X_c) was calculated according to Equation (1):

$$X_c = \frac{\Delta H_m}{\omega \cdot \Delta H_{m,100\%}} \tag{1}$$

where ΔH_m indicates the melting enthalpy, and ω is the weight fraction of PLGA in the composite. $\Delta H_{m,100\%}$ is the theoretical enthalpy (93.7 J/g) of completely crystalline poly(L-lactic acid) (PLLA) [21].

The mechanical enhancement effect for PLGA after different addition contents of two surface-grafted were measured by an electromechanical universal testing machine (CMT6000, Sans, China). According to GB/T1042-92, the three-point bending strength of rectangular bars of 4 mm×6 mm×60 mm were measured at a crosshead speed of 20 mm/min, and the tensile strength of specimens with dimensions of 50 mm×6 mm×0.5 mm were measured at a speed of 1 mm/min, at 22°C and a relative humidity of 60%. The average value of five measurements was given.

3. Results and discussion

3.1. Characterization of surface modification reactions for n-HA

3.1.1. IR analysis

Figure 1 gives the FTIR spectra of unmodified n-HA and surface-modified n-HA. Some of the main absorption peaks of PO_4^{3-}, –OH groups and H_2O were identified for n-HA (shown in Figure 1 curve a). In addition, the split peaks at 1420.0 and 1465.6 cm^{-1} belonging to CO_3^{2-} asymmetric stretch peak are also observed, which was resulted from the minor CO_3^{2-} inclusion during the n-HA synthesis. These results are in accordance with those of n-HA in literature [22]. After surface modification, besides these bands, for g2-n-HA exhibits bands of the carbonyl groups at 1737.5 cm^{-1}, and some small peaks observed between 3000 and 2850 cm^{-1} are assigned

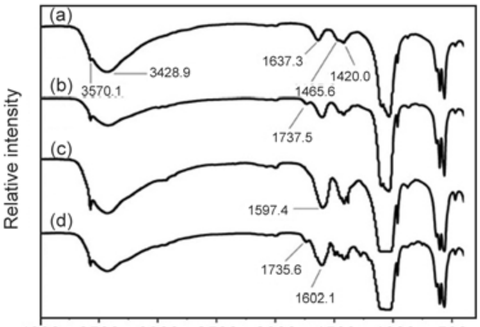

Figure 1. IR spectra of (a) unmodified n-HA, (b) g2-n-HA, (c) n-HA of citric acid modified, (d) g1-n-HA

to C–H stretching vibration of the CH_3- and CH-groups (shown in Figure 1 curve b), suggesting that ester bonds originated from the polymerization of DLLA on the n-HA surface existed. For the n-HA modified by citric acid (shown in Figure 1 curve c), small peaks of C–H stretching vibration emerges and the peak of COO^- at 1597.4 cm^{-1} is observed, implying that calcium carboxylate on the surface of n-HA was formed. While g1-n-HA exhibits a new absorption peak at 1602.1 cm^{-1} belonging to carbonyl groups of PLA, besides for the carbonyl groups at 1735.6 cm^{-1} (shown in Figure 1 curve d). According to the above analysis, we concluded that citric acid and PLA were both successfully grafted onto the surface of n-HA.

3.1.2. TGA

The amount of grafted organic substances is determined by TGA, as shown in Figure 2. According to the TGA curves, the weight losses of unmodified n-HA, n-HA of citric acid modified and two g-n-HA are 4.703, 8.06%, 12.86 and 6.303%, respectively. The surface-grafted amount onto n-HA is calculated as follows by the equation, the grafting amounts [%] = W_1 [%] – W_0 [%], where W_1 is the weight loss of surface-grafted n-HA and W_0 is the weight loss of unmodified n-HA. Therefore, the total grafting amounts onto n-HA of citric acid, g1-n-HA and g2-n-HA are 3.357, 8.157 and 1.600%, respectively, and the grafting amounts of PLA onto g1-n-HA and g2-n-HA are 4.800 (8.157%–3.357%) and 1.600%, respectively. Obviously, it is further proved that n-HA surface was successful grafted quantitatively. Moreover, the grafting amount of g1-n-HA is larger than that of g2-n-HA, which shows that citric acid played an important role in increasing grafting amounts of PLA onto n-HA, and the reason may be attributed to the higher reactivity of the hydroxyl groups of citric acid and the better dispersion of n-HA due to the steric hindrance of citric acid during the processing of grafting with D, L-lactide, comparing with n-HA directly grafted with D, L-lactide without citric acid. The higher grafting amounts onto n-HA would be benefit to improve the dispersion of n-HA and interface adhesion with PLGA matrix when it was added into PLGA [23].

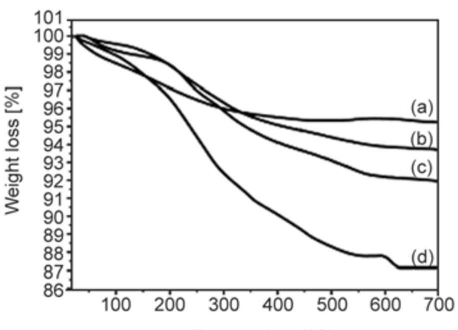

Figure 2. TGA curves of (a) unmodified n-HA, (b) g2-n-HA, (c) n-HA of citric acid modified, (d) g1-n-HA

3.1.3. XRD

Figure 3 gives the XRD patterns of unmodified n-HA and two g-n-HA. The unmodified n-HA exhibits characteristic peaks at 2θ regions of 26, 32-34, 40, and 46–54°, which is consistent with the crystalline nature of n-HA in literature [24]. Comparing the XRD patterns of g-n-HA with unmodified n-HA, it can be found that the characteristic diffractions of two g-n-HA nanocrystals are nearly the same as those of unmodified n-HA, which shows that there are no other new apatite crystalline phases, namely, the surface modifications didn't significantly affect the crystalline phases of n-HA. However, it is easy to find that the intensity of characteristic crystalline peaks of 2θ at 26° becomes a little weaker after being modified, and the crystalline peaks of g1-n-HA is weaker than that of g2-n-HA, whose crystallinity of unmodified n-HA, g1-n-HA and g2-n-HA calculated with XRD analysis software Jade are 80.81, 72.00 and 80.53%, respectively. The difference of crystallinity is attributed to the covering of the organic substances grafted on n-HA, and the larger the grafting amount is, the lower the crystallinity of n-HA is, which is in agreement with the results of TGA.

Based on these, the surface-grafting reaction with citric acid for n-HA are assumed as shown in Figure 4. First, Ca on the surface of n-HA reacted with car-

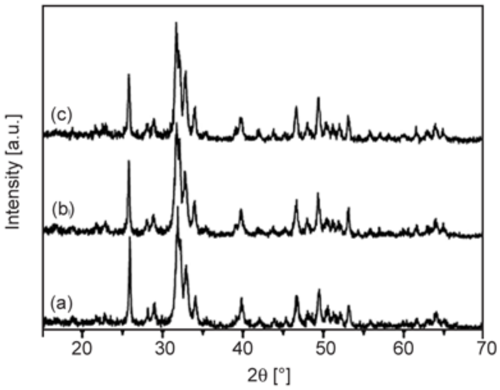

Figure 3. XRD patterns of (a) unmodified n-HA, (b) g2-n-HA, (c) g1-n-HA

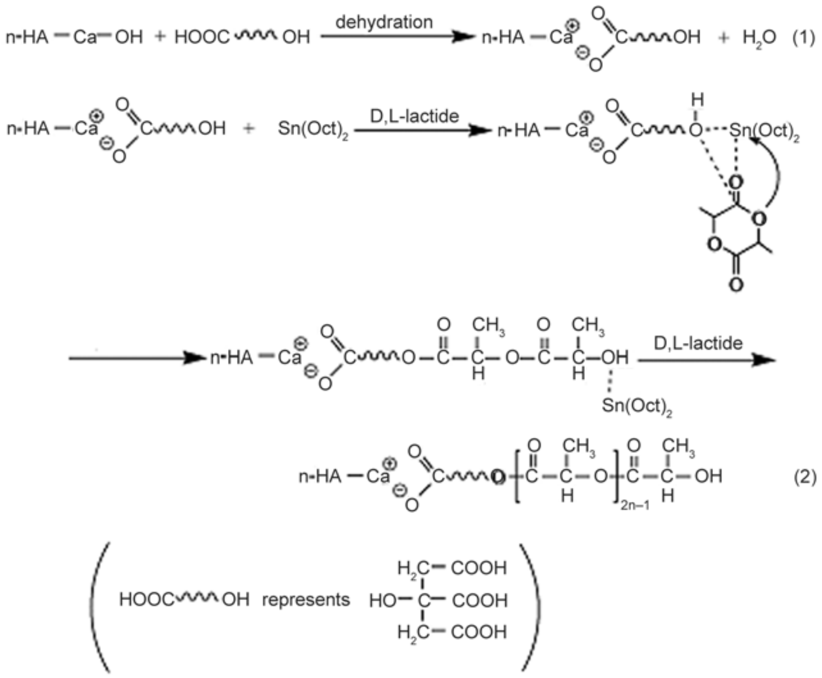

Figure 4. Illustration of the surface grafting with citric acid for n-HA

boxylate of citric acid to form a Ca Carboxylate bond (Step (1)). Then the propagation reaction in the presence of $Sn(Oct)_2$ included in succession the coordination of both the lactide and the hydroxyl group of calcium citric acid on the surface of HA modified by citric acid with $Sn(Oct)_2$ followed by cleavage of the acyl-oxygen bond of the D, L-lactide by the Sn-coordinate insertion mechanism and thereby activated hydroxyl group as indicated in (Step (2)) [20].

3.1.4. TEM

TEM photographs of unmodified n-HA and two g-n-HA are shown in Figure 5. It can be seen that they are all needles, indicating that the morphology of g-n-HA nanoparticles did not change after being surface-modified. However, unmodified n-HA nanoparticles exhibit aggregation phenomenon in dichloromethane (seen in Figure 5a), while the dispersion of two g-n-HA are obviously improved after being surface-modified, as shown in Figure 5b and 5c. Especially, g1-n-HA has better dispersibility than g2-n-HA, which may be resulted from its higher grafting amount.

3.1.5. Dispersion test

To further investigate the dispersion effect of surface modification for n-HA, the three different samples were dispersed in dichloromethane, and the intuitive photographs taken by a conventional camera are given in Figure 6. As expected, unmodified n-HA particles precipitated in hydrophobic organic solution immediately after ultrasonication. However, after n-HA particles was coated by PLA chains, the surface wettability was greatly improved, so that the two g-n-HA could maintain a stable dispersion in suspension for a longer time. Especially, g1-n-HA exhibits more excellent colloid stability, which can remain stable for one day, while a little precipitate appears in the suspension of g2-n-HA. Obviously, the dispersion of g-n-HA is closely related

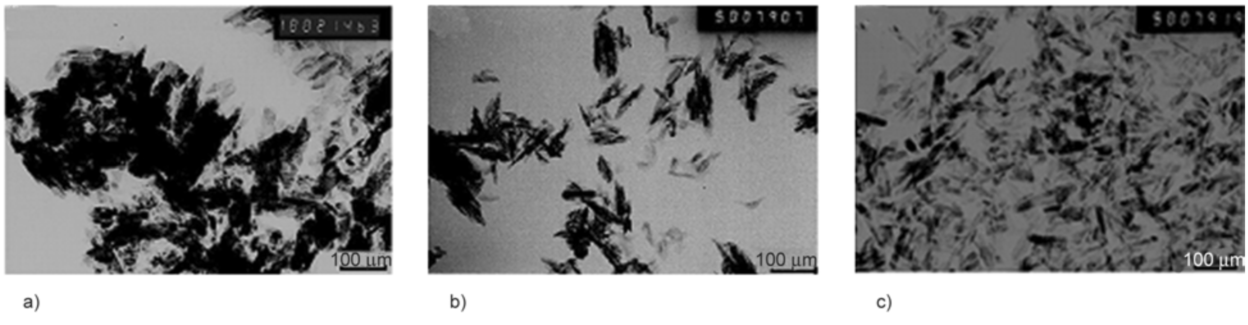

Figure 5. TEM photographs of (a) unmodified n-HA, (b) g2-n-HA, (c) g1-n-HA

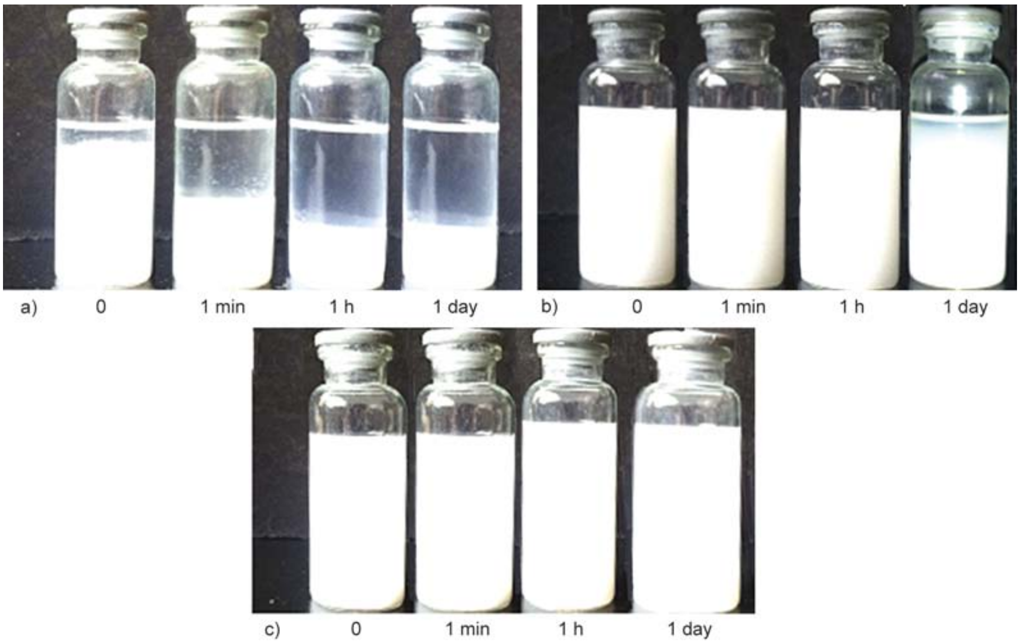

Figure 6. Photographs of (a) unmodified n-HA, (b) g2-n-HA, (c) g1-n-HA dispersed in dichloromethane for different time

to the grafting amount on the surface of n-HA. This result shows that the novel method of surface-grafted with the assistance of citric acid for n-HA could change the surface wettability and prevent the aggregation of n-HA particles is more efficient than the method of the directly surface-grafted LA without citric acid for n-HA, and the dispersibility is better than some literature [25], which may be more useful to enhance mechanical properties for PLGA.

3.2. Properties of g-n-HA/PLGA composites

3.2.1. SEM observation

To investigate the dispersion of g-n-HA particles in PLGA matrix and the interfacial adhesion, the SEM analysis has been performed. The SEM micrographs are given in Figure 7. For g2-n-HA/PLGA composite, there are many cavities between g2-n-HA particles and PLGA matrix, and many agglomerated g2-n-HA particles emerge when the g2-n-HA content is up to 8 wt%, indicating that there was poor dispersion and interfacial adhesion. However, for the g1-n-HA/PLGA composite, there are few cavities and agglomerated particles until the g1-n-HA content increased to 25 wt%. Obviously, it can be concluded that the g1-n-HA dispersed much more uniformly in PLGA matrix than g2-n-HA, so surface-grafted with the assistance of citric acid for n-HA is a novel surface-grafting method to improve

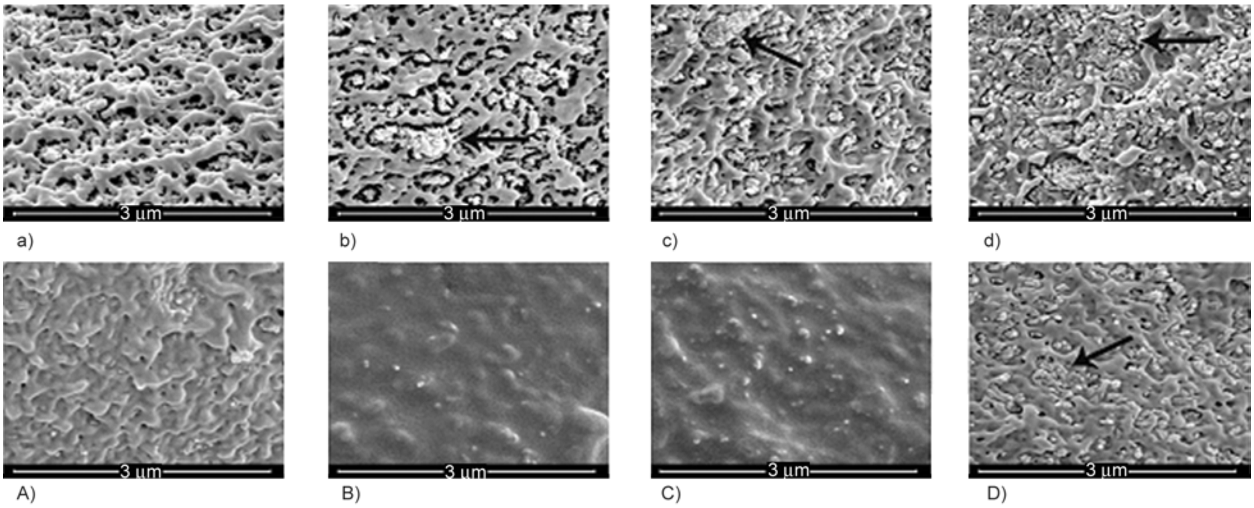

Figure 7. SEM micrographs of different g-n-HA addition content of g2-n-HA at (a) 3 wt%, (b) 8 wt%, (c) 15 wt%, (d) 25 wt% and g1-n-HA (A) 3 wt%, (B) 8 wt%, (C) 15 wt%, (D) 25 wt%. The arrows show the agglomerate g-n-HA particles in PLGA matrix

the dispersion of nanoparticles in PLGA matrix and the interfacial adhesion, which has a close relationship with the mechanical enhancement effect for PLGA [26].

3.2.2. Thermal properties

To further investigate the thermal properties, the DSC curves of PLGA after the different addition of two g-n-HA are shown in Figure 8, and the thermal properties data calculated from DSC curves are listed in Table 1. It can be found that the melting temperature (T_m) seems to have no relationship with the loading of g-n-HA particles, while the crystallinity of PLGA matrix increased with the increasing g-n-HA content. What is more, the crystallinity of PLGA after the addition of g1-n-HA is higher than that of corresponding addition of g2-n-HA, which indicates the g1-n-HA acts as a more effective heterogeneous nucleating agent than g2-n-HA. The reason is that the better dispersion of g1-n-HA in PLGA matrix, the more conducive it is to absorb PLGA matrix onto the surface of g1-n-HA particles, so that the nucleation and crystallinity are further promoted, which may be another factor to enhance the mechanical property for PLGA [27].

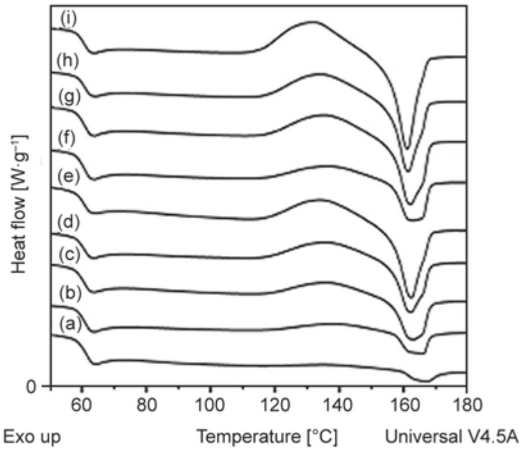

Figure 8. DSC thermograms of samples of (a) PLGA, (b) 3 wt%, (c) 8 wt%, (d) 5 wt%, (e) 25 wt% of g2-n-HA, (f) 3 wt%, (g) 8 wt%, (h) 15 wt%, (i) 25 wt% of g1-n-HA

3.2.3. Mechanical properties

The initial mechanical property is usually a critical technical index for bone fracture internal fixation materials. The enhancement dependency of bending strength and tensile strength for PLGA after different addition content of two g-n-HA are shown in Figure 9. Obviously, it can be seen that the maximum enhancement of bending strength and tensile strength is at 3 wt% surface-grafted, and it leads to a reduction in the bending strength and tensile strength with the further increasing g-n-HA content. Moreover, g1-n-HA has more improvement in mechanical properties than g2-n-HA, whose bending strength and tensile strength were both over 20% higher than those of pure PLGA when 3 wt% g1-n-HA was added. Especially, even 15 wt% g1-n-HA was added, whose bending and tensile strength are still 8 and 6% higher than those of pure PLGA, respectively. However, in our previous study, the maximum addition content of n-HA into PLGA was only 10 wt%, and the addition of 15 wt% n-HA decreased markedly its bending strength [18, 19]. Obviously, the mechanical enhancement for PLGA is by far the most excellent as comparing to some related literatures [28]. The main reason may also be ascribed to the higher grafting amount for g1-n-HA, which might improve the dispersion of g1-n-HA nanoparticles in PLGA matrix and the interfacial adhesion as well as the increased crystallinity for PLGA.

4. Conclusions

In this study, a new method of surface-grafting D, L-lactide (DLLA) with the assistance of citric acid

Table 1. Thermal properties of PLGA after different addition content of two g-n-HA determined by DSC

Sample	Addition g-n-HA content [wt%]	T_m [°C]	ΔH_m [$J \cdot g^{-1}$]	X_c [%]
PLGA	0	166.78	2.423	2.586
g2-n-HA/PLGA	3	164.24	5.221	5.744
	8	161.98	10.45	12.12
	15	161.68	13.99	17.57
	25	161.93	18.14	25.81
g1-n-HA/PLGA	3	161.86	9.623	10.59
	8	161.71	16.05	18.62
	15	161.13	18.56	23.30
	25	160.92	22.96	32.67

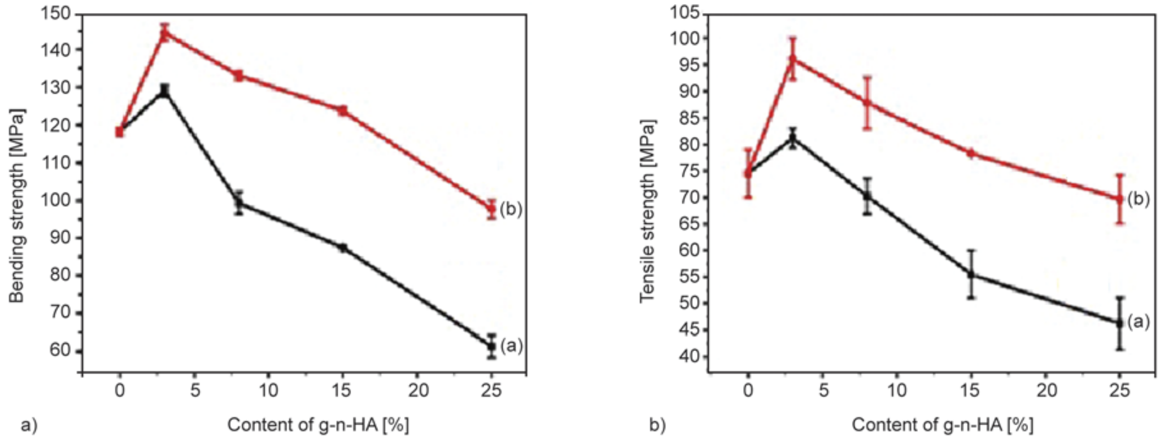

Figure 9. Mechanical properties of different g-n-HA content (a) bending strength, (b) tensile strength (red curve is g1-n-HA, and black curve is g2-n-HA)

for n-HA was designed, comparing with the surface-grafting without citric acid, and the two surface-grafted n-HA were respectively introduced into PLGA matrix with different contents. The results showed that the two surface-grafting methods for n-HA were both successful. However, citric acid played a critical role in surface-grafting, which had much higher grafting amount and better dispersion than surface-grafting without citric acid, so that the g-n-HA/PLGA composites exhibited more excellent mechanical properties owing to the better dispersion and interfacial adhesion throughout PLGA matrix, and the higher crystallinity for PLGA, whose bending strength and tensile strength were both over 20% higher than those of pure PLGA when 3 wt% n-HA was added. Especially, even 15 wt% n-HA was added, whose bending and tensile strength were still 8 and 6% higher than those of PLGA, respectively. The above results suggested that the new surface-grafting with the aid of citric acid for n-HA was an ideal novel surface modification method, which could greatly improve the dispersion and achieve a better mechanical strength for g-n-HA/PLGA composite with higher n-HA content, suggesting that it has a great potential in the bone fracture internal fixation application in future. For the degradability and biological properties of the g-n-HA/PLGA composite, the work is in progress, and the results would be reported in another paper in the future.

Acknowledgements

This work was supported by the Talent Training Project of West Light Foundation of Chinese Academy of Science, and National Natural Science Foundation (31000440).

References

[1] Raikin S. M., Ching A. C.: Bioabsorbable fixation in foot and ankle. Foot and Ankle Clinics, **10**, 667–684 (2005).
DOI: 10.1016/j.fcl.2005.06.008

[2] Saito E., Liao E. E., Hu W-W., Krebsbach P. H., Hollister S. J.: Effects of designed PLLA and 50:50 PLGA scaffold architectures on bone formation *in vivo*. Journal of Tissue Engineering and Regenerative Medicine, **7**, 99–111 (2013).
DOI: 10.1002/term.497

[3] Tiainen J., Soini Y., Törmälä P., Waris T., Ashammakhi N.: Self-reinforced polylactide/polyglycolide 80/20 screws take more than 1¹/2 years to resorb in rabbit cranial bone. Journal of Biomedical Materials Research Part B: Applied Biomaterials, **70**, 49–55 (2004).
DOI: 10.1002/jbm.b.30013

[4] Swetha M., Sahithi K., Moorthi A., Srinivasan N., Ramasamy K., Selvamurugan N.: Biocomposites containing natural polymers and hydroxyapatite for bone tissue engineering. International Journal of Biological Macromolecules, **47**, 1–4 (2012).
DOI: 10.1016/j.ijbiomac.2010.03.015

[5] Sun F., Zhou H., Lee J.: Various preparation methods of highly porous hydroxyapatite/polymer nanoscale biocomposites for bone regeneration. Acta Biomaterialia, **7**, 3813–3828 (2001).
DOI: 10.1016/j.actbio.2011.07.002

[6] Wang D. X., He Y., Bi L., Qu Z. H., Zou J. W., Pan Z., Fan J. J., Chen L., Dong X., Liu X. N., Pei G. X., Ding J. D.: Enhancing the bioactivity of poly(lactic-*co*-glycolic acid) scaffold with a nano-hydroxyapatite coating for the treatment of segmental bone defect in a rabbit model. International Journal of Nanomedicine, **8**, 1855–1865 (2013).
DOI: 10.2147/IJN.S43706

[7] Kim S-S., Park M. S., Jeon O., Choi C. Y., Kim B-S.: Poly(lactide-*co*-glycolide)/hydroxyapatite composite scaffolds for bone tissue engineering. Biomaterials, **27**, 1399–1409 (2006).
DOI: 10.1016/j.biomaterials.2005.08.016

[8] Petricca S. E., Marra K. G., Kumta P. N.: Chemical synthesis of poly(lactic-*co*-glycolic acid)/hydroxyapatite composites for orthopaedic applications. Acta Biomaterialia, **2**, 277–286 (2006).
DOI: 10.1016/j.actbio.2005.12.004

[9] Šupová M.: Problem of hydroxyapatite dispersion in polymer matrices: A review. Journal of Materials Science: Materials in Medicine, **20**, 1201–1213 (2009).
DOI: 10.1007/s10856-009-3696-2

[10] Borum L., Wilson O. C.: Surface modification of hydroxyapatite. Part II. Silica. Biomaterials, **24**, 3681–3688 (2003).
DOI: 10.1016/S0142-9612(03)00240-0

[11] Liu Q., de Wijn J. R., Bakker D., van Toledo M., van Blitterswijk C. A.: Polyacids as bonding agents in hydroxyapatite polyester-ether (PolyactiveTM 30/70) composites. Journal of Materials Science: Materials in Medicine, **9**, 23–30 (1998).
DOI: 10.1023/A:1008826410395

[12] Dong G-C., Sun J-S., Yao C-H., Jiang G. J., Huang C-W., Lin F-H.: A study on grafting and characterization of HMDI-modified calcium hydrogenphosphate. Biomaterials, **22**, 3179–3189 (2001).
DOI: 10.1016/S0142-9612(01)00070-9

[13] Wang Y., Zhang X., Yan J., Xiao Y., Lang M.: Surface modification of hydroxyapatite with poly(methyl methacrylate) via surface-initiated ATRP. Applied Surface Science, **257**, 6233–6238 (2011).
DOI: 10.1016/j.apsusc.2011.02.045

[14] Hong Z., Zhang P., Liu A., Chen L., Chen X., Jing X.: Composites of poly(lactide-*co*-glycolide) and the surface modified carbonated hydroxyapatite nanoparticles. Journal of Biomedical Materials Research: Part A, **81**, 515–522 (2007).
DOI: 10.1002/jbm.a.31038

[15] Cui Y., Liu Y., Cui Y., Jing X., Zhang P., Chen X.: The nanocomposite scaffold of poly(lactide-*co*-glycolide) and hydroxyapatite surface-grafted with L-lactic acid oligomer for bone repair. Acta Biomaterialia, **5**, 2680–2692 (2009).
DOI: 10.1016/j.actbio.2009.03.024

[16] Lock J., Nguyen T. Y., Liu H. N.: Nanophase hydroxyapatite and poly(lactide-*co*-glycolide) composites promote human mesenchymal stem cell adhesion and osteogenic differentiation in vitro. Journal of Materials Science: Materials in Medicine, **23**, 2543–2552 (2012).
DOI: 10.1007/s10856-012-4709-0

[17] Jiang L., Xiong C., Chen D., Jiang L., Pang X.: Effect of n-HA with different surface-modified on the properties of n-HA/PLGA composite. Applied Surface Science, **259**, 72–78 (2012).
DOI: 10.1016/j.apsusc.2012.06.091

[18] Jiang L., Xiong C., Jiang L., Chen D., Li Q.: Effect of n-HA content on the isothermal crystallization, morphology and mechanical property of n-HA/PLGA composites. Materials Research Bulletin, **48**, 1233–1238 (2013).
DOI: 10.1016/j.materresbull.2012.11.113

[19] Jian L-X., Jiang L-Y., Ma C., Han C-T., Xu L-J., Xiong C-D.: Preparation and characterization of nano-hydroxyapatite/plga composites with novel surface-modified nano-hydroxyapatite. Jounal of Inorganic Materials, **28**, 751–756 (2013).
DOI: 10.3724/SP.J.1077.2013.12502

[20] Qiu X., Hong Z., Hu J., Chen L., Chen X., Jing X.: Hydroxyapatite surface modified by L-lactic acid and its subsequent grafting polymerization of L-lactide. Biomacromolecules, **6**, 1193–1199 (2005).
DOI: 10.1021/bm049502l

[21] Wu H., Pang D., Ma C., Li Q., Xiong C.: Composites of hydroxyapatite whiskers/poly(L-lactide-*co*-glycolide) with high tensile plasticity. Journal of Macromolecular Science Part B: Physics, **51**, 1242–1255 (2011).
DOI: 10.1080/00222348.2011.627824

[22] Lee J. H., Shofner M. L.: Copolymer-mediated synthesis of hydroxyapatite nanoparticles in an organic solvent. Langmuir, **29**, 10940–10944 (2013).
DOI: 10.1021/la402434v

[23] Hong Z., Qiu X., Sun J., Deng M., Chen X., Jing X.: Grafting polymerization of L-lactide on the surface of hydroxyapatite nano-crystals. Polymer, **45**, 6699–6706 (2004).
DOI: 10.1016/j.polymer.2004.07.036

[24] Boanini E., Fini M., Gazzano M., Bigi A.: Hydroxyapatite nanocrystals modified with acidic amino acids. European Journal of Inorganic Chemistry, **23**, 4821–4826 (2006).
DOI: 10.1002/ejic.200600423

[25] Wei J., Liu A., Chen L., Zhang P., Chen X., Jing X.: The surface modification of hydroxyapatite nanoparticles by the ring opening polymerization of γ-benzyl-L-glutamate *N*-carboxyanhydride. Macromolecular Bioscience, **9**, 631–638 (2009).
DOI: 10.1002/mabi.200800324

[26] Zhang Y., Meng B., Chen L., Tao J., Wu Z.: Properties and structures of polylactide filled with poly(ε-caprolactone)-coated calcium carbonate. Journal of Applied Polymer Science, **125**, 952–958 (2012).
DOI: 10.1002/app.36280

[27] Luo Y-B., Li W-D., Wang X-L., Xu D-Y., Wang Y-Z.: Preparation and properties of nanocomposites based on poly(lactic acid) and functionalized TiO_2. Acta Materialia, **57**, 3182–3191 (2009).
DOI: 10.1016/j.actamat.2009.03.022

[28] Hong Z., Zhang P., He C., Qiu X., Liu A., Chen L., Chen X., Jing X.: Nano-composite of poly(L-lactide) and surface grafted hydroxyapatite: Mechanical properties and biocompatibility. Biomaterials, **26**, 6296–6304 (2005).
DOI: 10.1016/j.biomaterials.2005.04.018